


AN ABSTRACT OF THE THESIS OF

Ming Yang for the degree of Doctor of Philosophy in
Chemistry presented on August 22, 1990

Title: Coherent Raman Spectroscopy of Molecular Clusters

Redacted for Privacy

Abstract approved:

 Professor Joseph W. Nibler

Several refinements of the Coherent anti-Stokes Raman Scattering (CARS) method have been developed to permit scanning of the 0 - 500 cm^{-1} low frequency shift region at high resolution and sensitivity. These involve use of an injection-seeded Nd:YAG laser tuned such that the 532nm harmonic of the single frequency output matches a sharp I_2 absorption. A sensor/circuit was built to eliminate "bad" multimode shots and, when combined with an I_2 cell to effectively filter 532 nm scattering from the nearby CARS signal, excellent spectra were obtained down to zero Raman shift.

Applications of this system were made to several systems. Pure rotational spectra were obtained for several nonvolatile compounds, AsCl_3 in heated cell and HgCl_2 and CS_2 in a cold jet expansion from a hot nozzle cell. These are the first coherent Raman data obtained for such high temperature inorganic vapors.

The condensation of nitrogen in a free jet expansion was also

studied by the high resolution CARS technique, which was found to give slightly better S/N than Raman loss spectroscopy. By probing at different points along the expansion axis the vibrational frequency shifts of nitrogen clusters were accurately measured and used with equilibrium data to deduce cluster temperatures. The liquid to β -solid phase transformation of nitrogen was observed in the jet and a gradual "isothermal" freezing model was used to describe the phase transition of small N_2 drops. The influence of molecules such as CO_2 and He on the nucleation process in the free jet expansion was also examined. The surface effects on the evaporative cooling of the small clusters was also considered and used to determine mean cluster diameters of 38 nm for a cone nozzle and 24 nm for a shim nozzle.

Coherent Raman Spectroscopy of Molecular Clusters

by

Ming Yang

A THESIS

submitted to

Oregon State University

in partial fulfillment of
the requirements for the
degree of

Doctor of Philosophy

Completed August 22, 1990

Commencement June 1991

APPROVED:

Redacted for Privacy

Professor of Chemistry in charge of major

Redacted for Privacy

Head of Department of Chemistry

Redacted for Privacy

Dean of Graduate School

Date thesis is presented _____ August 22, 1990

Typed by researcher for _____ Ming Yang

To my wife

ACKNOWLEDGEMENTS

I would like to thank Professor Joseph W. Nibler for his support and encouragement over the years. His guidance is not only in scientific matters but also otherwise. I am grateful for having had the opportunity to work with him.

My thanks also go to all of the group members who have contributed in so many ways during the research of this thesis.

I credit my father, Zhang Yang, with nurturing my interest in science.

I also thanks to my wife, Lei Li, for her encouragement and patience.

TABLE OF CONTENTS

CHAPTER 1	
INTRODUCTION	1
Historical Perspective	2
Nonlinear Raman Spectroscopy	3
 CHAPTER 2	
THEORETICAL BACKGROUND	7
Coherent Raman Spectroscopy	7
Maxwell's Equations	7
Electric-Field-Induced Polarization	9
Symmetry Properties of $\chi^{(3)}$	13
CARS Amplitudes	16
Microscopic Form of $\chi^{(3)}$	19
Selection Rules	27
Spectral Line Shape	28
Free Jet Expansions	32
Classical Homogeneous Nucleation Theory	36
Thermodynamic Aspects	38
Kinetic Aspects	41
Condensation in Free Jet Expansion	43
 CHAPTER 3	
DEVELOPMENT OF A BACKGROUND REDUCTION TECHNIQUE FOR LOW FREQUENCY CARS AND A MULTIMODE REJECTOR FOR A SEEDED Nd:YAG LASER	46
Introduction	46
Basic Laser Theory	53
Two-level Laser System	53
Intensity Amplification	56
Population Inversion	58
Loss Processes	60
Threshold Condition	62
Q-Switched Laser	64
Injection Seeding Theory	65
Longitudinal Modes of Pulsed Laser	65
Q-Switch Buildup Time: Unseeded Operation	67
Q-Switch Buildup Time: Seeded Operation	70
Injection Seeder	71
Frequency Control of Injection Seeder	75
Development of Background Reduction Technique	77
Modification of Frequency Tuning for the Seeder	77
I ₂ Absorption Spectrum	81
Background Reduction Technique	83
Development of Laser Multimode Rejector	85
Basic idea of the apparatus	85
Electronic circuitry	88
Results	90

TABLE OF CONTENTS (cont.)

CHAPTER 4	
APPLICATION OF CARS AND SRS FOR INVOLATILE MOLECULES	97
Introduction	97
Experimental	99
High Temperature Jet Expansion Cell	99
SRL spectrometer	99
Results	103
The AsCl_3 molecule	103
The HgCl_2 molecule	103
The CS_2 molecule	109
Summary	114
CHAPTER 5	
STUDIES OF SMALL CLUSTERS IN JET EXPANSIONS BY HIGH RESOLUTION CARS	116
Introduction	116
Experimental	117
High resolution CARS Spectrometer	117
Frequency Calibration	119
Pulsed Jet Assembly	120
Results	123
Comparison of High Resolution CARS and SRS in Studying Cluster Formation in Free Jet Expansion	123
Vibrational Raman Spectrum of Condensed Phase	125
Conditions for Forming Cluster in Jet Expansion	128
Phase Transition in the Jet Expansion	129
Temperature of Liquid Aggregate	137
The Freezing Zone	139
Rotational Temperature of the Monomer	142
Cluster Size Estimate	142
Surface Tension Effect on Cooling Curves	147
Summary	151
REFERENCES	153
APPENDICES:	159
A. Data Collection Program for CARS Experiment	159
B: Seeded Nd:YAG Laser Scan Program	178
C: Seeded Nd:YAG Laser "Bad Shot" Rejector User Manual	181
D: Laser Noise Rejector	185
E: Some Data Used in This Thesis	187

LIST OF FIGURES

<u>Figures</u>	<u>Page</u>
1.1 Energy level diagrams for various Raman process discussed in the text	4
2.1 Coherent anti-Stokes Raman scattering phase-matching diagram	20
2.2 Energy diagrams for several nonlinear processes	22
2.3 Real and imaginary components of $\chi^{(3)}$	30
2.4 Square of $\chi^{(3)}$	31
2.5 Molecular velocity distribution	34
2.6 Results from jet expansion theory	37
2.7 Nucleation process	40
2.8 Free energy of nucleation process	40
3.1 Schematic of CARS spectrometer	48
3.2 Three dimensional phase matching diagram	50
3.3 Pure rotational CARS spectrum of N_2	51
3.4 Calculated pure rotational spectra of $HgCl_2$	52
3.5 Two-level Laser system	54
3.6(a) Line shape of absorption and emission	59
3.6(b) Relative populations of laser system	59
3.7 Threshold condition	63
3.8 Longitudinal modes of Nd:YAG pulsed laser	66
3.9 Q-switch buildup time reduction	69
3.10 Injection seeder	72
3.11 Monolithic isolated end pumped ring	73
3.12 Frequency and temperature diagram	76

LIST OF FIGURES (cont.)

<u>Figures</u>	<u>Page</u>
3.13 Temperature control circuit	78
3.14 Temperature scan circuit	80
3.15 I ₂ absorption spectrum	82
3.16 CARS process diagram	83
3.17 CARS pure rotational spectrum of N ₂	84
3.18 Transmission through the I ₂ cell at 18788.451 cm ⁻¹	86
3.19 "Bad Shot" rejector circuit diagram	89
3.20 Schematic of CARS spectrometer with the rejector	91
3.21 Pure rotational CARS spectrum of N ₂ taken with "bad shot" rejector	93
3.22 High resolution CARS spectrum of O ₂ taken with and without "bad shot" rejector	94
3.23 Nonresonant background CARS spectrum of Methyl iodide/He in a jet expansion taken with and without the rejector	95
4.1 High temperature nozzle cell	100
4.2 High resolution SRS spectrometer	102
4.3 Pure rotational Raman loss spectrum of AsCl ₃	104
4.4 Calculated R and S branch pure rotational spectrum of AsCl ₃ .	105
4.5 Pure rotational jet spectrum of HgCl ₂	107
4.6 Calculated pure rotational jet spectrum of HgCl ₂	108
4.7 Pure rotational CARS spectrum of CS ₂	111

LIST OF FIGURES (cont.)

<u>Figures</u>	<u>Page</u>
4.9 High resolution spectra of CS ₂	113
5.1 High resolution CARS spectrometer	118
5.2 Cross-section of pulsed nozzles	121
5.3 Comparison of the signal to noise of CARS and SRS	124
5.4 Crystal structure of solid nitrogen	126
5.5 Vibrational spectra of nitrogen in condensed phases	127
5.6 High resolution CARS spectra of nitrogen vapor and solid.	131
5.7 CARS spectra of nitrogen aggregates in a jet expansion	132
5.8 CARS spectra of a N ₂ and CO ₂ mixture expansion	135
5.9 Aggregate spectra of nitrogen/He expansions	136
5.10 Three different extrapolation choices of N ₂ frequency vs temperature	138
5.11 Supercooled liquid and β -solid temperature in a free jet expansion	140
5.12 Temperature of vapor, liquid, and solid N in a free jet expansion	143
5.13 Cluster size estimation from cooling curves for a cone nozzle	145
5.14 Cluster size estimation from cooling curves for a shim nozzle	146
5.15 Calculated P/P ₀ changes with the size of clusters	149

LIST OF TABLES

<u>Table</u>		<u>Page</u>
3.1	Truth table for the AND function	88
5.1	Comparison of size estimation with and without the considering of surface effect	150

LIST OF APPENDIX FIGURES

C.1	Bad shot rejector front panel	184
D.1	Temperature scan and noise rejector circuit	186

COHERENT RAMAN SPECTROSCOPY OF MOLECULAR CLUSTERS

CHAPTER 1 INTRODUCTION

The research reported in this thesis describes some technique and instrumentation development for coherent Raman spectroscopy along with application to several systems of chemical interest. This first chapter briefly introduces the area of nonlinear Raman spectroscopy and some of the historical development of this method. Chapter 2 presents some theoretical background regarding Coherent Anti-Stokes Raman scattering (CARS), free jet expansions, and nucleation processes. Description of a new multimode bad laser pulse rejector for a single mode Nd:YAG laser and the development of a background reduction technique for low frequency CARS are presented in chapter 3. In chapter 4, studies of high temperature molecules by coherent Anti-Stokes Raman and Raman loss techniques are presented. This work has yielded the first pure rotational spectrum of HgCl_2 cooled by jet expansions. In this chapter also appears a discussion of the formidable difficulties in such studies of high temperature molecules. Finally in chapter 5, high resolution CARS studies of aggregate formation of nitrogen in free jet expansions are presented. A gradual "isothermal" model is introduced and a cooling curve calculated from the model is in a good agreement with the experimental data. The surface effect for the cooling curve is also discussed and cluster size has been estimated from the cooling curve. A comparison is made with results obtained by high resolution stimulated Raman spectroscopy.

HISTORICAL PERSPECTIVE

In 1928 Chandrasekhara V. Raman, an Indian physicist, observed that, when dust-free liquids or gases were illuminated by light of a particular wavelength, the scattered radiation had not only the wavelengths of the incident light (Rayleigh scattering) but also light of different wavelengths (Raman effect, 1928).¹ In the same year Landsberg and Mandelstam observed this phenomenon in transparent solids and reported the light scattering with change of frequency in quartz.²

For more than 50 years Raman spectroscopy has been an important method for the investigation of molecular structure.³ It is particularly useful in that it allows observation of transitions between molecular states for which the dipole matrix element vanishes. As a result, Raman spectroscopy has proved to be a valuable complement to infrared spectroscopy.⁴

Spontaneous Raman scattering is, however, a weak effect; the scattering cross sections are typically less than 10^{-30} cm², and for a Raman experiment with a gas at 1 torr pressure only about 1 incident photon in 10^{15} will be observed as an inelastically scattered photon. The invention of the laser revolutionized the practice of Raman spectroscopy in the early 1960s. Major difficulties, however, remained. Because the Raman effect was so weak, even faint luminescence could obscure the desired spectra. It was difficult or impossible to study, for example, flames, plasmas, crystals with fluorescent impurities, and many biological molecules.

Discovery of stimulated Raman scattering by Woodbury and Ng in 1962,⁵ followed closely by the observation of four wave mixing in coherent anti-Stokes Raman scattering(CARS) in 1963 by Terhune⁶ and by Maker and Terhune⁷ in 1965, marked the beginning of the field of nonlinear Raman spectroscopy. The early experiments were constrained by the available lines of fixed wavelength lasers. However the technique has undergone rapid development with the availability of the tunable dye laser in the early 1970's.

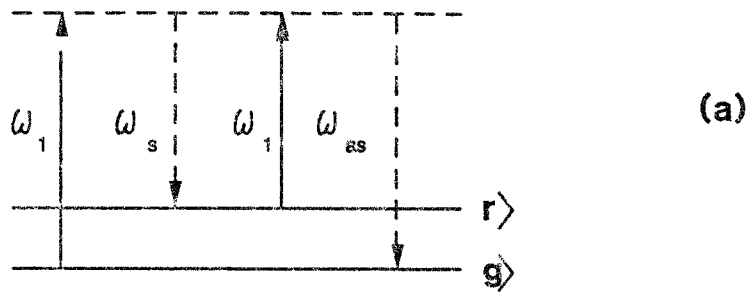
NONLINEAR RAMAN SPECTROSCOPY

Figure 1.1 shows the energy level schematic for spontaneous Raman spectroscopy, CARS and the stimulated Raman spectroscopic techniques of Raman gain and Raman loss spectroscopy. Spontaneous Raman spectroscopy is a "two photon" process which involves the interaction of a molecule with intense monochromatic radiation ν_I , having an energy content different from that necessary to excite the molecule to a quantized upper state. This interaction, referred to as inelastic scattering, results in the creation of an induced dipole given by

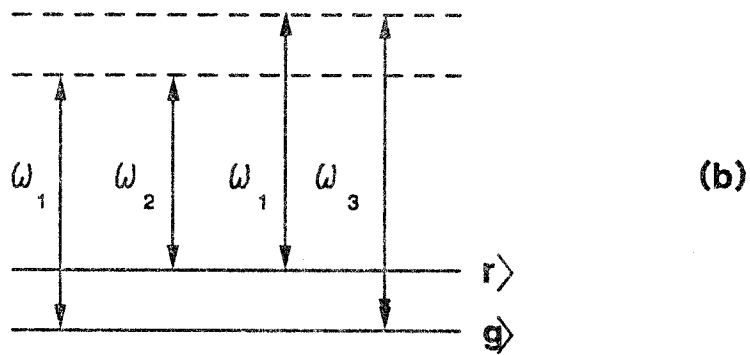
$$\mu_I = \alpha \epsilon \quad (1.1)$$

In this condition the molecule is said to exist in a virtual state. The existence of a molecule in a virtual state is essentially instantaneous with the molecule returning to the same lower level with the concurrent emission of radiation of frequency ν . If the final

Spontaneous Raman Scattering



Coherent Anti-Stokes Raman Scattering



Stimulated Raman Scattering

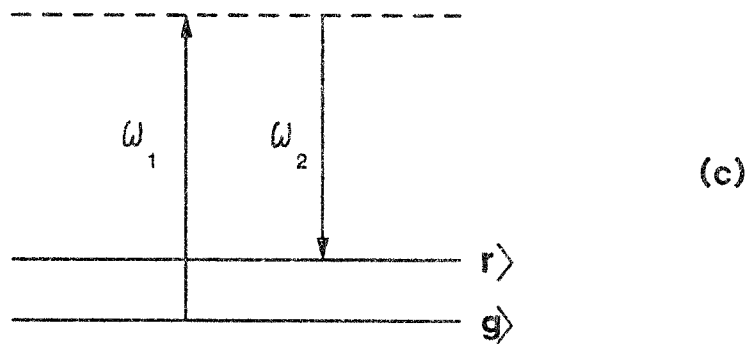


Figure 1.1: Energy level diagrams for various Raman process discussed in the text.

state of the molecule differs from the initial state, then the scattered radiation will be shifted in frequency from the incident radiation, and the scattering is inelastic. If $\nu_I > \nu$ the scattered radiation is called Stokes scattering, and if $\nu_I < \nu$ it is referred to as anti-Stokes scattering. The net result of this process is to produce scattered radiation which has been shifted in frequency from the initial radiation by an amount equivalent to the difference between two quantized energy levels.

In contrast, nonlinear Raman spectroscopy is a "four photon" process which couples two or three incident laser beams to produce the observed signal. CARS spectroscopy is depicted in Figure 1.1b in which three waves, two at a pump frequency ω_1 and one at a "Stokes" frequency ω_2 , are mixed in a sample to produce a new coherent beam at the anti-Stokes frequency $\omega_3 = 2\omega_1 - \omega_2$. This mixing occurs for all samples but is greatly enhanced if the frequency difference $\Delta \equiv \omega_1 - \omega_2$ approaches a Raman active vibrational or rotational resonance in the medium, often several orders of magnitude greater than that of spontaneous Raman signal. An alternative designation is three-wave Raman mixing. If $\Delta = \omega_1 - \omega_2$ is positive then $2\omega_1 - \omega_2 = \omega_1 + \Delta$ is greater than ω_1 and the detected frequency is greater than either of the two incident frequencies. In this sense the scattering is 'anti-Stokes'. If $\omega_1 < \omega_2$, $2\omega_1 - \omega_2 = \omega_1 - |\Delta|$ and the detected frequency is lower than either of the incident frequencies. This will be designated coherent Stokes Raman scattering (CSRS) which is also depicted Figure 1.1b.

Another non-linear Raman process closely related to CARS, but

distinct from it experimentally, is the stimulated Raman scattering depicted in Figure 1.1c . Two laser beams simultaneously impinge upon the sample and tuning the difference frequency to a molecular resonance results in a decrease in intensity of the higher frequency beam along with a corresponding increase in the intensity of the lower frequency beam. Again, the beams have the frequency relationship $\omega_1 - \omega_2 = \omega_{rg}$.

From the spectroscopic point of view, nonlinear Raman spectroscopy provides the same information as that obtained by Raman scattering. However, the major reason for interest is that the high signal levels, signal collimation, and inherently high resolution increase the signal detectivity so that it is more practical to obtain a CARS spectrum than a spontaneous Raman spectrum in many circumstances.

CHAPTER 2. THEORETICAL BACKGROUND

COHERENT RAMAN SPECTROSCOPY

The coherent Raman technique is one of many nonlinear optical effects. The theory of coherent anti-Stokes Raman scattering was developed by Bloembergen and co-workers,^{8,9} Maker and Terhune,^{6,7} and Butcher.¹⁰ A large amount of literature was published subsequently on the theory of the various nonlinear Raman effects. The discussion of coherent Raman scattering in this chapter is a synthesis of the theories contained in references 5 - 17. Also, the theories of free jet expansions and nucleation processes in the jet expansion will be discussed in this chapter.

Maxwell's Equations

Maxwell's equations are the starting point for a macroscopic theory of propagation of light in matter. Here we are only concerned with non-magnetic, non-conducting, isotropic materials, such as molecular liquids and gases, which would be in thermodynamic equilibrium except for the fact that electromagnetic radiation is propagating in them. For such systems the equations take the form

$$\nabla \cdot \mathbf{D} = 0 \quad (2.1)$$

$$\nabla \cdot \mathbf{H} = 0 \quad (2.2)$$

$$\nabla \times \mathbf{E} = - \frac{1}{c} \frac{\partial \mathbf{H}}{\partial t} \quad (2.3)$$

$$\nabla \times \mathbf{H} = \frac{1}{c} \frac{\partial \mathbf{D}}{\partial t} \quad (2.4)$$

The electric displacement \mathbf{D} is related to the electric field vector by

$$\mathbf{D} = \mathbf{E} + 4\pi\mathbf{P} \quad (2.5)$$

where \mathbf{P} is the electric polarization in the medium. Substituting Eq. (2.5) into Eq. (2.4) and then the result into the curl of Eqn. (2.1), the wave equation with a polarization source term on the right-hand side is

$$\nabla \times (\nabla \times \mathbf{E}) + \frac{1}{c^2} \frac{\partial^2 \mathbf{E}}{\partial t^2} = - \frac{4\pi}{c^2} \frac{\partial^2 \mathbf{P}}{\partial t^2} \quad (2.6)$$

We assume that the electric field and polarization will be sums of functions with frequencies of the applied fields, of the sample resonances and of the various sum and difference frequencies:

$$\mathbf{E}(\mathbf{r}, t) = \frac{1}{2} \sum_j \{ \mathbf{E}_j \exp[i(\mathbf{k}_j \cdot \mathbf{r} - \omega_j t)] + \text{c.c.} \} \quad (2.7)$$

$$\mathbf{P}(\mathbf{r}, t) = \frac{1}{2} \sum_j \{ \mathbf{P}_j \exp[i(\mathbf{k}_j \cdot \mathbf{r} - \omega_j t)] + \text{c.c.} \} \quad (2.8)$$

where the waves are propagating in the z direction, \mathbf{E}_j and \mathbf{P}_j are the j th frequency components and c.c. is the complex conjugate. For a given frequency component ω_j , the wave equation is

$$\nabla \times (\nabla \times \mathbf{E}_j) - (\omega_j/c)^2 \mathbf{E}_j = 4\pi(\omega_j/c)^2 \mathbf{P}_j \quad (2.9)$$

which gives the electric field response to an oscillating polarization.

Electric-field-induced Polarization

The electric dipole moment induced in a molecule or atom by an electric field \mathbf{E} can be expanded in a power series

$$\mu = \alpha \mathbf{E} + \beta \mathbf{E}^2 + \gamma \mathbf{E}^3 + \dots \quad (2.9)$$

The coefficients α, β, γ , etc., are tensor quantities to account for the fact that the induced dipole vector may point in a direction different from that of the electric field vector. The polarizability α , is rank 2, and the hyperpolarizabilities β, γ are of rank 3, 4, ..., respectively. A medium displays a bulk polarization, as a consequence of the dipole moment induced in its constituent atom or molecules. The polarization \mathbf{P} is given by

$$\mathbf{P} = \chi^{(1)} \mathbf{E} + \chi^{(2)} \mathbf{E}^{(2)} + \chi^{(3)} \mathbf{E}^{(3)} + \dots \quad (2.10)$$

where $\chi^{(1)}, \chi^{(2)}, \chi^{(3)}, \dots$ are the first, second, third, order dielectric susceptibility tensors.

For materials for which the optical index of refraction is near unity, such as gases, the macroscopic and microscopic fields are

nearly identical, and

$$P = N \mu \quad (2.11)$$

Moreover, it is apparent that

$$\chi^{(1)} = N\alpha, \quad \chi^{(2)} = N\beta, \quad \text{and} \quad \chi^{(3)} = N\gamma \quad (2.12)$$

where N is the particle density. It is important to emphasize this connection of the macroscopic polarization and the induced dipole, and of the dielectric susceptibility tensors and the molecular polarizabilities, because a theoretical description of the effect of the applied field deals with the molecular properties, while the experimental measurements are macroscopic in nature.

The linear susceptibility is related to the complex dielectric constant, $\epsilon = 1 + 4\pi\chi^{(1)}$, and thus $\chi^{(1)}$ is responsible for classical linear optical phenomena, including refraction, absorption, Rayleigh scattering, and normal Raman scattering. In the absence of absorption, ϵ is real and is equal to the square of the index of refraction n . The second order susceptibility, $\chi^{(2)}$, and all higher-order even terms of the susceptibility vanish in isotropic media such as gases and liquids and in centrosymmetric crystals, in which the macroscopic dielectric properties always exhibit inversion symmetry. $\chi^{(2)}$ is, however, important in non-centrosymmetric crystals such as potassium dideuterium phosphate, KD^*P , commonly used as an electro-optic Q-switch material and for second-harmonic and sum and difference frequency generation. $\chi^{(3)}$ is the first non-linear term which is non-zero for all media and which is responsible for the coherent Raman

phenomena as well as for other effects such as third-harmonic generation. Neglecting higher-order terms, substitution of (2.10) into (2.9) yields the wave equation with the third-order polarization.

$$P^{(3)}(r, t) = \chi^{(3)} E(r, t)E(r, t)E(r, t), \quad (2.13)$$

where the spatial and temporal variation of the field with the induced polarization is made explicit.

Coherent anti-Stokes Raman scattering and other three wave mixing processes involve up to three distinct field frequencies j , so the summation in Eq. (2.7) should be $j=1$ to 3. Equation (2.7) also can be written as

$$E(r, t) = \frac{1}{2} \sum_{\substack{j=-3 \\ j \neq 0}}^3 E(\omega_j, r) \exp[i(k_j \cdot r - \omega_j t)], \quad (2.14)$$

where $\omega_{-j} \equiv -\omega_j$, $k_{-j} \equiv -k_j$, and $E(\omega_{-j}, r) \equiv E^*(\omega_j, r)$. Combining Eq. (2.13) and Eq. (2.14), the third order polarization can be written as

$$\begin{aligned} P^{(3)} = \frac{1}{8} \sum_{\substack{i, j, k = -3 \\ i, j, k \neq 0}} \chi^{(3)} E(\omega_i, r) E(\omega_j, r) E(\omega_k, r) \\ \times \exp[i(k_i + k_j + k_k) \cdot r] \exp[-i(\omega_i + \omega_j + \omega_k)t] \end{aligned} \quad (2.15)$$

Equation (2.15) shows that $P^{(3)}$ will have frequency components at

$$\omega_0 = \omega_i + \omega_j + \omega_k, \quad (2.16)$$

where ω_i , ω_j and ω_k can be positive or negative. Thus $P^{(3)}$ will have many frequency components, including $3\omega_1$, $3\omega_2$, and $3\omega_3$, which correspond to third-harmonic generation, $\omega_1 + \omega_2 + \omega_3$, giving frequency summation, as well as a CARS component at $\omega_1 - \omega_2 + \omega_3$, where $\omega_1 > \omega_2$. $\chi^{(3)}$ is also a function of ω_0 , ω_i , ω_j , and ω_k , therefore it can not be moved from the summation in Eq. (2.15).

We can write $P^{(3)}$ in terms of its Fourier components

$$P^{(3)}(r, t) = \frac{1}{2} \sum_{\substack{i, j, k=-3 \\ i, j, k \neq 0}} P^{(3)}(\omega_0, r) \exp[-i(\omega_0 t)], \quad (2.17)$$

where ω_0 is given by Eq. (2.16). By substituting Eq. (2.17) into the left hand side of Eq. (2.15), the connection of the Fourier components of the polarization with those of the electric fields can be shown:

$$P^{(3)}(\omega_0, r) = \frac{1}{4} \chi^{(3)} E(\omega_i, r) E(\omega_j, r) E(\omega_k, r) \times \exp[i(k_i + k_j + k_k) \cdot r] \quad (2.18)$$

We also can express Eq. (2.18) in terms of the Cartesian components as

$$P_{\rho}^{(3)}(\omega_0, r) = \left(\frac{6}{n!}\right) \frac{1}{4} \chi_{\rho\sigma\tau\nu}^{(3)}(-\omega_0, \omega_i, \omega_j, \omega_k) \times E_{\sigma}(\omega_i, r) E_{\tau}(\omega_j, r) E_{\nu}(\omega_k, r) \exp[i(k_i + k_j + k_k) \cdot r] \quad (2.19)$$

where $\rho, \sigma, \tau, \nu = x, y, \text{ or } z$. The $\chi^{(3)}(-\omega_0, \omega_i, \omega_j, \omega_k)$ represents the susceptibility for the process in which a polarization is induced at $\omega_0 = \omega_i + \omega_j + \omega_k$. While the ordering of the frequencies $\omega_i, \omega_j, \omega_k$

or the Cartesian indices σ , τ , ν cannot be permuted without altering $\chi_{\rho\sigma\tau\nu}^{(3)}$, permutation of pairs (i,σ) , (j,τ) , and (k,ν) , which corresponds to permuting the order of the electric fields in Eq. (2.19), leave the $\chi_{\rho\sigma\tau\nu}^{(3)}$ unchanged. The factor $6/n!$, with n equal to the number of identical frequencies, accounts for the fact that each distinct permutation contributes to the polarization $P_{\rho}^{(3)}(\omega_0, r)$.

Symmetry Properties of $\chi^{(3)}$

The third-order susceptibility or 'chi-three' is a fourth-rank tensor containing 81 elements of the form $\chi_{\rho\sigma\tau\nu}^{(3)}(-\omega_0, \omega_1, \omega_2, \omega_3)$. Symmetry restrictions, however, will limit the number of the elements that are independent and nonvanishing. We have already mentioned in the preceding section the intrinsic symmetry of $\chi_{\rho\sigma\tau\nu}^{(3)}$ with respect to permutation of the pairs $(1,\sigma)$, $(2,\tau)$, $(3,\tau)$. $\chi^{(3)}$ must transform according to the macroscopic symmetry properties of the medium. For a crystal, this means that $\chi^{(3)}$ must be unchanged by any of the symmetry operations appropriate to the crystal. Butcher has examined these restrictions and Flytzanis tabulated the results for different crystal classes and for isotropic media such as liquids or gases. In the latter case there are 21 nonzero elements of which only 3 are independent. They are

$$\chi_{1111}^{(3)} = \chi_{xxxx}^{(3)} = \chi_{yyyy}^{(3)} = \chi_{zzzz}^{(3)}$$

$$\chi_{1122}^{(3)} = \chi_{xxyy}^{(3)} = \chi_{xxzz}^{(3)} = \chi_{yyxx}^{(3)} = \chi_{yyzz}^{(3)} = \chi_{zzxx}^{(3)} = \chi_{zzyy}^{(3)}$$

$$\chi_{1212}^{(3)} = \chi_{xyxy}^{(3)} = \chi_{xzxz}^{(3)} = \chi_{yxyx}^{(3)} = \chi_{yzyz}^{(3)} = \chi_{zxzx}^{(3)} = \chi_{zyzy}^{(3)}$$

$$\chi_{1221}^{(3)} = \chi_{xyyx}^{(3)} = \chi_{xzzx}^{(3)} = \chi_{yxxy}^{(3)} = \chi_{yzzz}^{(3)} = \chi_{zxxz}^{(3)} = \chi_{zyyz}^{(3)}$$

$$\chi_{1111}^{(3)} = \chi_{1122}^{(3)} + \chi_{1212}^{(3)} + \chi_{1221}^{(3)} \quad (2.20)$$

The combination of the permutation and isotropic restriction greatly simplifies the summations in Eq.(2.19) and, in the general case of four wave mixing, we obtain

$$\begin{aligned} P^{(3)}(r, \omega_0) = & 6 [\chi_{1122}^{(3)}(\omega_1, \omega_2, \omega_3) \hat{e}_1 (\hat{e}_2 \cdot \hat{e}_3) \\ & + \chi_{1212}^{(3)}(\omega_1, \omega_2, \omega_3) \hat{e}_2 (\hat{e}_1 \cdot \hat{e}_3) \\ & + \chi_{1221}^{(3)}(\omega_1, \omega_2, \omega_3) \hat{e}_3 (\hat{e}_1 \cdot \hat{e}_2)] \\ & \times E(1)E(2)E(3) \exp[i(k_1 + k_2 + k_3) \cdot r] \end{aligned} \quad (2.21)$$

where \hat{e}_i is the unit polarization vector of $E(i)$.

For CARS, two of the frequencies are identical so we divide by 2! and also equate $\chi_{1122}^{(3)}$ to $\chi_{1212}^{(3)}$ because of permutation symmetry. This gives

$$\begin{aligned} P^{(3)}(r, \omega_0) = & [6\chi_{1122}^{(3)}(\omega_1, \omega_1, -\omega_2) \hat{e}_1 (\hat{e}_1 \cdot \hat{e}_2) + 3\chi_{1221}^{(3)}(\omega_1, \omega_1, -\omega_2) \hat{e}_2] \\ & \times E(1)^2 E(2)^* \exp [i(2k_1 - k_2) \cdot r]. \end{aligned} \quad (2.22)$$

If $\hat{e}_1 = \hat{e}_2$, then

$$\begin{aligned}
\chi_{\text{CARS}}^{(3)} &= 6\chi_{1122}^{(3)} + 3\chi_{1221}^{(3)} \\
&= 3\chi_{1111}^{(3)}(\omega_1, \omega_1, -\omega_2).
\end{aligned} \tag{2.23}$$

For perpendicular polarizations $\hat{e}_1 \perp \hat{e}_2$ we have

$$\chi_{\text{CARS}}^{(3)} = 3\chi_{1221}^{(3)}(\omega_1, \omega_1, -\omega_2) \tag{2.24}$$

Thus the parallel and perpendicular polarization measurements suffice to completely determine all elements of the macroscopic susceptibility tensor.

Stimulated Raman scattering is also known to depend upon the third-order susceptibility. The third-order polarization in this case can be written as

$$\begin{aligned}
P^{(3)}(r, \omega_2) &= [6\chi_{1122}^{(3)}(\omega_2, \omega_1, -\omega_1)\hat{e}_2 + 6\chi_{1212}^{(3)}(\omega_2, \omega_1, -\omega_1)\hat{e}_1(\hat{e}_1 \cdot \hat{e}_2) \\
&\quad + 6\chi_{1221}^{(3)}(\omega_2, \omega_1, -\omega_1)\hat{e}_1(\hat{e}_1 \cdot \hat{e}_2)] E(1)E(2)^*E(2) \exp(ik_2 r)
\end{aligned} \tag{2.25}$$

For parallel polarization $\hat{e}_1 = \hat{e}_2$ then

$$\chi_{\text{SRS}} = 6(\chi_{1122}^{(3)} + \chi_{1212}^{(3)} + \chi_{1221}^{(3)}) = 6\chi_{1111}^{(3)}(\omega_2, \omega_1, -\omega_1) \tag{2.26}$$

In the case of stimulated Raman loss, SRL, the polarization component at ω_1 is of interest and the corresponding expression is

$$\begin{aligned}
P^{(3)}(r, \omega_1) &= 6\chi_{1111}^{(3)}(\omega_1, \omega_2, -\omega_2)E_1E_2E_2^* \exp(ik_1 r) \\
&= \chi_{\text{SRL}} E_1 E_2 E_2^* \exp(ik_1 r)
\end{aligned} \tag{2.27}$$

CARS Amplitudes

The nonlinear polarization $P^{(3)}(r,t)$ at frequency ω_0 acts as a source term in Maxwell's equation to produce an electromagnetic wave $E(r,t)$ at ω_0 , where

$$\frac{\partial^2 E(r,\omega)}{\partial z^2} - \left(\frac{\omega_3}{c}\right)^2 \epsilon_3 E(r,\omega_3) = 4\pi \left(\frac{\omega_3}{c}\right) P^{(3)}(r,\omega_3) \quad (2.28)$$

where

$$P^{(3)}(r,\omega_3) = \chi_{\text{CARS}} E_1^2 E_2^* \exp[i(2k_1 - k_2)r] \quad (2.29)$$

If we consider the driving fields to be plane waves with parallel propagation vectors aligned along the space-fixed z axis, then we can assume a solution

$$E = \hat{e}_{\text{CARS}} E_3^0 \exp[ik_3 z] \quad (2.30)$$

where \hat{e}_{CARS} is the unit polarization vector in the direction of the CARS field, then Eq. (2.28) becomes

$$\frac{\partial^2 E(3)}{\partial z^2} + 2ik_3 \frac{\partial E(3)}{\partial z} = -4\pi \left(\frac{\omega_3}{c}\right)^2 \chi_{\text{CARS}} E(1)^2 E(2)^* \exp(i\Delta k z) \quad (2.31)$$

with

$$\Delta k = 2k_1 - k_2 - k_3 \quad (2.32)$$

We assume that Δk is small and that E_3^0 is a slowly varying function of

z so that the second derivative can be neglected. If we assume that $E_3^0 = 0$ at $z = 0$, then we have, for a propagation distance from 0 to L ,

$$E_3^0 = \frac{-3i\pi\omega_3}{2c} E^2(\omega_1)E^*(\omega_2) \int_0^L \chi^{(3)} \exp(i\Delta kz) dz \quad (2.33)$$

When $\Delta k = 0$ the beams are referred to as phase-matched. Therefore, we have

$$E(\omega_0, L) = \frac{-3i\pi\omega_0}{2c} E^2(\omega_1)E^*(\omega_2)\chi_{\text{CARS}} L \quad (2.34)$$

By using the fact that the intensity is related to the field amplitude,

$$I(\omega) = (c/8\pi) |E|^2, \quad (2.35)$$

the CARS intensity can be expressed as

$$I_0(L) = (12\pi^2\omega_0/c^2)^2 I_1 I_2 |\chi_{\text{CARS}}^{(3)}|^2 L^2, \quad (2.36)$$

where I_1 is the intensity of the beam at frequency ω_1 .

This plane wave result for the intensity of the CARS reveals many of the characteristic features of the coherent anti-Stokes Raman scattering process. The signal intensity scales as the product of the Stokes laser intensity I_2 and the square of the pump laser intensity I_1 . Hence CARS signals will have large gains by using pulsed lasers

with high peak powers. I_3 depends upon the square of the bulk susceptibility $|\chi^{(3)}|^2$ and hence is proportional to the square of the sample density.

Equation (2.36) also indicates that the CARS signal intensity should increase as the square of the sample length indefinitely. This behavior is a consequence of the assumption that the dispersion of the sample is zero. If we take into account the index of refraction variation in the medium, the integral in Eq.(2.33) becomes

$$\int_0^L \chi^{(3)} \exp(i \Delta k z) dz = \chi^{(3)} L \frac{\sin(\Delta k L/2)}{\Delta k L/2} \quad (2.37)$$

The CARS intensity, therefore, becomes

$$I_0(L) = \left(\frac{12\pi^2 \omega_0^2}{c^2} \right)^2 I_1 I_2 |\chi_{\text{CARS}}|^2 L^2 \left[\frac{\sin(\Delta k L/2)}{\Delta k L/2} \right]^2 \quad (2.38)$$

For the $\Delta k \neq 0$, the intensity becomes periodic with path length L . The coherence L_c can be defined as the path length to reach a maximum intensity, i.e.,

$$L_c = \pi/\Delta k. \quad (2.39)$$

The intensity at this coherence length L_c is reduced by a factor of $(2/\pi)^2$ compared to the phase matched case. By expanding the index of refraction as a power series in frequency, L_c becomes¹⁶

$$L_c = \frac{\pi c}{(\omega_1 - \omega_2)^2} \left[2 \frac{\partial n}{\partial \omega} + \omega_1 \frac{\partial^2 n}{\partial \omega^2} \right]^{-1}. \quad (2.40)$$

The coherence length for most gases is of the order of 100 cm at STP and is inversely proportional to density. Since the term in square brackets in Eq.(2.38) is nearly equal to 1 for $L < \approx L_c/3$, Eq.(2.26) is a good approximation to the signal intensity for most gas samples.

For condensed phases, dispersion effects are much larger and L_c is of the order of millimeters so that the maximum CARS intensity allowed by Eq.(2.38) becomes coherence length limited. To increase L_c , $\Delta k = 2k_1 - k_2 - k_3$ is usually reduced in liquids by crossing the beam at a phase matching angle θ , as shown in Fig.2.1. This angle θ is called the phase-matching angle and in most case is of the order of $1-3^\circ$. In condensed phases, the CARS signal generation consequently becomes limited by the finite spatial overlap of the crossed ω_1 and ω_2 beams.

Microscopic Form of $\chi^{(3)}$

The coherent anti-Stokes Raman scattering process that generates the anti-Stokes signal beam at $\omega_0 = \omega_1 - \omega_2 + \omega_3$ is greatly enhanced when $\omega_1 - \omega_2 = \omega_{rg}$, the frequency of a Raman allowed transition between molecular energy states g and r . This resonance behavior comes from Raman resonances in $\chi^{(3)}$. In order to understand the nonlinear effect caused by the third order susceptibility $\chi^{(3)}$, one has to establish the connection between the macroscopic bulk polarization and

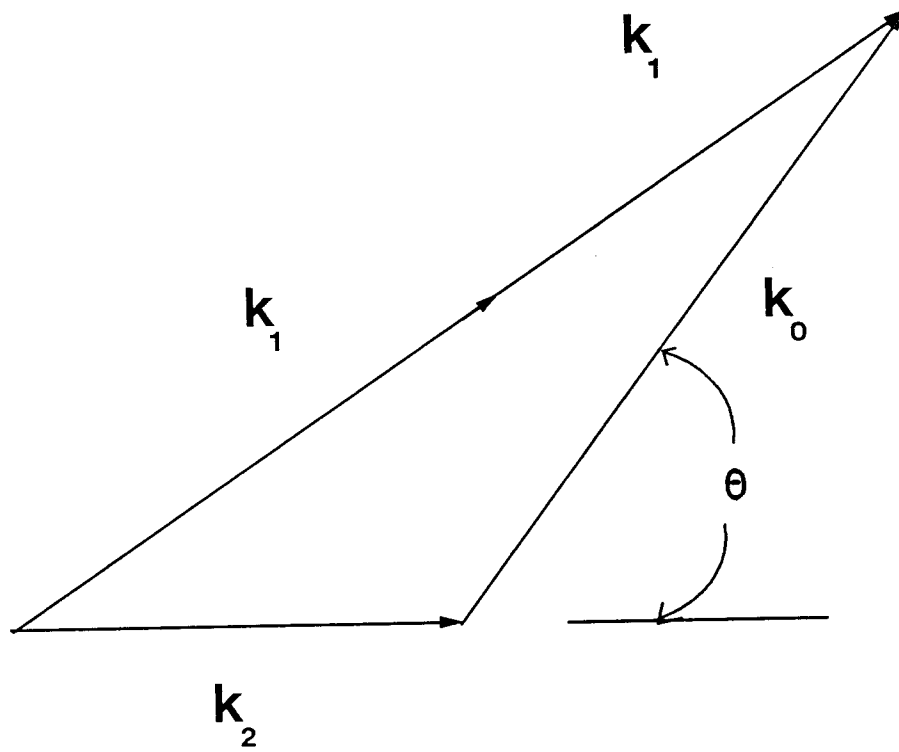


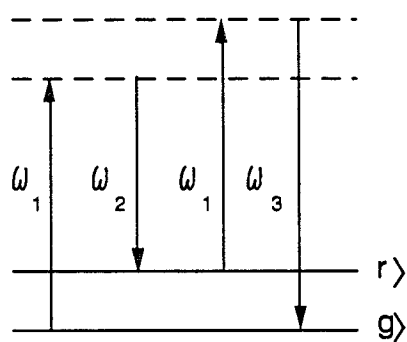
Figure 2.1. Coherent anti-Stokes Raman scattering phase-matching diagram.

the microscopic molecular properties of the material.

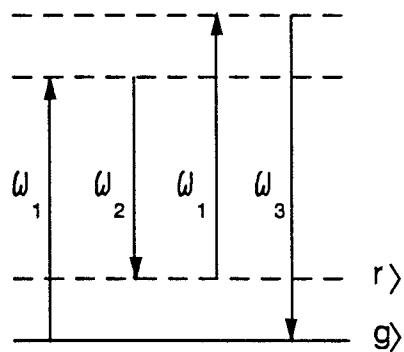
The expression of third order susceptibility $\chi^{(3)}$ can be obtained by a quantum mechanical time-dependent perturbation theory calculation. Such a treatment⁸ shows that each of the 81 Cartesian components of the fourth-rank tensor $\chi^{(3)}$ is given by the sum of 24 terms, each of which is itself a threefold sum over all molecular states, with each element of the threefold sum a product of dipole matrix elements divided by a product of frequency factors. For the CARS process, in which an electric field at frequency $\omega_0 = \omega_1 - \omega_2 + \omega_3$ is produced by the interaction of fields ω_1 , ω_2 , and ω_3 , the components of χ are given in Eq. (2.41).

The Raman resonant enhancement happens when the frequency factors such as $\omega_{kg} - (\omega_1 - \omega_2)$ occur in the denominator of the second term in the expression for $\chi_{\rho\sigma\tau\nu}$. When $k = r$ this frequency factor becomes $\omega_{rg} - (\omega_1 - \omega_2)$, where r and g are the two molecular states connected by Raman allowed transition. As $\omega_1 - \omega_2 \rightarrow \omega_{rg}$, the denominator in the second term in the expression in Eq. (2.41) approaches zero. The denominators such as $\omega_{jg} - \omega_1$ give rise to one-photon resonances in $\chi_{\rho\sigma\tau\nu}$. The effect of these one-photon resonances is termed resonance CARS. Other frequency factors like $\omega_{kg} - (\omega_1 - \omega_3)$ represent two-photon absorption resonances in $\chi_{\rho\sigma\tau\nu}$. The resonant and nonresonant contributions to $\chi_{\rho\sigma\tau\nu}$ are illustrated in Figure 2.2.

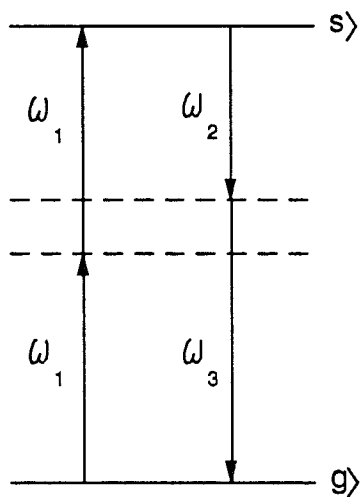
Thus $\chi^{(3)}$ goes to infinity at various one photon, Raman and two photon absorption resonances. This unphysical characteristic was modified later by Orr and Ward by applying perturbation theory treatment on $\chi^{(3)}$. However, we are only interested in Raman resonances



Coherent Anti-Stokes Raman Scattering



Non-Resonant Four Wave Mixing



Two-Photon Absorption

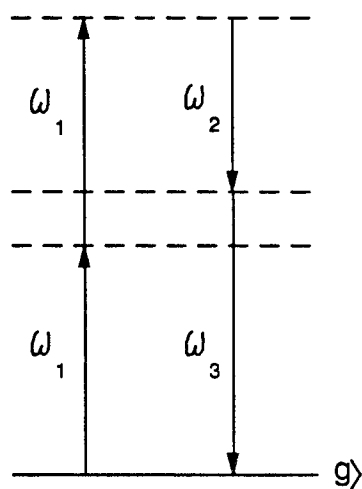
Non-Resonant Contributions to $\chi^{(3)}$

Figure 2.2. Energy-level schematic for several processes discussed in the text.

$$\begin{aligned}
\chi_{\rho\sigma\tau\nu}^{(3)} = N \hbar^{-3} \sum_{j,k,l} & \left[\frac{\rho\tau\nu\sigma}{(\omega_{jg} - \omega_1)(\omega_{kg} - \omega_1 - \omega_3)(\omega_{lg} - \omega_0)} + \frac{\rho\nu\tau\sigma}{(\omega_{jg} - \omega_1)(\omega_{kg} - \omega_1 - \omega_2)(\omega_{lg} - \omega_0)} \right. \\
& + \frac{\rho\tau\nu\sigma}{(\omega_{jg} - \omega_3)(\omega_{kg} - \omega_1 - \omega_3)(\omega_{lg} - \omega_0)} + \frac{\rho\nu\sigma\tau}{(\omega_{jg} + \omega_2)(\omega_{kg} - \omega_1 + \omega_2)(\omega_{lg} - \omega_0)} \\
& + \frac{\rho\sigma\tau\nu}{(\omega_{jg} - \omega_3)(\omega_{kg} - \omega_3 + \omega_2)(\omega_{lg} - \omega_0)} + \frac{\rho\sigma\nu\tau}{(\omega_{jg} + \omega_2)(\omega_{kg} - \omega_3 + \omega_2)(\omega_{lg} - \omega_0)} \\
& + \frac{\tau\rho\nu\sigma}{(\omega_{jg} - \omega_1)(\omega_{kg} - \omega_1 - \omega_3)(\omega_{lg} - \omega_2)} + \frac{\nu\rho\tau\sigma}{(\omega_{jg} - \omega_1)(\omega_{kg} - \omega_1 + \omega_2)(\omega_{lg} + \omega_3)} \\
& + \frac{\tau\rho\nu\sigma}{(\omega_{jg} - \omega_3)(\omega_{kg} - \omega_1 - \omega_2)(\omega_{lg} - \omega_2)} + \frac{\nu\rho\sigma\tau}{(\omega_{jg} - \omega_2)(\omega_{kg} - \omega_1 + \omega_2)(\omega_{lg} + \omega_3)} \\
& + \frac{\sigma\rho\tau\nu}{(\omega_{jg} - \omega_3)(\omega_{kg} - \omega_1 + \omega_2)(\omega_{lg} + \omega_1)} + \frac{\sigma\rho\nu\tau}{(\omega_{jg} + \omega_2)(\omega_{kg} - \omega_3 + \omega_2)(\omega_{lg} + \omega_1)} \\
& + \frac{\tau\nu\rho\sigma}{(\omega_{jg} - \omega_1)(\omega_{kg} - \omega_3 - \omega_2)(\omega_{lg} - \omega_2)} + \frac{\nu\tau\rho\sigma}{(\omega_{jg} - \omega_1)(\omega_{kg} + \omega_3 - \omega_2)(\omega_{lg} + \omega_3)} \\
& + \frac{\tau\sigma\rho\nu}{(\omega_{jg} - \omega_3)(\omega_{kg} + \omega_1 - \omega_2)(\omega_{lg} - \omega_2)} + \frac{\nu\sigma\rho\tau}{(\omega_{jg} - \omega_2)(\omega_{kg} + \omega_1 + \omega_3)(\omega_{lg} + \omega_3)} \\
& + \frac{\sigma\tau\rho\nu}{(\omega_{jg} - \omega_3)(\omega_{kg} + \omega_1 - \omega_2)(\omega_{lg} + \omega_1)} + \frac{\sigma\nu\rho\tau}{(\omega_{jg} + \omega_2)(\omega_{kg} + \omega_1 + \omega_3)(\omega_{lg} + \omega_1)} \\
& + \frac{\tau\nu\sigma\rho}{(\omega_{jg} + \omega_0)(\omega_{kg} + \omega_3 - \omega_2)(\omega_{lg} - \omega_2)} + \frac{\nu\tau\sigma\rho}{(\omega_{jg} + \omega_0)(\omega_{kg} + \omega_3 - \omega_2)(\omega_{lg} + \omega_3)} \\
& + \frac{\tau\sigma\nu\rho}{(\omega_{jg} + \omega_0)(\omega_{kg} + \omega_1 - \omega_2)(\omega_{lg} - \omega_2)} + \frac{\nu\sigma\tau\rho}{(\omega_{jg} + \omega_0)(\omega_{kg} + \omega_1 + \omega_3)(\omega_{lg} + \omega_3)} \\
& \left. + \frac{\sigma\tau\nu\rho}{(\omega_{jg} + \omega_0)(\omega_{kg} + \omega_1 - \omega_2)(\omega_{lg} + \omega_1)} + \frac{\sigma\nu\tau\rho}{(\omega_{jg} + \omega_0)(\omega_{kg} + \omega_1 + \omega_3)(\omega_{lg} + \omega_1)} \right]
\end{aligned}
\tag{2.41}$$

in $\chi^{(3)}$, in which the expression is much simpler and the Eq.(2.41) is adequate if a damping of the molecular states j , k and l is introduced. That is, we make the various Raman resonant frequency denominators complex by replacing ω_{ng} , where $n = j, k, l$ by Ω_{ng} , where

$$\Omega_{ng} = \omega_{ng} - i\Gamma_{ng} \quad (2.42)$$

and Γ_{ng} is the damping constant.

This replacing leads quite naturally to a separation of $\chi^{(3)}$ into resonant and nonresonant contributions

$$\chi^{(3)} = \chi' + i\chi'' + \chi^{NR} \quad (2.43)$$

where $\chi' + i\chi''$ is the resonant part and χ^{NR} is the nonresonant part.

The perturbation theory treatment shows how Raman resonances appear in $\chi^{(3)}$. But the next question is how the amplitude of $\chi^{(3)}$ at these resonances connects to the spontaneous Raman scattering cross section $d\sigma/d\Omega$. We will use the semi-classical oscillator model to derive the important relations. This simplest approach identifies the resonant frequency ω_{rg} as the frequency of a damped harmonic oscillator and assumes that the linear polarization theory of Placzek¹⁴ is valid. The linear polarizability tensor α of the molecule is given by the expansion

$$\alpha = \alpha_0 + \left(\frac{\partial \alpha}{\partial q} \right)_0 q + \dots \quad (2.44)$$

where q is the harmonic oscillator coordinate. The equation of motion for this oscillator in the presence of a driving electric field E can be written as¹⁹:

$$\frac{\partial^2 q}{\partial t^2} + \Gamma_{rg} \frac{\partial q}{\partial t} + \omega_{rg}^2 q = \frac{1}{2m} \left(\frac{\partial \alpha}{\partial q} \right)_0 E^2 \Delta_{rg} \quad (2.45)$$

Here Δ is the population difference between the two oscillator levels, m is the reduced mass of the oscillator, and Γ is the damping constant which is related to the dephasing time: $\Gamma = 1/T_2$.

Writing the field in terms of its Fourier components with real fields at frequencies $\omega_1 - \omega_2$

$$\begin{aligned} \frac{\partial^2 q}{\partial t^2} + \Gamma_{rg} \frac{\partial q}{\partial t} + \omega_{rg}^2 q = \frac{1}{2m} \left(\frac{\partial \alpha}{\partial q} \right)_0 E(\omega_1, r) E^*(\omega_2, r) \Delta \\ \times \exp\{i[(k_1 - k_2) \cdot r - (\omega_1 - \omega_2)t]\} \end{aligned} \quad (2.46)$$

for which the solution is

$$q(\omega_1 - \omega_2) = \frac{1}{8m} \left(\frac{\partial \alpha}{\partial q} \right)_0 \frac{E(\omega_1, r) E^*(\omega_2, r) \exp\{i[(k_1 - k_2) \cdot r - (\omega_1 - \omega_2)t]\}}{[\omega_{rg}^2 - (\omega_1 - \omega_2)^2 - i\Gamma_{rg}(\omega_1 - \omega_2)]} \quad (2.47)$$

The Raman contribution to the nonlinear polarization is given by

$$P = N q(\omega_1 - \omega_2) \left(\frac{\partial \alpha}{\partial q} \right)_0 E \quad (2.48)$$

where N is the molecular number density. Inserting the solution of the equation of motion for q gives

$$P(r, t) = \frac{N\Delta}{16m} \left(\frac{\partial \alpha}{\partial q} \right)_0 \left(\frac{\partial \alpha}{\partial q} \right)_0 \frac{E(\omega_1, r)E(\omega_2, r)E(\omega_1, r)}{[\omega_{rg}^2 - (\omega_1 - \omega_2)^2 - i\Gamma_{rg}(\omega_1 - \omega_2)]} \\ \times \exp\{i[2k_1 - k_2] \cdot r - \omega_0 t\} + \text{cc.} \quad (2.49)$$

If we assume that the laser fields have parallel field vectors and parallel propagation vectors aligned along the space-fixed z axis, Eq. (2.47) becomes

$$P(z, t) = \frac{3N\Delta}{16m} \left(\frac{\partial \alpha}{\partial q} \right)_0^2 \frac{E^2(\omega_1)E^*(\omega_2) \exp\{[(2k_1 - k_2)z - \omega_0 t]\}}{[\omega_{rg}^2 - (\omega_1 - \omega_2)^2 - i\Gamma_{rg}(\omega_1 - \omega_2)]} + \text{c.c.}, \quad (2.50)$$

Comparing Eqs. (2.50) and (2.29), we get:

$$\chi^{(3)}(-\omega_0, \omega_1, -\omega_2, \omega_1) = \frac{N\Delta}{2m} \left(\frac{\partial \alpha}{\partial q} \right)_0^2 \frac{1}{[\omega_{rg}^2 - (\omega_1 - \omega_2)^2 - i\Gamma_{rg}(\omega_1 - \omega_2)]} \quad (2.51)$$

For liquids and gases the susceptibility is averaged over all orientations of the molecules. The relation between Raman cross section $d\sigma/d\Omega$ and the Raman matrix element $(\partial\alpha/\partial q)_0^2$ is:

$$\left(\frac{\partial \alpha}{\partial q} \right)_0^2 = \left(\frac{2m\omega_{rg} c^4}{\hbar\omega_2^4} \right) \left(\frac{d\sigma}{d\Omega} \right) \quad (2.52)$$

By using this one finds:

$$\chi^{(3)}(-\omega_0, \omega_1, -\omega_2, \omega_1) = \frac{Nc^4\Delta}{\hbar\omega_2^4} \frac{d\sigma}{d\Omega} \frac{\omega_{rg}}{[\omega_{rg}^2 - (\omega_1 - \omega_2)^2 - i\Gamma_{rg}(\omega_1 - \omega_2)]} \quad (2.53)$$

At resonance $\omega_1 - \omega_2 = \omega_{rg}$

$$|\chi^{(3)}|^2 = \left(\frac{Nc^4\Delta}{\hbar\omega_2^4}\right)^2 \left(\frac{d\sigma}{d\Omega}\right)^2 \frac{1}{\Gamma_{rg}^2} \quad (2.54)$$

Thus the magnitude of a CARS signal at resonance depends on the square of the magnitude of the Raman cross section for that Raman transition, as well as on the square of the difference in population between the states r and g, Δ_{rg} , and on the square of the Raman transition linewidth Γ_{rg} .

Selection Rules

The selection rules for CARS are seen by examining the expectation value for a susceptibility element which is resonant at a frequency ω_{rg} corresponding to a transition between vibration rotation states r, J and g, J'. Neglecting χ_{NR} and using the population difference between the two states, for the molecule in the laboratory frame one can write:

$$\langle rJ | \chi^{(3, \text{mol})}(\omega_1, \omega_1, \omega_2) | gJ' \rangle = \frac{\Delta}{24\hbar} \frac{\langle rJ | \alpha_{\alpha\beta}^A | gJ' \rangle \langle rJ' | \alpha_{\gamma\delta}^S | rJ \rangle + (\beta \leftrightarrow \gamma)}{\omega_J - \omega_1 + \omega_2 - i\Gamma_J} \quad (2.55)$$

To express these integrals in term of the molecular axis system we make use of the transformation relation

$$\alpha_{\alpha\beta} = \sum_{\alpha',\beta'} \phi_{\alpha\alpha'} \phi_{\beta\beta'} \alpha_{\alpha'\beta'} \quad (2.56)$$

where the ϕ 's are direction cosines. If the vibrational and rotational wave functions are assumed separable, (2.53) becomes

$$\begin{aligned} \langle rJ | \chi^{(3,\text{mol})} | gJ' \rangle &= \frac{\Delta}{\omega_J - \omega_1 + \omega_2 - i\Gamma_J} \sum_{\alpha,\beta,\gamma,\delta} [\langle r | \alpha_{\alpha,\beta}^A | g \rangle \langle g | \alpha_{\gamma,\delta}^S | r \rangle \\ &\times \langle J | \phi_{\alpha\alpha'} \phi_{\beta\beta'} | J' \rangle \langle J' | \phi_{\gamma\gamma'} \phi_{\delta\delta'} | J \rangle + (\beta \leftrightarrow \gamma)] \end{aligned} \quad (2.57)$$

Each integral for a given term in Eq. (2.55) must be invariant to any molecular symmetry operation to have a non-zero contribution to the susceptibility. For the vibrational part, $\alpha_{\alpha,\beta}^A$ and $\alpha_{\gamma,\delta}^S$ must belong to the same symmetry species as normal coordinate q since $\psi_r(q)\psi_g(q)$ transforms as q . Therefore, the vibrational selection rules for CARS are identical to those for spontaneous Raman spectroscopy. Furthermore, the two rotational integrals in Eq. (2.55) yield exactly the same selection rules as in the conventional Raman case.

Spectral Line Shape

Because the CARS intensity is proportional to $|\chi_{\text{CARS}}|^2$, interference can occur between the different contributions contained in Eq. (2.51). The 1111 Cartesian component of the resonant contribution $\chi' + i\chi''$ can be identified with $\chi^{(3)}$ given in Eq. (2.51).

By separating it into real and imaginary parts, one finds

$$\chi' = \frac{Nc^4 \Delta}{\hbar \omega_2^4} \frac{d\sigma}{d\Omega} \frac{\omega_{rg} [\omega_{rg}^2 - (\omega_1 - \omega_2)^2]}{[\omega_{rg}^2 - (\omega_1 - \omega_2)^2]^2 + \Gamma_{rg}^2 (\omega_1 - \omega_2)^2} \quad (2.58)$$

and

$$\chi'' = \frac{Nc^4 \Delta}{\hbar \omega_2^4} \frac{d\sigma}{d\Omega} \frac{\omega_{rg} \Gamma_{rg} (\omega_1 - \omega_2)}{[\omega_{rg}^2 - (\omega_1 - \omega_2)^2]^2 + \Gamma_{rg}^2 (\omega_1 - \omega_2)^2} \quad (2.59)$$

As assumed before χ^{NR} represents real and independent input field frequencies, so

$$\chi^{NR} = \text{const.} \quad (2.60)$$

The contributions of χ' and χ'' to $\chi^{(3)}$ are plotted in Fig. 2.3, while

$$|\chi^{(3)}|^2 = (\chi')^2 + (\chi'')^2 + (\chi^{NR})^2 + 2\chi' \chi^{NR} \quad (2.61)$$

is shown in Fig. 2.4. Because the frequency dependence of the CARS signal is determined by $|\chi^{(3)}|^2$, Fig. 2.4 shows the expected CARS line shape, which is asymmetric for $\chi^{NR} \neq 0$.

The high signal intensity is the major advantage of CARS spectroscopy over spontaneous Raman spectroscopy, but the nonresonant background contribution to the CARS signal is a major disadvantage. For small χ' and χ'' relative to χ^{NR} , due to a small Raman cross

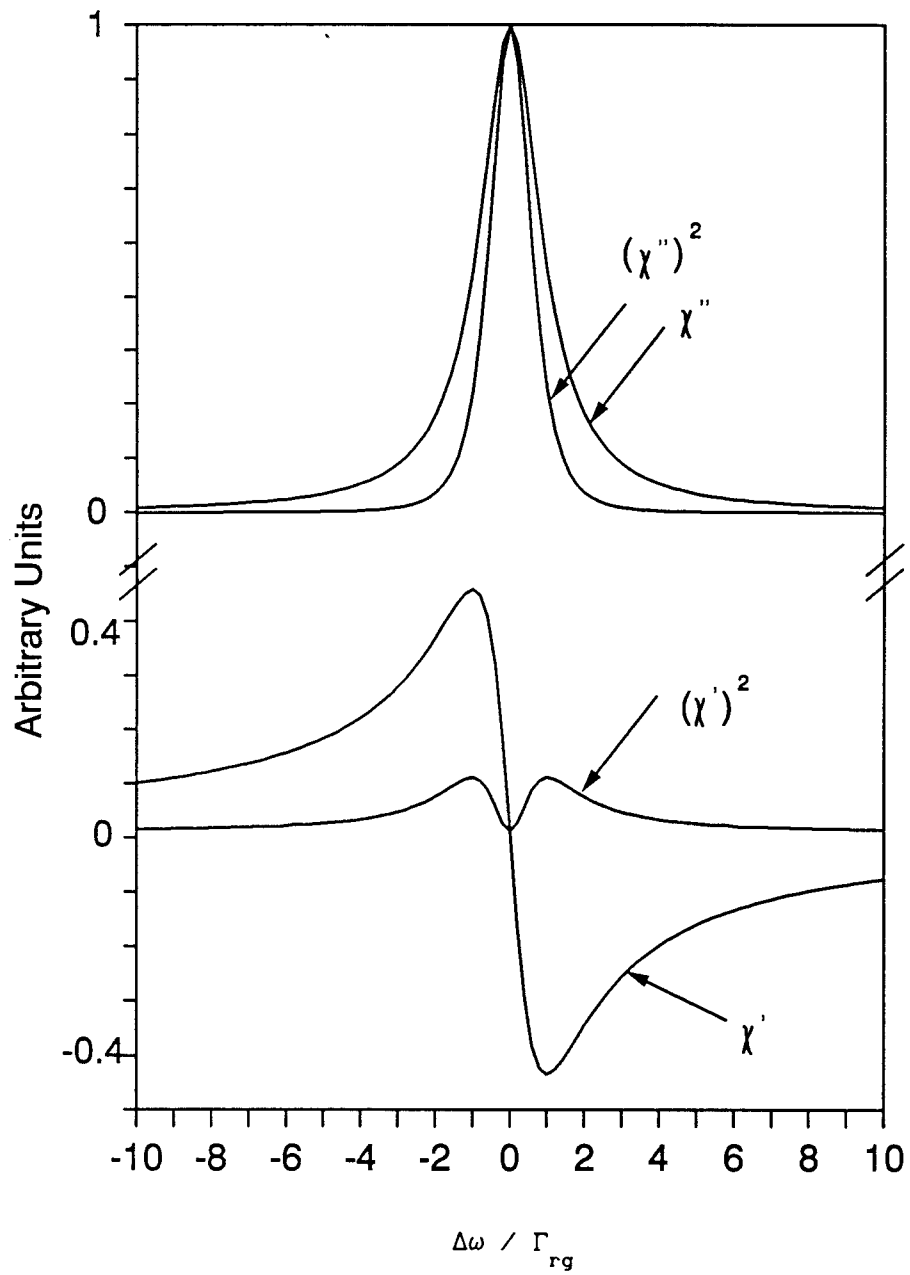


Figure 2.3. Real and imaginary components of the resonant third-order susceptibility $\chi^{(3)}$ in the region of the resonance.

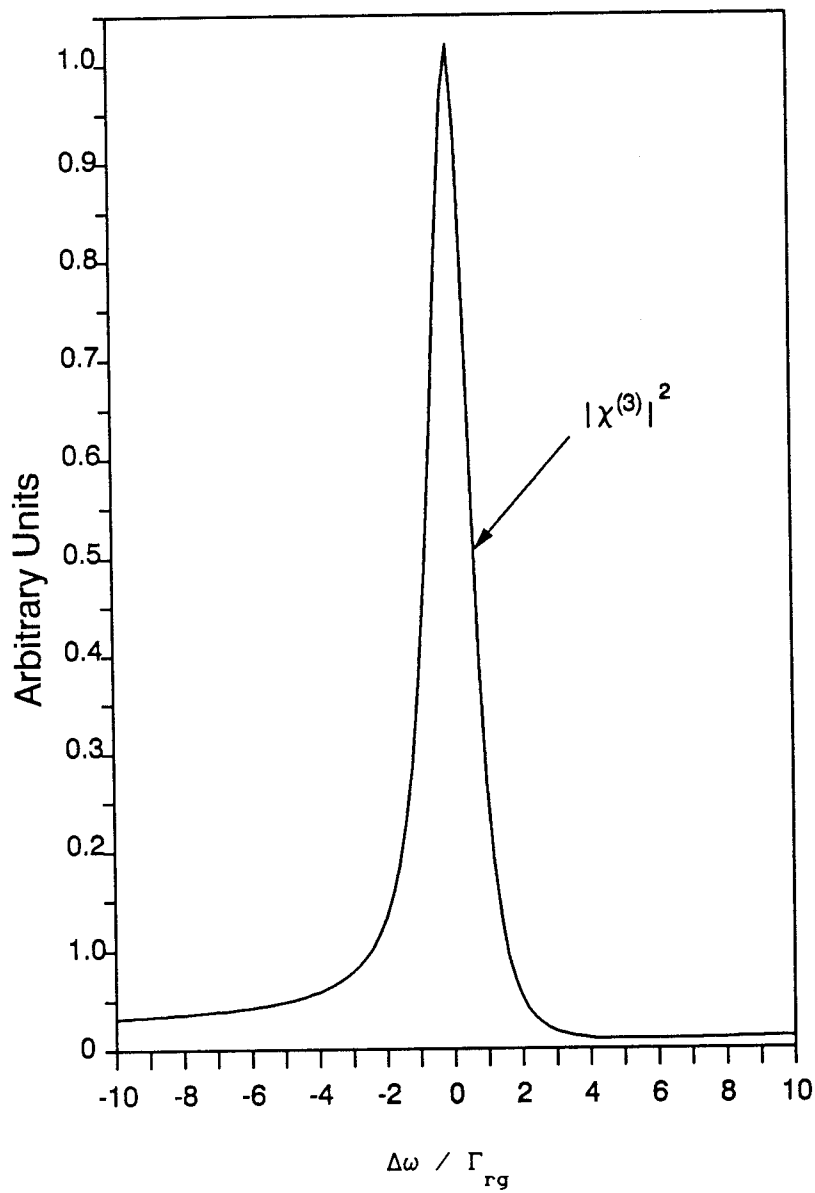


Figure 2.4. Square of the third-order susceptibility $\chi^{(3)}$ in the region of Raman resonance. $\chi^{NR} = 0.2$ is assumed.

section or low species concentration, Eq. (2.59) becomes

$$|\chi^{(3)}|^2 \cong (\chi^{\text{NR}})^2 + 2\chi'\chi^{\text{NR}} \quad (2.62)$$

In this case the nonresonant background $(\chi^{\text{NR}})^2$ can often be as large as or larger than $2\chi'\chi^{\text{NR}}$, limiting the signal-to-noise ratio in the spectrum.

The interference will be more serious in the case of several closely spaced Raman lines, for example, the rotational lines in a vibrational Q-branch Raman transition. Considering only two adjacent lines one can write

$$\begin{aligned} |\chi^{(3)}|^2 = & (\chi'_1)^2 + (\chi'_2)^2 + (\chi''_1)^2 + (\chi''_2)^2 + (\chi^{\text{NR}})^2 \\ & + 2\chi'_1\chi'_2 + 2\chi''_1\chi''_2 + 2\chi'_1\chi^{\text{NR}} + 2\chi'_2\chi^{\text{NR}} \end{aligned} \quad (2.63)$$

Obviously, when there are several closely spaced lines the CARS line shape function can become quite complicated.

So far we have discussed several basic aspects of CARS technique. The equations of CARS amplitudes, selection rules and the CARS spectral line shape derived from this section will be greatly helpful for understanding the experimental CARS spectra.

FREE JET EXPANSIONS

The supersonic free jet expansion is a widely used technique in gas phase spectroscopy since it allows gas samples to be cooled down

in an effective and simple way. The cooling is achieved by the expansion of a gas sample into a vacuum through a very small orifice. The cooling during the expansion is due to a redistribution of thermal energy of the equilibrium sample prior to expansion into the energy of mass flow of the jet. Figure 2.5 gives another way to visualize the temperature changes in a supersonic expansion. Temperature in a gas is described by the width of a Maxwell-Boltzmann velocity distribution and the relatively wide peak centered at $V = 0$ is characteristic of room temperature distribution. The second peak centered at $V = 550$ m/s represents the velocity distribution along the axis of the expansion at some point downstream of the nozzle. The line width contributions due to pressure broadening and the Doppler effect are greatly reduced in the jet system simply because the effective pressure is much lower and the gas flow is directional. The other feature of a supersonic free jet expansion is the relatively high collision rate during the early stage of expansion. Therefore clusters of interest, weakly bound molecular aggregates, can be formed in the initial steps of the expansion.

Levy²⁰ has described the redistribution of thermal energy in the expansion process in terms of conservation of enthalpy. If one assumes constant enthalpy per unit mass and h_0 is the enthalpy per unit mass in the reservoir, then

$$h_0 = h + u^2/2 \quad (2.64)$$

where h is the enthalpy per unit mass at some point downstream of the

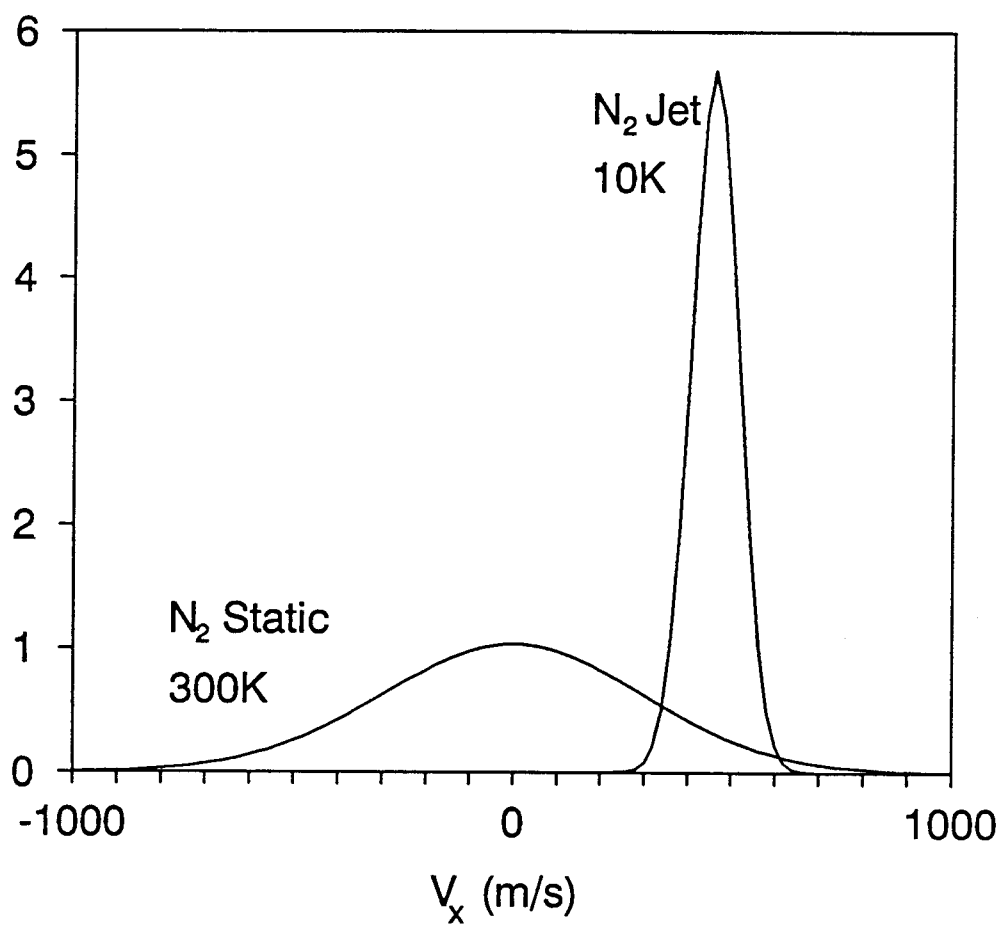


Figure 2.5. Normalized Maxwell-Boltzmann velocity distribution.

nozzle and u is the flow velocity.

For an ideal gas,

$$h_0 - h = C_p (T_0 - T) = \frac{\gamma}{\gamma - 1} r(T_0 - T) \quad (2.65)$$

where r is the gas constant per unit mass and $\gamma = C_p/C_v$, and C_p and C_v are the heat capacities per unit mass at constant pressure and volume respectively. T is the downstream temperature and T_0 is the reservoir temperature. Ratios of pressure, density and temperature are all related to the Mach number M ,

$$M = u/a \quad (2.66)$$

where u is the flow velocity and a is the local speed of sound.

For ideal gas the relation between the speed of sound and the local temperature T is given as:

$$a = (\gamma r T)^{1/2} \quad (2.67)$$

Combining equation (2.62) - (2.63) we get

$$\frac{T}{T_0} = \left(1 + \left(\frac{\gamma - 1}{2} \right) M^2 \right)^{-1} \quad (2.68)$$

where M is the Mach number. For an isentropic process in an ideal gas: $P = \text{const. } \rho^\gamma$. With this relationship and the ideal gas law, the

equation for density and pressure as a function of the Mach number can be written as

$$\frac{P}{P_0} = \left(1 + \left(\frac{\gamma-1}{2} \right) M^2 \right)^{\frac{\gamma}{1-\gamma}} \quad (2.69)$$

$$\frac{\rho}{\rho_0} = \left(1 + \left(\frac{\gamma-1}{2} \right) M^2 \right)^{\frac{\gamma}{1-\gamma}} \quad (2.70)$$

The Mach number as a function of the position along the expansion axis has been shown by Ashkenas and Sherman,²¹ to be described by the empirical relation

$$M = A \left(\frac{X - X_0}{D} \right)^{\gamma - 1} - \frac{1}{2} \left(\frac{\gamma + 1}{\gamma - 1} \right) \bigg/ A \left(\frac{X - X_0}{D} \right)^{\gamma - 1} \quad (2.71)$$

where A and X_0 are constants which are dependent on γ and D is the diameter of the nozzle orifice. Figure 2.6 shows these results in diagram form which give us a idea of how the velocity, temperature, density and pressure changes during the expansion.

CLASSICAL HOMOGENEOUS NUCLEATION THEORY

Molecular clusters, formed from nucleation processes, are a primary object of our research interests. Therefore, it is important for us to understand the mechanism of the nucleation process and the critical conditions for forming small molecular cluster. In this

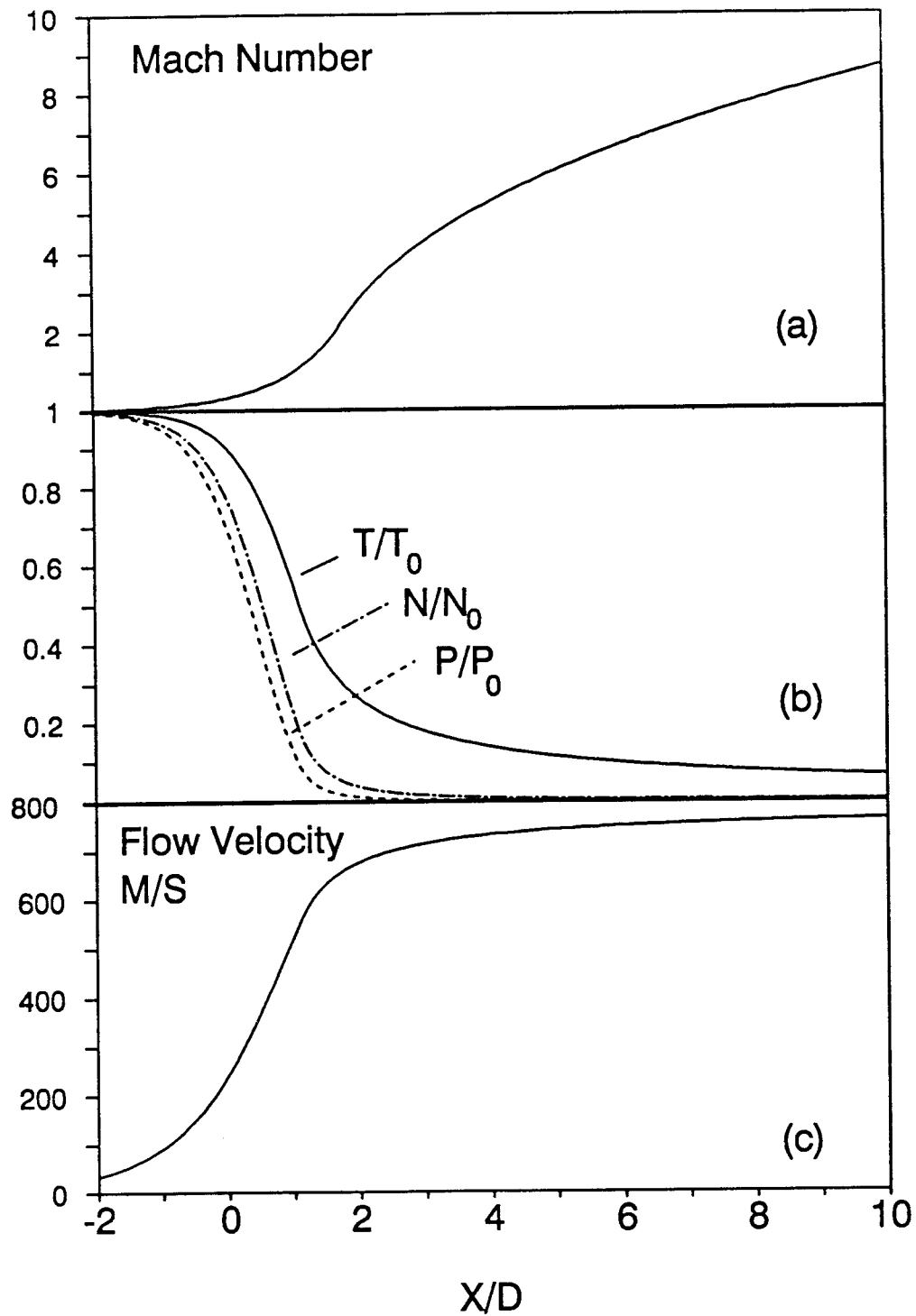


Figure 2.6. Jet profiles as a function of position along the expansion axis as calculated for a neat nitrogen with $P_0 = 10$ atm and $T_0 = 300$ K.

section a brief discussion of the thermodynamic and kinetic aspects of nucleation processes and of condensation in the free jet expansion are presented.

Thermodynamic Aspects

For a system with vapor-liquid equilibrium one can picture, as indicated in Fig.2.7, a small droplet of condensed phase B which is surrounded by the vapor phase A, and for which the total free energy change on droplet formation is given by²²

$$\Delta G_T = \frac{4}{3} \pi r^3 \Delta G_v + 4\pi r^2 \sigma \quad (2.72)$$

Here, ΔG_v is the bulk free energy difference per volume of condensed phase between the vapor and the liquid phases, r is the radius of the small droplet and σ is the vapor-liquid surface tension.

Considering the chemical potential and vapor pressure between phases A and B, one has

$$\Delta \mu_{A \rightarrow B} = -RT \ln \left(\frac{p_A}{p_B} \right) \quad (2.73)$$

So that

$$\Delta G_v = - \frac{RT}{V_m} \ln \left(\frac{p_A}{p_B} \right) \quad (2.74)$$

where V_m is the molar volume of the liquid at the temperature under consideration.

The droplet will grow from the vapor only if its free energy decreases below a critical value so that ΔG_T is equal to or greater than some critical value ΔG^* for the free-energy difference. As shown in Fig. 2.8, the plot of ΔG_T versus r reveals a maximum, which can be located by setting $\partial \Delta G_T / \partial r = 0$. From this the critical radius can be found

$$r^* = - \frac{2\sigma}{\Delta G_v} = \frac{2\sigma V_m}{RT \ln \left(\frac{p}{p_{\text{vap}}} \right)} \quad (2.75)$$

Consequently ΔG^* can be found by inserting the Eq.(2.75) into Eq.(2.72), yielding

$$\Delta G^* = \frac{16\pi\sigma^3}{3\Delta G_v^2} \quad (2.76)$$

It is instructive to note in Fig.2.8 the composition of the ΔG versus r curve in terms of the surface and bulk free energy contributions which are given in the figure as dashed curves. In the early stages of droplet formation, only after the critical size is reached does the bulk free energy term dominate and the droplet become theoretically stable. Thus it is a continual battle for small clusters of molecules to accrete enough bulk free energy to offset the surface effect, and as one shall see in the kinetics discussion, the probability of such a droplet becoming stable and growing is extremely remote for vapor pressure saturation ratios less than 1.0.

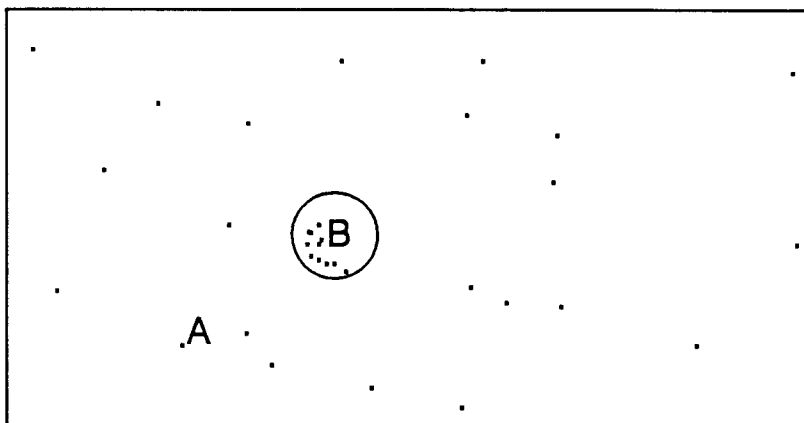


Figure 2.7. Small droplet of phase B suspended in host-phase A.

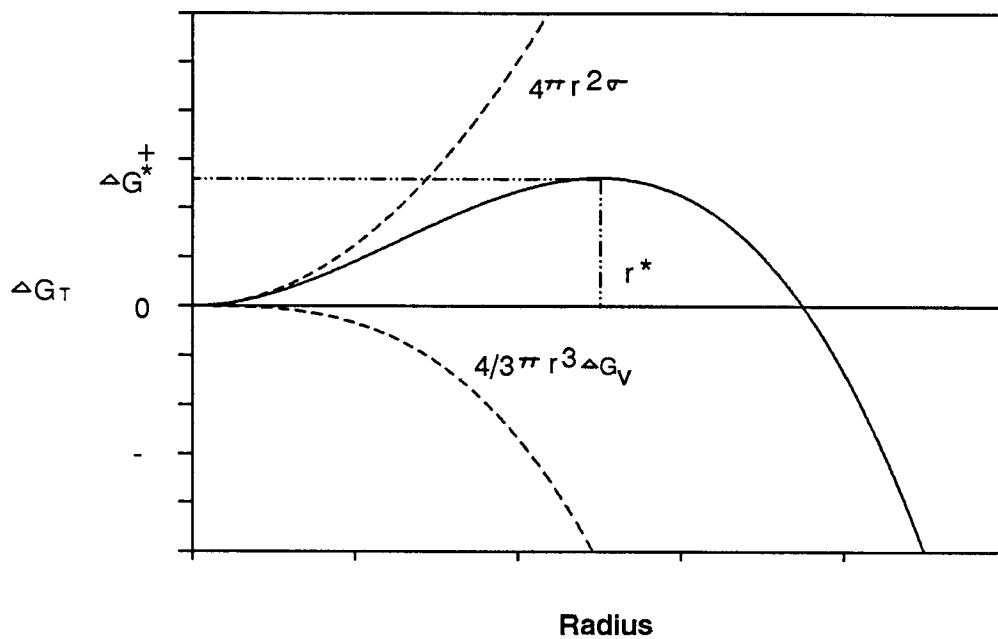


Figure 2.8. Free energy as a function of radius for a cluster contributions from surface and volume energy.

Kinetic Aspects

From our everyday experience we are prone to think of condensation as occurring at a sharply defined saturation threshold ($S_r = p / p_{\text{vap}} = 1$). Because of the statistical nature of molecular bombardment, however, it is intuitive that there should be moments when molecular aggregation of only a few molecules could occur though the lifetime of such a cluster is very short. It is even reasonable to assume that large clusters of molecules can exist for even shorter periods of time; in fact, a continuous distribution of so-called "polymers" should exist in the static state condition. Thus, the transient existence of two, three, or four molecular clusters termed dimers, trimers, and tetramers, and successively larger "g-mers" seems like a reasonable postulate on which to base the theory of homogeneous condensation.

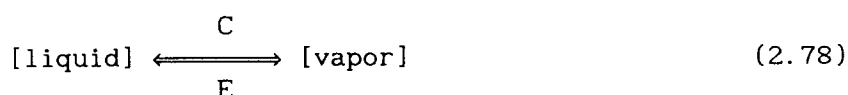
In general consequence of the law of mass action, increased concentrations of reactants enhance the forward transformation process. Thus one hopes to describe the rate of reaction in terms of concentration of subcritical droplets to supercritical droplets in the formation of clusters. In such a process there is a statistical steady-state population of clusters given by a Boltzmann-like distribution function

$$n_g = n_1 \exp \left(- \frac{\Delta G_g}{kT} \right) \quad (2.77)$$

where n_g is the number of clusters of size g molecules existing within

the distribution, and n_1 is the number of single molecules in the system. ΔG_g is the total free energy difference between the clusters in the condensed state and the host gaseous phase.

The process of condensation and evaporation can be described in the following form:



consisting of condensation (C) balanced by evaporation (E). For classical theory involving the bombardment of molecules onto a small cluster of radius r , the condensation rate is given by

$$C = \frac{4 \pi r^2 q p}{(2 \pi m k T)^{1/2}} \quad (2.79)$$

where m is the mass of one vapor molecule, p is the prevailing vapor pressure and q is the fraction of impinging molecules that remain on the cluster (accommodation factor or "sticking" coefficient. McDonald²³ gave a derivation of the kinetic expression for the condensation process in which he assumed that the evaporation rate is not a function of vapor pressure but only of radius and temperature. The evaporation rate E for a given cluster is equivalent to the rate of condensation at a vapor pressure that would exist if the given cluster radius would represent a critical radius. McDonald suggested further that the current J_g results from a product of C or E and n_g where n_g is the concentration of clusters of g size in the system.

Based on this idea the kinetic expression for the flux of critical-sized clusters is obtained as

$$J = \left(\frac{p}{kT} \right)^2 \frac{1}{\rho_L} \left(\frac{2\sigma}{\pi N_A} \right)^{1/2} \exp \left(- \frac{4\pi\sigma r^{*2}}{3kT} \right) \quad (2.80)$$

Here k is the Boltzmann constant, N the Avogadro number, ρ the density of the vapor, σ the surface tension of the liquid, and r^* is the critical drop radius.

Condensation in Free Jet Expansion

The analysis of condensation of gases in a jet expansion can be done based on the following assumptions: (1) the flow is steady, and the nozzle wall is frictionless and non-heat conducting; (2) the vapor is a perfect gas with known thermodynamic constants; (3) the flow is isentropic before the onset of condensation, and diabatic thereafter; (4) the interaction between the condensed phase and flow is negligible; (5) the volume of the condensed phase is negligible compared with the total volume. With these assumptions, the flow equations can be written as:²⁴

$$\frac{d\rho}{\rho} + \frac{du}{u} + \frac{dA}{A} = 0 \quad (2.81)$$

$$\frac{d\rho}{\rho} + u \, du = 0 \quad (2.82)$$

$$\frac{dp}{p} = \frac{d\rho}{\rho} + \frac{dT}{T} - \frac{dg}{1-g} \quad (2.83)$$

$$(\gamma-1)M^2 \left(\frac{du}{u} \right) + \frac{dT}{T} - \left(\frac{L}{C_p T} \right) dg = 0 \quad (2.84)$$

where p , T , u , A and ρ are flow quantities; L is the latent heat of evaporation; and g is the mass fraction in the condensed phase.

By using the above equations and with a framework of thermodynamics as well as nucleation theory Wang²⁴ obtained the growth rate of a droplet as

$$\Delta r_i = \frac{q}{L} \frac{p}{\rho_L} \left(\frac{2}{\pi} \right)^{1/2} \left(\frac{kN_A}{\mu T} \right)^{1/2} (T_s - T) \frac{\Delta X_i}{u} \quad (2.85)$$

where q is an accommodation factor and T_s is the temperature of the liquid.

By assuming the growth of droplets formed in all the previous steps and the new droplets formed, the net mass fraction condensed in a step increment ΔX_i can be obtained as

$$\Delta g_j = \frac{4\pi\rho_L}{m} \left[\sum_{i=1}^{j-1} N_i r_{ij}^2 \Delta r_j + \frac{1}{3} N_j r_j^{*3} \right] \quad (2.86)$$

here j is the index for the sample points under consideration, i the running index covering all previous sample points where nuclei were formed.

While the above expressions contain many assumptions, in principle, they can be used to model the condensation region of the N_2 expansions we discuss in chapter 5. Due to various reasons, modelling

of this early portion of the expansion was not completed as part of this thesis work but the brief discussion above is included as a stimulus to future extension of this work.

CHAPTER 3 DEVELOPMENT OF A BACKGROUND REDUCTION TECHNIQUE FOR
LOW FREQUENCY CARS AND A MULTIMODE REJECTOR FOR A
SEEDED Nd:YAG LASER

INTRODUCTION

Coherent anti-Stokes Raman spectroscopy (CARS) is an extremely powerful technique. Numerous applications now have been performed, such as combustion diagnostics,²⁵⁻²⁸ for which it was originally developed,²⁹ and the measurement of rovibrational excitations of molecules in plasmas³⁰ or in photochemistry experiments.³¹⁻³³ Most of this work has involved the study of vibrational transitions of 500 cm^{-1} or more. Extension to lower frequencies is desirable for the study of pure rotations of most molecules as well as of the low frequency modes of heavier molecules. Since the pure rotational spectrum of most molecules lies within 100 cm^{-1} of zero shift, one can readily scan this frequency range with a single dye and thus eliminate the need for multiple dyes necessary to span the vibrational region. This restricted frequency range, coupled with narrower, more widely spaced rotational lines allows for the possible detection of any number of simple molecules simultaneously. This feature of widely spaced, narrow lines also makes it possible to extract ground state rotational constants directly and hence to deduce molecular geometries. An additional advantage of pure rotational spectra is that they are easily fit to calculated spectra to give a direct measurement of sample temperature. Thus pure rotational CARS is useful for

determining number density, temperature, and structure of a wide variety of molecules with a single experimental setup.

Of particular interest to us is the development of low frequency CARS as a probe of free jet expansions. Such expansions are advantageous in that the rotational cooling that occurs during the expansion greatly increases the CARS signal intensity. By cooling a sample from room temperature down to 50 K or lower, pure rotational CARS signal intensities can be increased by several orders of magnitude, which greatly improves the detection limit of the spectrometer. For molecules with a complicated rotational spectrum, the cooling can simplify the spectral analysis and increase the effective resolution since Doppler and collisional linewidths are greatly reduced.

Figure 3.1 shows a schematic of the CARS spectrometer at Oregon State University. In brief, it consists of a single-mode injection seeded Nd:YAG laser which produce a 532 nm pump beam as ω_1 and a 355 nm beam to pump a PDL dye laser. The output of the dye laser is used as ω_2 . The CARS spectrum is recorded by scanning ω_2 . A folded BOXCARS arrangement³⁴⁻³⁵ is used in the low frequency CARS experiment in order to eliminate the background scattering. A single pass monochromator is used to detect the CARS signal. A local computer program and a personal computer are used with a master A/D board to scan the dye laser and monochromator and to digitize the signal.

The primary problem in obtaining low frequency CARS spectra is the separation of the very intense pump beam ω_1 and Stokes beams ω_2

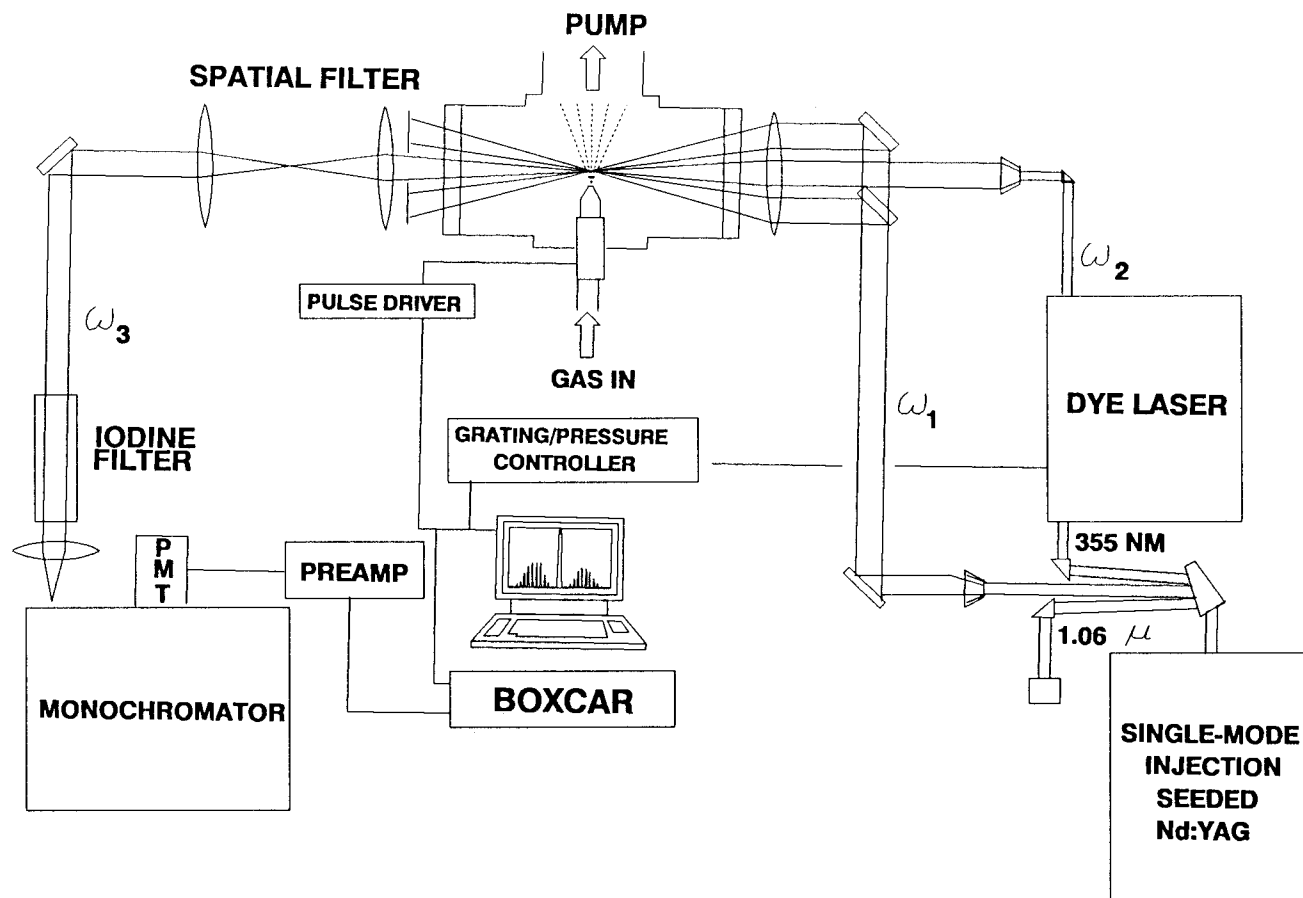


Figure 3.1. Schematic of CARS spectrometer.

from the much weaker CARS beam ω_3 since the frequencies of all are nearly degenerate for small shifts. The first report of low frequency CARS was by Beattie who recorded the pure rotational spectrum of air down to about 40 cm^{-1} . He utilized a four color, collinear phase matching scheme with two dye lasers and one fixed frequency laser to produce the CARS beam frequency shifted away from the tunable sources. Separation of the CARS signal from the input beams was achieved by use of prisms, gratings and a polarization analyzer. It was apparent from Beattie's work that optical separation of the CARS signal beam from the input beams was not possible at very low shifts.

Subsequently, a phase-matching technique, folded BOXCARS, was developed by Eckbreth,³⁴ as shown in Figure 3.2, to spatially separate the signal beam from the input beams. This technique works well down to about $\pm 10 \text{ cm}^{-1}$ shift. However, as seen in the pure rotational spectrum of N_2 shown in Figure 3.3, the background scattering is still quite strong for smaller shifts from zero. For most heavier molecules, the pure rotational spectrum is seen within a few wavenumbers shift, as illustrated, for example, by a calculated pure rotational spectrum of HgCl_2 shown in Figure 3.4. Our interest in studying such species led us to seek ways to eliminate all the scattering even down to the zero shift. As described below, a effective method has been found which works with a single mode pump laser source.

The Q-switched Nd:YAG laser is the most important element in our CARS apparatus. We utilize an injection seeded Nd:YAG laser which

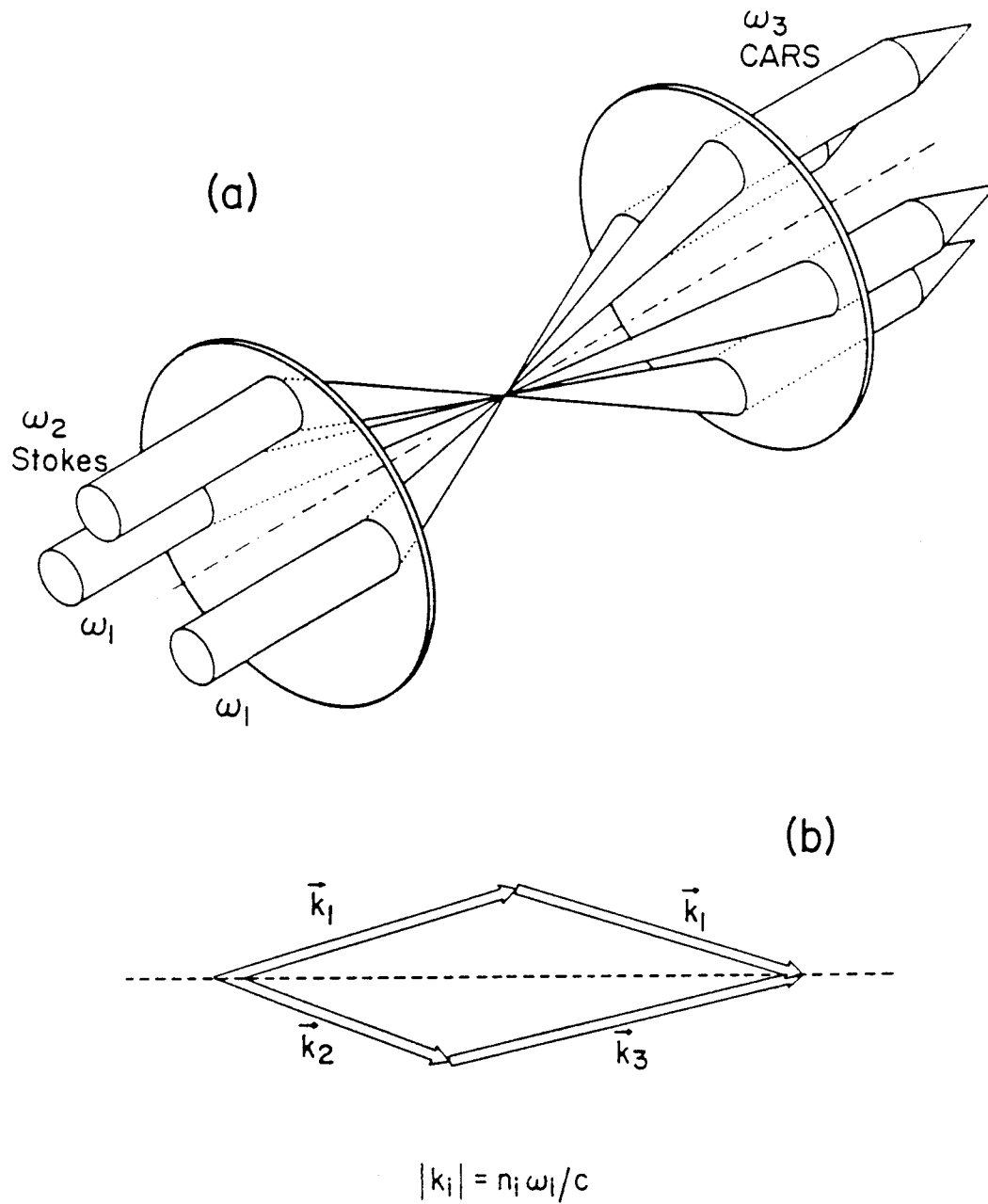


Figure 3.2. Three dimensional phase matching in the CARS experiment. (a) gives physical orientation of input and CARS beams, (b) is the vector condition necessary to achieve $\Delta k = 0$.

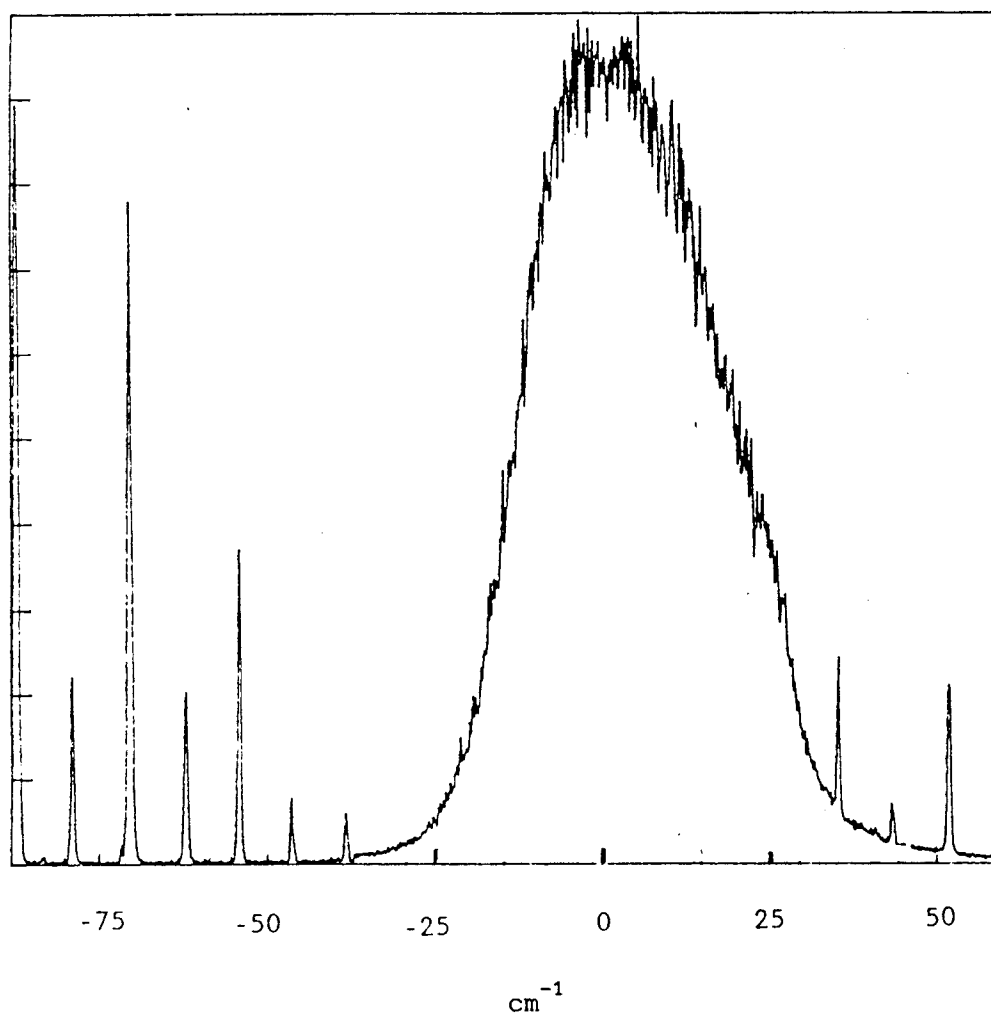


Figure 3.3. CARS Pure rotational spectrum of N_2 .

Pure Rotational Raman Intensities

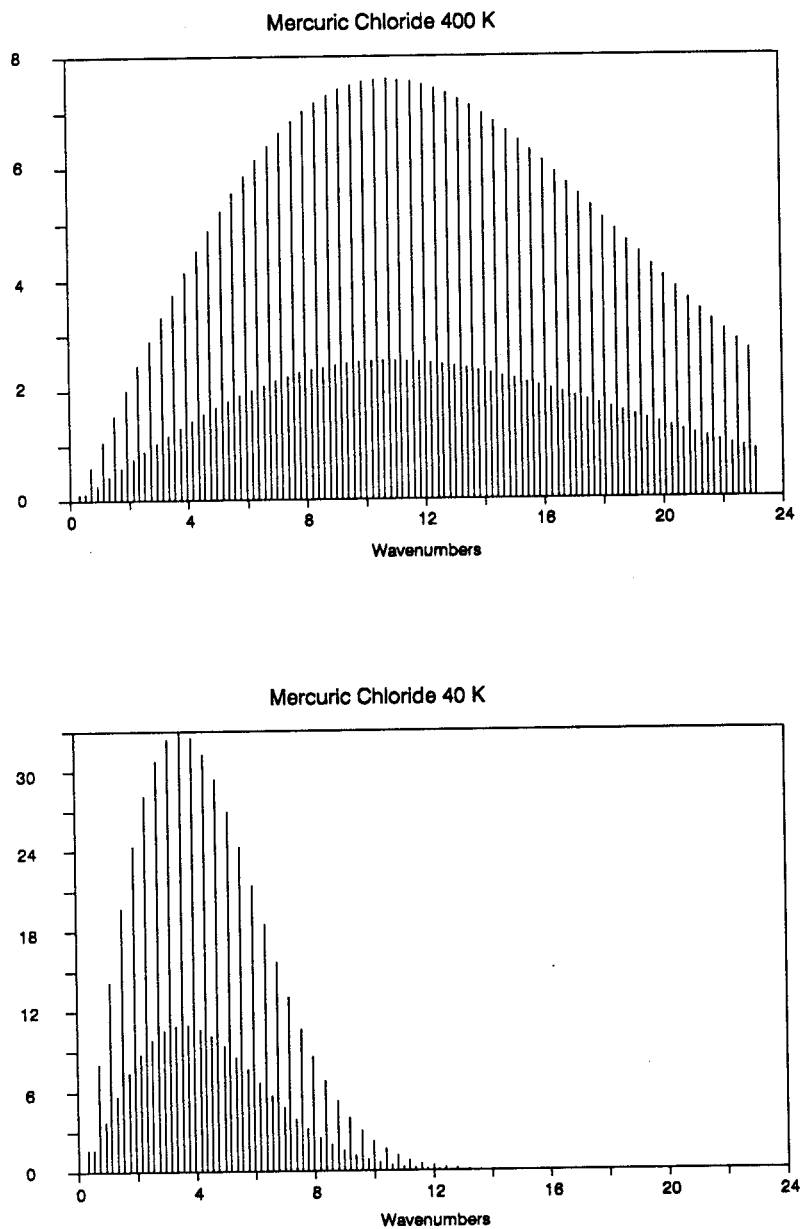


Figure 3.4. Calculated pure rotational spectra of mercuric chloride at 400 K and 40 K.

includes a diode laser-pumped injection source based on the MISER design of Byer.³⁸⁻⁴² This master laser is a true single mode source but unfortunately the injected slave laser is less perfect and mode hops and multimode output ("bad shots") occur 5 to 10% of the time. In addition, a burst of multimode pulses occurs when the adjustment range of the piezo drive for the slave cavity length is exceeded and a reset operation takes place. These "bad shots" are particularly troublesome in our CARS experiment since they not only degrade the spectral purity of the source but also produce significant amplitude fluctuations. In this chapter, I will present a new background reduction technique for low frequency CARS. As part of this technique a new INVENTION of a multimode laser shots rejector for the seeded Nd:YAG laser was developed. Experimental results show that the device works very well for rejecting all such bad laser shots, significantly improving the signal to noise ratio in our experiments.

In order to build up a background for the material which we will present in this chapter, a review on the basic theory of laser and seeding laser operation will be given first.

BASIC LASER THEORY

Two-level Laser System

We now consider a two level system shown in Fig.3.5(a) as enclosed in the optical resonator shown in Fig 3.5(b). The two levels have energies E_1 and E_2 , and degeneracies g_1 and g_2 respectively, and

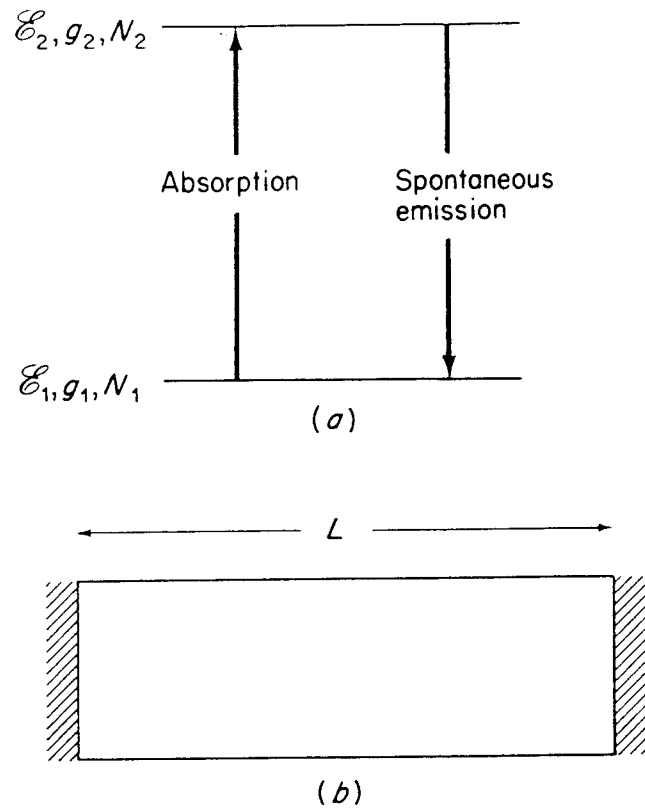


Figure 3.5. (a) A two-level system. (b) Laser resonator containing the two-level atoms.

the system contains N_1 atoms in level 1 and N_2 in level 2. The two ends of the optical resonator are two plane mirrors parallel to each other and separated by the distance L .

The N_1 atoms in the lower level absorb photons of energy $h\nu_0$ at the rate.

$$R_{\text{abs}} = B_{12} N_1 u(\nu_0) \quad (3.1)$$

where B_{12} is the Einstein coefficient for absorption and $u(\nu_0)$ is the energy density in the frequency interval of width $d\nu$, centered at ν_0 . The N_2 atoms in the upper level are stimulated to emit photons at the rate

$$R_{\text{stim}} = B_{21} N_2 u(\nu_0) \quad (3.2)$$

where B_{21} is the Einstein coefficient for stimulated emission. The N_2 atoms also decay spontaneously at the rate

$$R_{\text{spont}} = A_{21} N_2 = \tau_2^{-1} N_2 \quad (3.3)$$

where A_{21} is the Einstein coefficient for spontaneous decay and τ_2 is the lifetime of the upper level. The Einstein coefficients for stimulated emission and absorption are

$$B_{21} = \frac{c^3}{8\pi h \nu_0^3 \tau_2} \quad (3.4)$$

$$B_{12} = \frac{g_2}{g_1} B_{21} \quad (3.5)$$

When the line shape is dominated by Doppler broadening, it is represented by the function $g(\nu - \nu_0)$ as shown in Figure 3.6(a), where the area under the line is normalized to unity,

$$\int g(\nu - \nu_0) d\nu = 1 \quad (3.6)$$

For the specific frequency ν the Equation (3.4) becomes

$$B_{21}(\nu) = \frac{c^3 g(\nu - \nu_0)}{8\pi h \nu_0^3 \tau_2} \quad (3.7)$$

Intensity Amplification

Now we assume that there is a monochromatic beam of frequency ν travelling along the axis of the optical resonator with an intensity

$$I(x) = cu(\nu, x) \quad (3.8)$$

where $u(\nu, x)$ is the energy density in the frequency ν on the x axis. If the density of atoms in the lower level is n_1 , the number of photons absorbed in one second within a slab of depth dx and unit area is $B_{12}(\nu)n_1 dx u(\nu, x)$. Each absorption leads to the removal of an

energy amount $h\nu$ from the beam, and so

$$dI = - h\nu B_{12}(\nu) n_1 dx \quad u(\nu, x) = - I(z) \frac{h\nu B_{12}(\nu) n_1}{c} dx \quad (3.9)$$

If absorption were the only process occurring within the beam, the beam intensity would be given by

$$I(x) = I(0) e^{-\mu x} \quad (3.10)$$

where the absorption coefficient is

$$\mu = \frac{h\nu B_{12}(\nu) n_1}{c} = \frac{g_2 c^2 g(\nu - \nu_0) n_1}{g_1 8\pi \nu_0^2 \tau_2} \quad (3.11)$$

On the other hand, the presence of atoms in the upper state causes photons to be added to the beam by stimulated emission, giving an effective 'anti-absorption' or intensity amplification. The absorption coefficient, now better described as the attenuation coefficient, is

$$\mu = \frac{h\nu}{c} (B_{12} n_1 - B_{21} n_2) = \frac{c^2 g(\nu - \nu_0)}{8\pi \nu_0^2 \tau_2} \left(\frac{g_2}{g_1} n_1 - n_2 \right) \quad (3.12)$$

This can be positive or negative, depending on the relative magnitudes of $g_2 n_1 / g_1$ and n_2 .

For a system in thermal equilibrium, the attenuation coefficient is always positive, and the intensity decreases with distance. This

follows because for each atomic level the population of each of its sub-levels is proportional to the Boltzmann factor. Therefore

$$n_{1,2} \propto g_{1,2} e^{-E_{12}/kT} \quad (3.13)$$

and

$$\frac{g_2}{g_1} n_1 - n_2 = n_2 (e^{(E_2-E_1)/kT} - 1) = n_2 (e^{h\nu/kT} - 1) > 0 \quad (3.14)$$

Thus the $\mu > 0$.

Population Inversion

The attenuation coefficient can be made negative by setting up a nonequilibrium system in which the condition

$$\Delta n = n_2 - \frac{g_2}{g_1} n_1 > 0 \quad (3.15)$$

is satisfied. This population inversion can be created by a suitable pumping mechanism.

Figure 3.6(b) shows a system in which a population inversion exists between the levels 2 and 3 and also between the levels 5 and 6. When a population inversion exists the beam intensity increases with distance,

$$I(x) = I(0) e^{kx} \quad (3.16)$$

where the gain coefficient k is

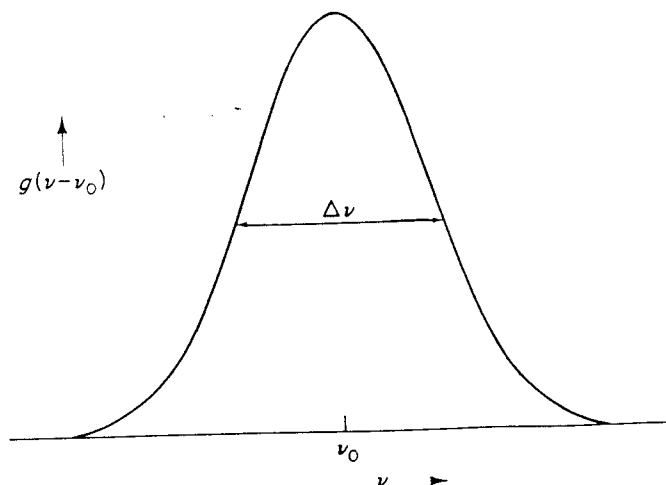


Figure 3.6(a). Shape of the absorption or emission line.

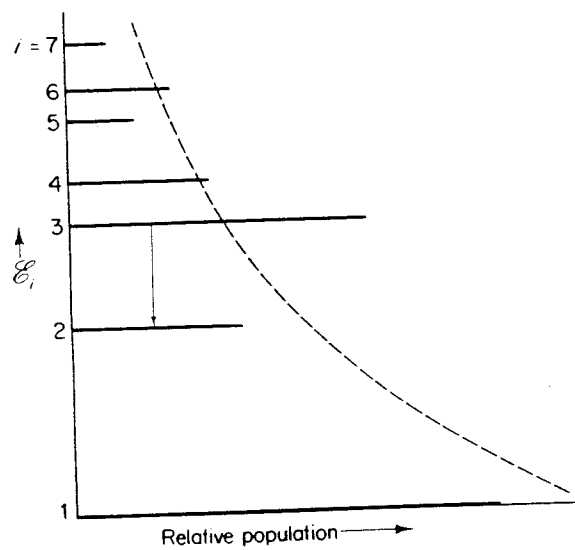


Figure 3.6(b). Relative populations level of a laser medium.

$$k = -\mu = \frac{c^2 g(\nu - \nu_0)}{8\pi\nu^2 \tau_2} \Delta n \quad (3.17)$$

In traversing the length L of the laser the intensity therefore increases by the factor

$$\left(\frac{I(L)}{I(0)} \right) = e^{kL} \quad (3.18)$$

Loss Processes

Apart from absorption and stimulated emission there are various other processes which cause changes in the intensity of the beam, all of them resulting in a loss of intensity. The most important of these occurs in the laser in which the beam must be reflected many times between the two end mirrors in order to obtain a significant intensity gain. If the successively reflected waves are in phase with each other there is no loss in the intensity when they interfere, but if they are out of phase they interfere destructively, eventually canceling each other out after many reflections. As in the Fabry-Perot interferometer, the intensity loss due to destructive interference in the laser cavity is zero only under the condition

$$2L = n\lambda \quad (3.19)$$

where n is an integer. With this condition the electromagnetic field oscillates as a standing wave of frequency

$$\nu_n = n \frac{c}{2L} \quad (3.20)$$

This mode of oscillation is a normal mode of the cavity. The mode number n is usually very large; for example in our Nd:YAG laser, the cavity length is 0.6m and the wavelength is 1064 nm, so n is 1.1278×10^6 . The frequency spacing of these modes is

$$\Delta\nu = \frac{c}{2L} \quad (3.21)$$

Other sources of loss comes from the non-unity reflection coefficients R_1 and R_2 of the end mirrors, diffraction effects, and scattering in the laser medium. The losses can be characterized by the Q-value of the cavity, defined by

$$Q = 2\pi \frac{\text{energy stored}}{\text{energy lost per period of oscillation}} \\ = \frac{2\pi I}{\left(-\frac{dI}{dt} \bigg/ \nu\right)} = 2\pi\nu t_c \quad (3.22)$$

where t_c is the decay time of cavity. This value is about 10^8 to 10^9 for visible lasers.

Threshold condition

Figure 3.7 shows the magnitudes of the gains and losses for a laser, as a function of frequency, for a narrow range of frequency covering an absorption line. The absorption and stimulated emission processes give an average intensity gain per pass of

$$G_1 = e^{kL} \quad (3.23)$$

Assuming that a population inversion exists in the cavity, $k > 0$ and $G_1 \geq 1$. On the other hand the loss processes give an effective gain G_2 which is always less than 1. Its maximum value is

$$G_2^{\max} = e^{-L/(ct_c)} \quad (3.24)$$

which occurs when condition (3.19) is met.

The lower part of the figure shows the product $G_1 G_2$ in the case where $G_1 G_2 > 1$ at two different normal mode frequencies. The laser is therefore able to oscillate at these frequencies, with a continuous build-up of intensity. The other modes, shown as broken lines, are suppressed.

A necessary condition for the laser to be able to operate on at least one normal mode is that

$$k_{\nu_0} - \frac{1}{ct_c} > 0 \quad (3.25)$$

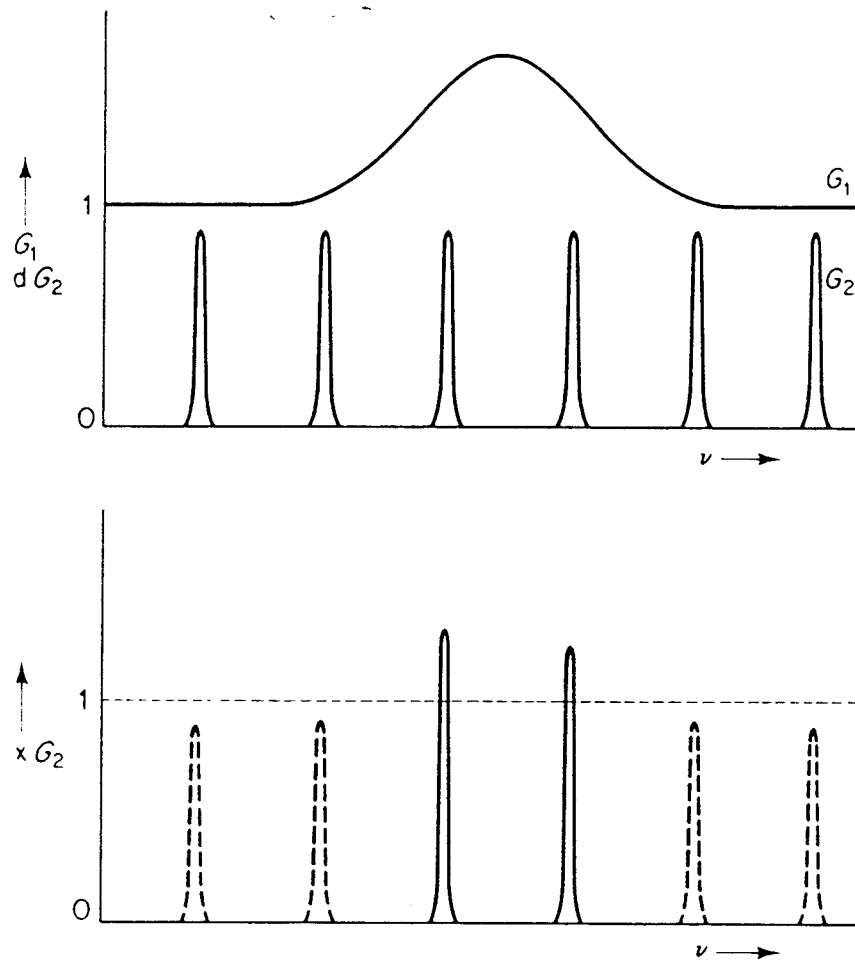


Figure 3.7. G_1 is the average gain per pass due to the combined effect of absorption and stimulated emission. $G \geq 1$ when a population inversion exists. G_2 is the gain per pass due to the various loss processes. The laser can oscillate only when $G_1 G_2 > 1$.

This is known as the threshold condition for the laser.

The threshold condition is a necessary condition to be satisfied before a laser beam can be produced, but at the same time the following conditions have also to be satisfied. One is that the beam to be amplified must originate at some time. Usually this happens by the spontaneous emission of an excited atom, producing a single photon. The other one is that this initial photon should travel in a direction parallel to the axis of the laser. Then the beam can be reflected several times, enabling the intensity to increase. Because spontaneous emission is an isotropic process there are always some photons emitted in the required direction.

Q-Switched Laser

A technique for producing a single high-energy pulse, instead of a continuous train of pulses, is that of *Q-switching*. The 'Q' refers to the Q-value of the laser cavity. In a *Q-switched* laser, the laser is keeping the Q-value low while the population inversion is created, and increasing it suddenly to allow stimulated emission to build up quickly by multiple reflections in the cavity. This results in the cavity energy being released in a short intense pulse.

INJECTION SEEDING THEORY

Injection seeding refers to the process of achieving single mode operation of a pulsed laser by injecting radiation from a very narrow linewidth laser into the pulsed laser cavity during the time of the opening of the Q-switch.

When the injecting radiation frequency is within the bandwidth of a pulsed laser cavity mode a Q-switched pulse will develop more rapidly out of this "seed" emission than out of background spontaneous noise emission. Consequently, the pulse developing out of the seed signal will saturate the gain medium and extract the energy before a pulse which is coincidentally trying to grow out of noise emission is able to do so. This inhibits further amplification and growth of any pulse developing out of noise emission. In this way all of the energy stored in a homogeneously broadened gain element such as a Nd:YAG laser rod is depleted by the pulse which developed out of the seed laser emission, resulting in single frequency output from the pulsed laser.

Longitudinal Modes of Pulsed Laser

As we described in the preceding section the Q-switched Nd:YAG laser with the cavity length of 0.6 m at frequency 1064 nm can have about 1.13×10^6 modes. The spacing of these modes can be calculated by using Equation (3.21) which gives

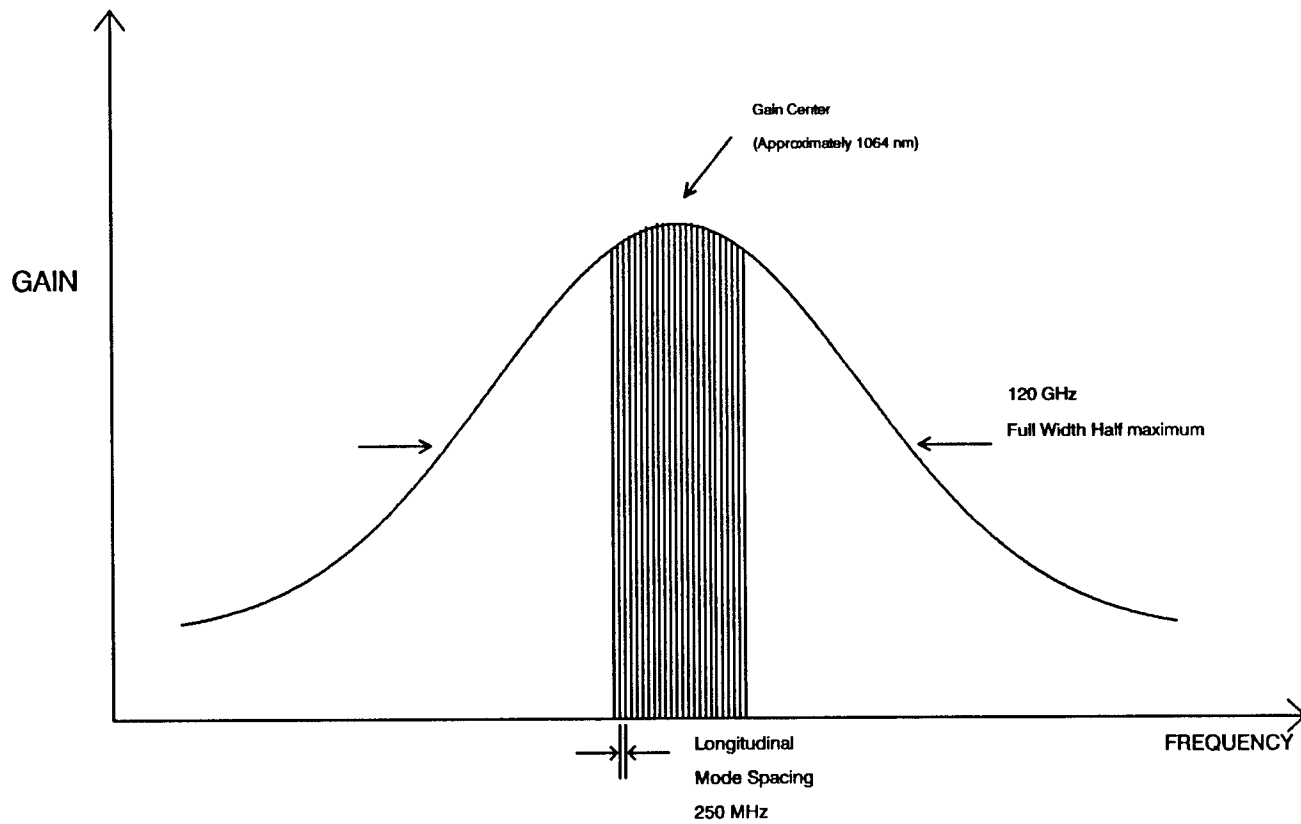


Figure 3.8. Longitudinal modes of the host laser.

$$\begin{aligned}\Delta\nu &= 3 \times 10^{10}(\text{cm/sec}^2) / 2 \times 1 \times 60 \text{ (cm)} \\ &= 250 \text{ MHz}\end{aligned}$$

The gain curve for Nd:YAG is approximately 120 GHz (or 4 cm^{-1}) FWHM which means that Nd:YAG can support a large number of longitudinal modes. However due to mode competition, longitudinal modes closest in frequency to the center of the gain curve capture most of the available energy at the expense of longitudinal modes further from gain center. This generally results in a normal unseeded line width of about 1 cm^{-1} for the pulsed laser.⁴⁵ This is illustrated in Fig. 3.8.

Laser resonators have transverse ("spatial") modes in addition to longitudinal modes. Transverse modes, like longitudinal modes, also have characteristic frequencies associated with them. It is imperative, for injection seeding purposes, that the pulsed Nd:YAG laser run in a single transverse mode (the lowest order transverse mode). Furthermore the resonator should have strong discrimination against the lasing of any higher order transverse modes.

Q-Switch Buildup Time: Unseeded Operation

The Q-Switch is included in the host resonator to initially prohibit lasing during flash lamp emission for a time period on the order of 250 μsec - the upper state lifetime of Nd:YAG. This ensures that the Nd:YAG rod in the host oscillator has stored as much energy as possible. At full power this stored energy level can translate into

a single pass gain in excess of 50.

After this energy storage time is complete the Q-Switch is opened. This allows any light in the cavity possessing the proper frequency characteristics (i.e. frequency within the gain bandwidth of Nd:YAG and resonant with a longitudinal mode of the host cavity) and spatial characteristics (i.e. "on axis") of the host resonator to be amplified by the Nd:YAG gain media. In the unseeded host laser this initial light within the cavity is in fact broad band spontaneous noise emission from the Nd:YAG oscillator and amplifier rods. The spectral features of this noise emission are given by the fluorescence gain curve of Nd:YAG shown in Fig. 3.9. This relatively weak spontaneous noise emission radiates in all direction leaving only a very small power level (\leq nanowatts) sufficiently on axis to experience resonant amplification.

Consequently, as the Q-Switch is opened this low level spontaneous emission must make a sufficient number of round trips through the Nd:YAG gain media to reach a fluence level comparable to the characteristic saturation intensity for Nd:YAG. With a small signal gain of ≥ 50 per pass, and accounting for output coupling losses, this typically requires about 12 resonator round trips. Given the speed of light and a resonator round trip length of 1.2 meters, 12 round trips can be seen to correspond to approximately 45 nsec.

When the amplified spontaneous emission reaches the saturation fluence, significant energy is extracted from the Nd:YAG rod that the large signal gain value is lowered to of approximately 2.5 - 4 per

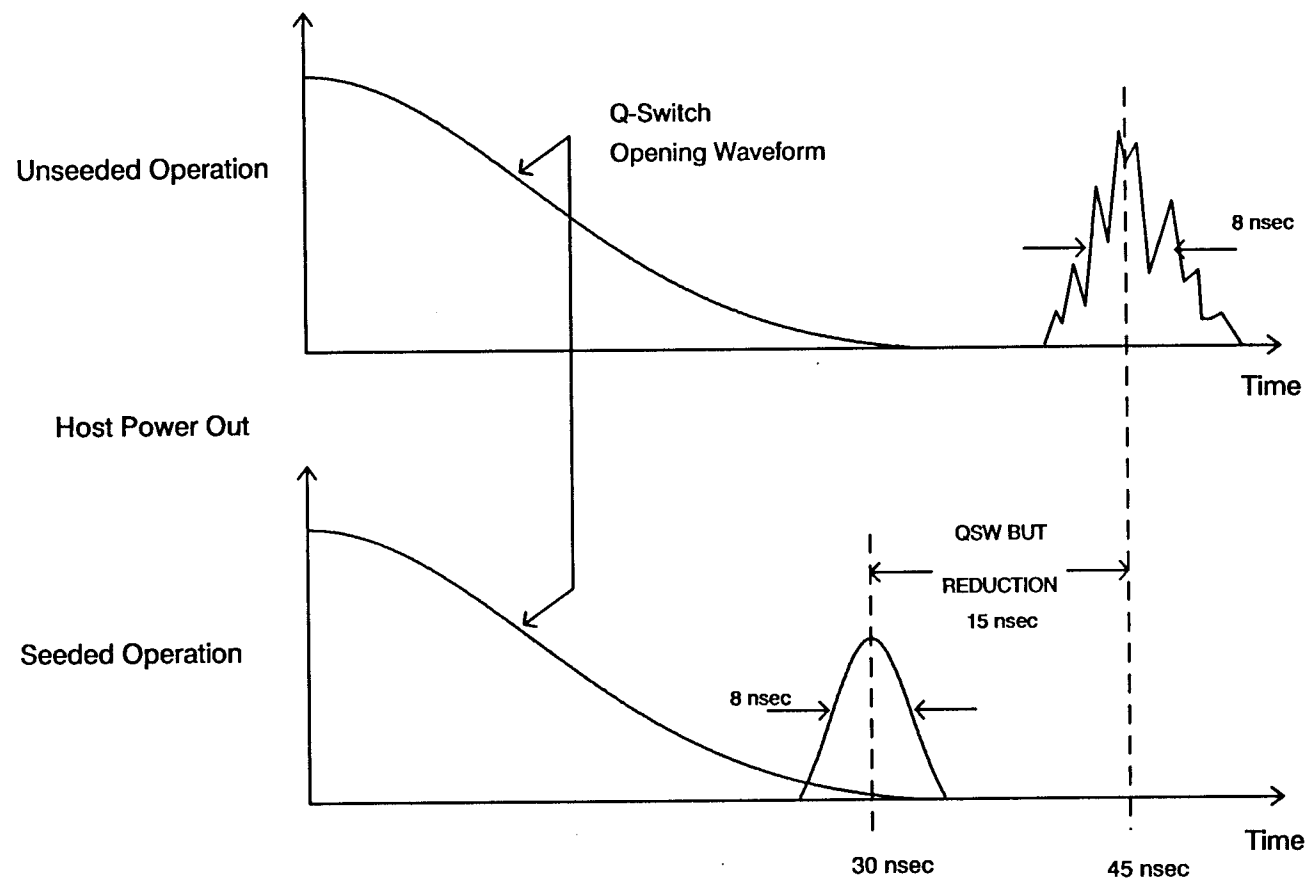


Figure 3.9. Q-switch buildup time reduction.

pass. At this time a pulse can begin to be observed being emitted from the host laser. The observed output pulse width corresponds to the number of round trips required for circulating photons to extract all the energy stored in the Nd:YAG oscillator rod. The time during which the spontaneous noise emission is amplified up to the saturation fluence level is termed the " Q-Switch Pulse Buildup Time ".

Q-Switch Buildup Time: Seeded Operation

During seeded operation very narrow linewidth ($\Delta\nu < 10 \text{ KHz}$) laser emission of > 1 milliwatt is directed into the host laser cavity on axis. When this "seed" emission is within the bandwidth of a longitudinal mode of the host laser it is resonantly amplified by the Nd:YAG rod when the Q-Switch is opened. The seed emission is greater than 6 orders of magnitude stronger than the spontaneous noise emission ($< \text{nanowatts}$). It is clear that a Q-Switched pulse will build up sooner out of the seed emission than it could out of spontaneous emission.

Furthermore, when the amplified seed emission reaches the saturation intensity level the gain in the oscillator rod is quickly reduced from the small signal level (> 50) to the large signal level (2.5-4). This reduction in gain inhibits further amplification of spontaneous emission keeping it at a low level relative to the seeded output pulse. The difference in time between when a Q-Switch pulse is emitted in seeded operation versus unseeded operation is termed the reduction in Q-Switch buildup time.

Injection Seeder

Figure 3.10 shows an injection seeder and each component will be discussed briefly as follows

(1) *C.W. 1.06 μ Seed Laser Source:*

The seed laser employed in the seeder is a monolithic, laser diode pumped, unidirectional ring resonator termed the MISER (Monolithic Isolated End pumped Ring). The essential features of the MISER are the incorporation within a monolithic structure of an effective half wave plate polarization rotator, Faraday rotator and polarizer. The combined effect of these three optical elements is to yield lower losses for a complete transit of the ring resonator for lasing in one direction than for the other. This forces the ring resonator to lase in one direction only. The ring resonator is then a travelling wave resonator in contrast to a standing wave resonator described previously. Because it is a travelling wave resonator the MISER does not suffer from the effects of spatial hole burning and consequently will only lase in a single longitudinal mode.

The geometry of the MISER is shown in Figure 3.11 Polarization selection takes place at the curved, partially transmitting face (point A). At points B, C, and D total internal reflection occurs. A magnetic field H is applied to establish unidirectional oscillation. Faraday rotation takes place along segments AB and DA. The focused pump laser beam enters the crystal at point A, and the output beam emerges at the same point.

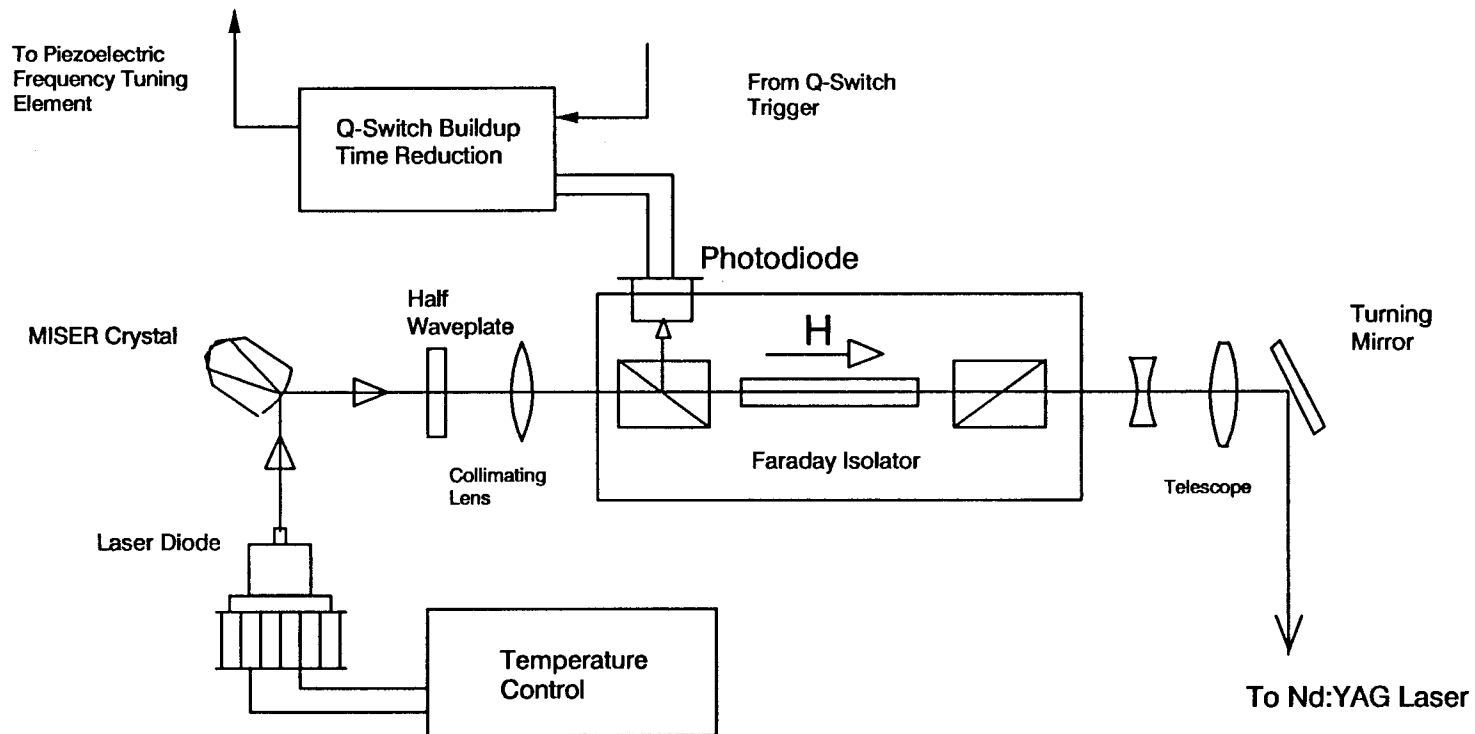


Figure 3.10. Injection seeder block diagram.

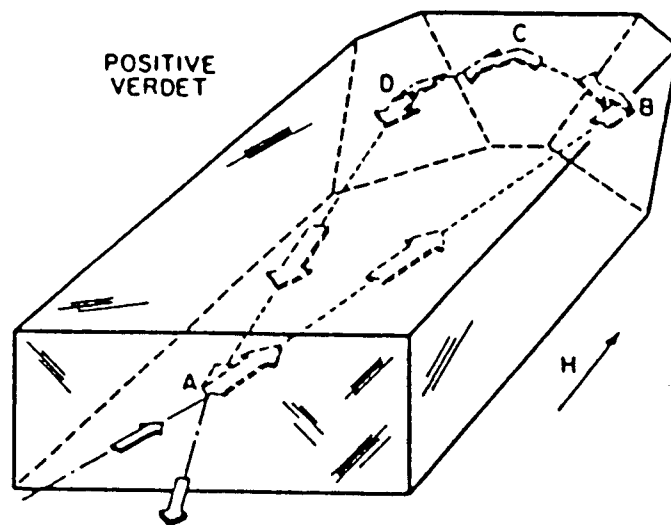


Figure 3.11. Monolithic isolated end pumped ring (MISER).

(2) *Collimating Lens And Half Wave Plate Assembly.*

The collimating lens is used to ensure that a small diameter, well collimated beam is transmitted through the Faraday Isolator for maximum throughput and isolation. The half wave plate matches the MISER output polarization to that of the Faraday Isolator.

(3) *Faraday Isolator.*

The Faraday Isolator, an optic diode, is included in the injection seeder for two essential reasons:

- i) to prevent any backward propagating radiation from the host laser from destroying the seed laser.
- ii) to decouple the seed laser resonator from the host resonator to preserve the frequency stability of the seed laser.

(4) *Telescope Assembly.*

Incorporation of a beam expanding telescope in the injection seeder helps to optimize the spatial mode matching between the seeder and the host. Spatial mode matching lengthens the lifetime of seed laser photons within the host resonator, increasing the seed laser power coupled into the host cavity. The telescope also provides a convenient adjustment to account for variable oscillator rod thermal lensing and mirror curvatures in the host laser.

(5) *Turning Mirror.*

The final optical element within the injection seeder is a turning mirror to turn the beam through an exit aperture at the bottom of the seeder. This mirror is adjustable and is included to maintain proper alignment of the seed laser beam with the host optical axis.

(6) *Q-Switch Buildup Time Reduction*

As discussed previously, the function of Q-switch buildup time reduction is to ensure optimal frequency overlap between the seed laser and the host laser.

(7) *Temperature control*

All temperature sensitive optical elements within the injection seeder are temperature controlled to ensure consistent performance with minimal operator adjustments.

Frequency Control of the Injection Seeder

The frequency of the Seed Laser output is temperature sensitive. By changing the temperature of the monolithic Seed Laser its output can be made to fall in the center of the host laser's gain curve. This position produces the most effective and stable seeding and also the highest seeded output power from the host laser.

Two temperature effects produce the movement of the Seeder output frequency. The first, expansion (or contraction) of the YAG crystal and the change in the YAG refractive index combine to produce a frequency shift $-3.1 \text{ GHz}/^{\circ}\text{C}$ in the Seeder resonator modes. The second, the movement of the YAG gain center causes a frequency shift of approximately $-1.4 \text{ GHz}/^{\circ}\text{C}$. These two effects combine to produce the frequency tuning curve shown in Figure 3.12. Approximately every 20 GHz the frequency "hops" back about 10 GHz. This is due to a new longitudinal mode moving to a position closer to the center of the gain curve. By temperature tuning, a range of about 2 cm^{-1} can be covered.

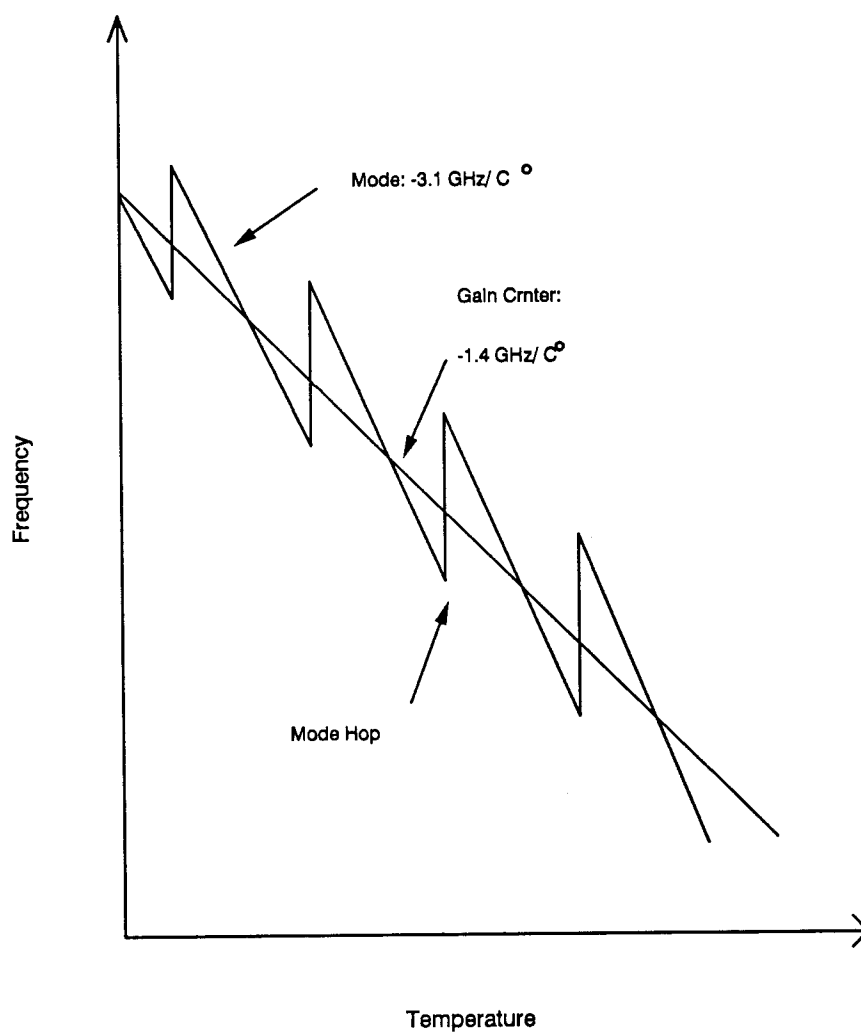


Figure 3.12. Frequency tuning of the injection seeder.

DEVELOPMENT OF A BACKGROUND REDUCTION TECHNIQUE

The basic ideal of the ω_1 background reduction technique is as follows, as we mentioned before the main concern for low frequency CARS experiments is the intense scattering of the ω_1 beam, which is difficult to filter from the weak near by ω_3 signal we wish to detect. Ideally, one would like a "spike" rejection filter at the ω_1 frequency but this is difficult to achieve with interference filters or monochromators. However, the vapor phase absorption spectrum of I_2 is very rich in the visible region. We make use of this by tuning the frequency of the doubled output of the seeded Nd:YAG laser ω_1 to one of the very sharp I_2 absorption peaks. An I_2 "spike" filter cell is then placed in front of the monochromator so that any scattering caused by ω_1 beam will be absorbed. Some details of our method of scanning the output of Nd:YAG laser to match an appropriate I_2 line are given in following sections.

Modification of Frequency Tuning for the Seeder

As discussed previously, the output frequency of a seeded Nd:YAG laser can be scanned about 2 cm^{-1} by temperature-tuning. The temperature coefficient of the MISER Nd:YAG laser is about $-0.15 \text{ cm}^{-1}/^\circ\text{C}$. Figure 3.13 shows the temperature control board of the

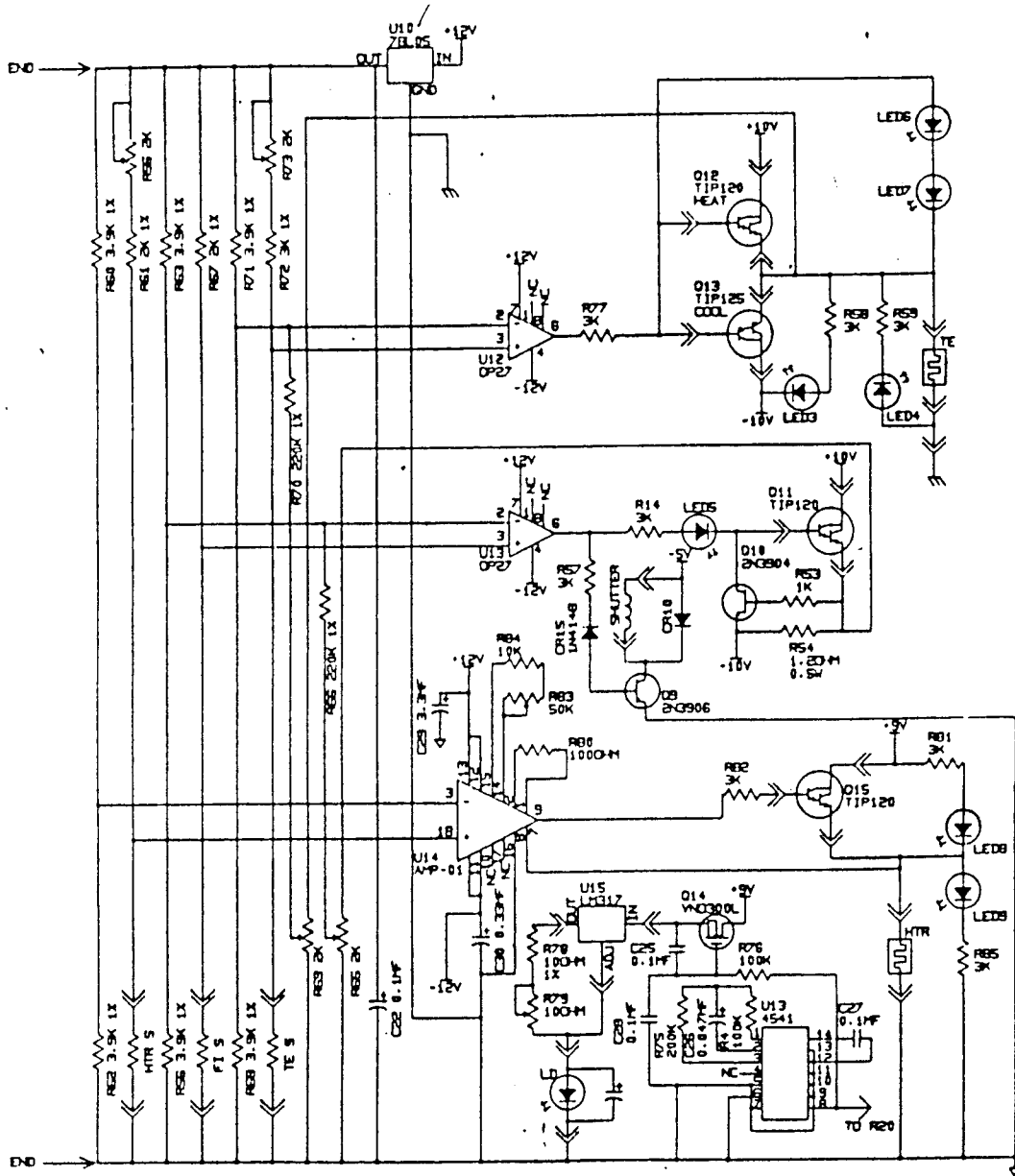


Figure 3.13. Temperature control circuit.

seeder. U14 amp-01 is a comparator which essentially controls the temperature of the MISER crystal. R60 and R62 are the two resistors for setting a reference temperature for the MISER crystal. HTR-5 is a thermistor which senses the temperature of the crystal. R61 and R56 are current limiting resistors which control the current passed through the thermistor. By adjusting the pot R56, one can change the temperature of the crystal. We have used this method to scan the laser 2 cm^{-1} for some experiment. However this is a tedious task manually since, with the time necessary for the temperature to stabilize, the scan required ~ 8 hours.

Figure 3.14 is the electronic circuit which I designed that can be inserted into the temperature control circuit in Figure 3.13 to let a computer scan the 2 cm^{-1} range. The way in which I modified the circuit is to disconnect R61 and R56 and connect the output of the modification circuit to R61. In this way we can vary the current passed through the thermistor by varying the voltage applied to it. The modified circuit basically is a reduced gain and an adder circuit which can reduce the step size of the scan. The D/A out of the computer is 10 V and the total number of bits is 4000. Therefore, 1 bit is about 2.5 mv. By using the modified circuit the smallest voltage interval is 0.625 mv. This small voltage increment is sufficient to ensure the temperature change of MISER Nd:YAG crystal is small. Therefore, the frequency of the output will be easy to stabilize. A computer program used for scanning the seeder is listed in appendix B.

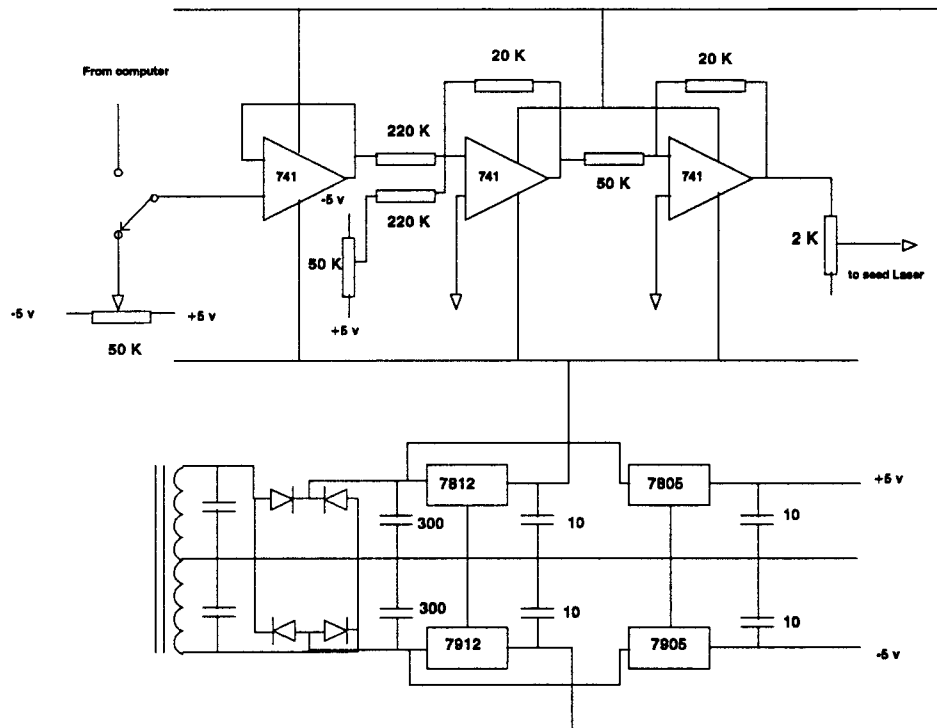


Figure 3.14. Temperature scan circuit.

I_2 Absorption Spectrum

The spectrum of iodine vapor is very rich in the visible region⁴⁹ and Figure 3.15 shows the absorption measured in the 532 nm region as the frequency of the seed laser was temperature-tuned. Displayed is the output of a photodiode used to monitor a small portion of the doubled output of the slave laser after passage through a 10 cm cell containing I_2 vapor in equilibrium with the solid at room temperature. Several hops between modes of the seed laser occurred as the temperature of the laser was scanned stepwise but it is apparent that several strong I_2 absorptions fall within the tuning range in which the slave laser output energy remains high. The vacuum wavenumber values and assignments given in Ref. 88,48 for the eight strong lines are

18786.66	R57	(32-0);	P166 (40-0)
18786.773	R54	(32-0)	
18787.134	P119	(35-0)	
18787.286	R86	(33-0)	
18787.344	R106	(34-0)	
18787.810	P83	(33-0);	R134 (36-0)
18788.343	R56	(32-0)	
19788.415	P53	(32-0);	P103 (34-0); P159 (39-0)

The Doppler width of each line is 0.013 cm^{-1} but hyperfine components broaden each transition to about 0.04 cm^{-1} .⁴⁸ Pressure

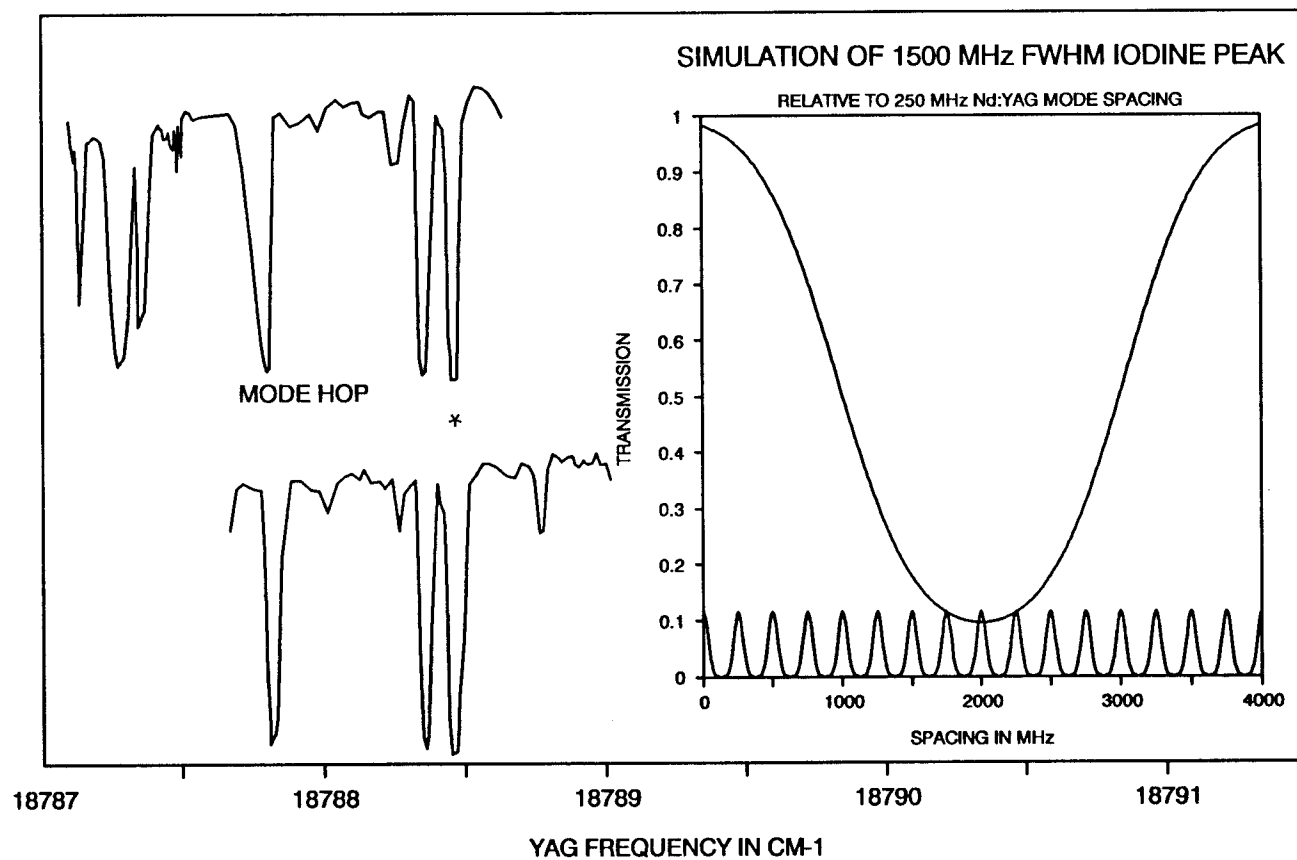


Figure 3.15. I_2 absorption spectrum within the seeder tuning range.

broadening is negligible in the absence of air leaks. The temperature coefficient of the MISER Nd:YAG laser is about $-0.15 \text{ cm}^{-1}/^{\circ}\text{C}$ and the temperature control provided with the laser electronics was sufficient to hold the frequency drift to less than $0.002 \text{ cm}^{-1}/\text{hr}$. To achieve great stability the frequency was tuned to the $18788.451 \text{ cm}^{-1}$ maximum marked with * since this line is near the maximum in the slave gain curve and also near the middle of a mode hop range of the seed laser. This feature consists of three overlapping transition P53(32-0), P103(34-0) and P159(39) with an estimated total width of 0.06 cm^{-1} . The window on the right side of Figure 3.15 shows the simulation of iodine peak and laser modes.

Background Reduction Technique

The I_2 absorption measurement within the temperature tuning range of the seeder gives us a way to eliminate the background scattering in the low frequency CARS experiment.

As we can see from the CARS process energy diagram Figure 3.16,

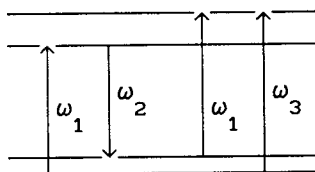


Figure 3.16 CARS Process Energy Diagram

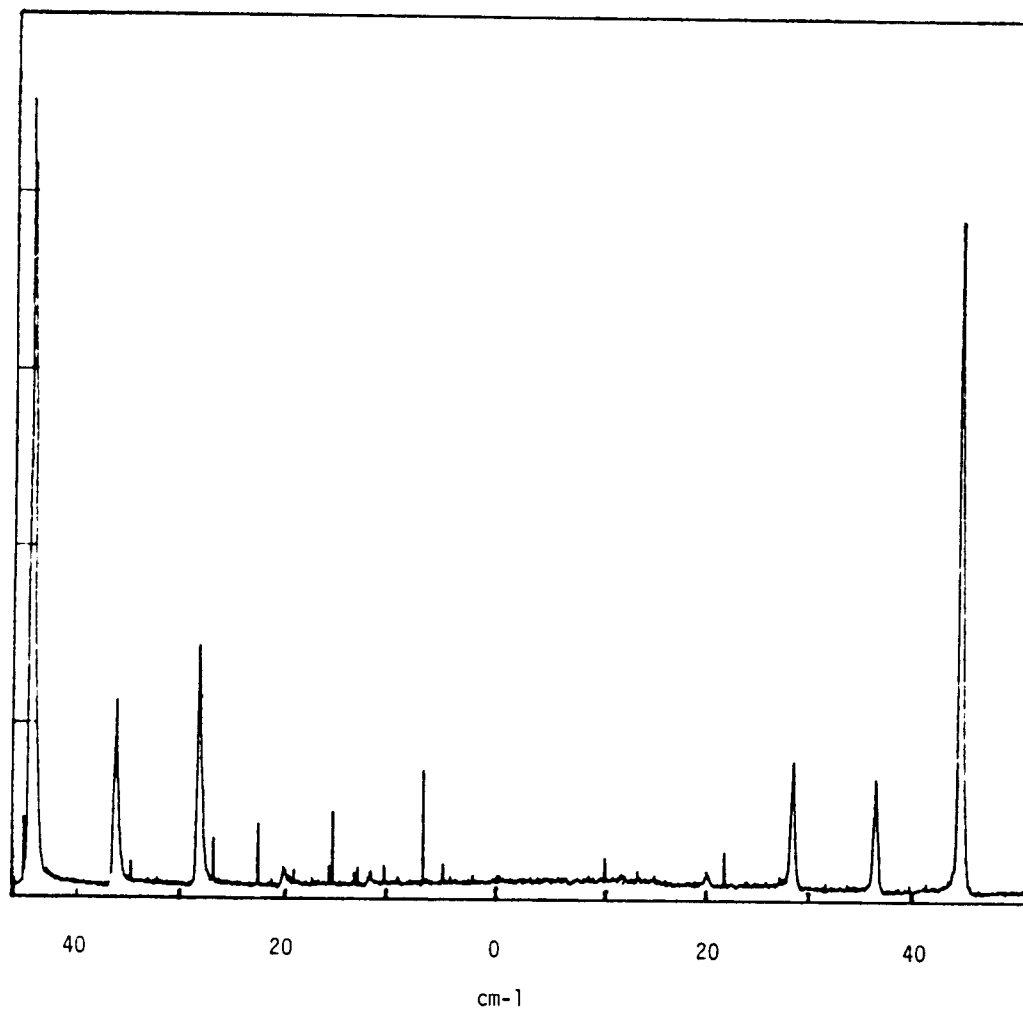


Figure 3.17. CARS pure rotational spectrum of N_2 .

in the low frequency case, when the ω_2 approach to ω_1 , the CARS single ω_3 will also approach ω_1 and ω_2 . In this situation, a very strong scattering will show up in the spectrum, as seen in Figure 3.3.

When the doubled frequency is centered on a strong, sharp I_2 absorption, a simple 10 cm I_2 cell placed after the sample serves to absorb the injection-locked narrow band (0.002 cm^{-1}) ω_1 light without significantly affecting the much broader signal at ω_3 . The rejection of ω_1 is shown in Figure 3.17 where the intense scattering near zero frequency in the spectrum is gone. We can see the base line is very flat throughout the spectrum, but there are some very sharp lines in the spectrum which are obviously not the rotational lines of nitrogen. The elimination of these troublesome artifacts is the subject discussed in the next section.

DEVELOPMENT OF LASER MULTIMODE SHOT REJECTOR

Basic Idea of the Rejector

The ω_1 stray light elimination results obtained in the last section are very encouraging for low frequency spectroscopy, except for the sharp spikes in the spectrum. In order to decide whether they were caused by impurities or the instrument, an experiment was carried out. The laser was tuned to the P53 I_2 line and the resultant transmission through the iodine cell was measured for 1000 shots (Fig.3.18). The light level through the cell was adjusted to avoid saturation of the transition and the zero level was obtained by

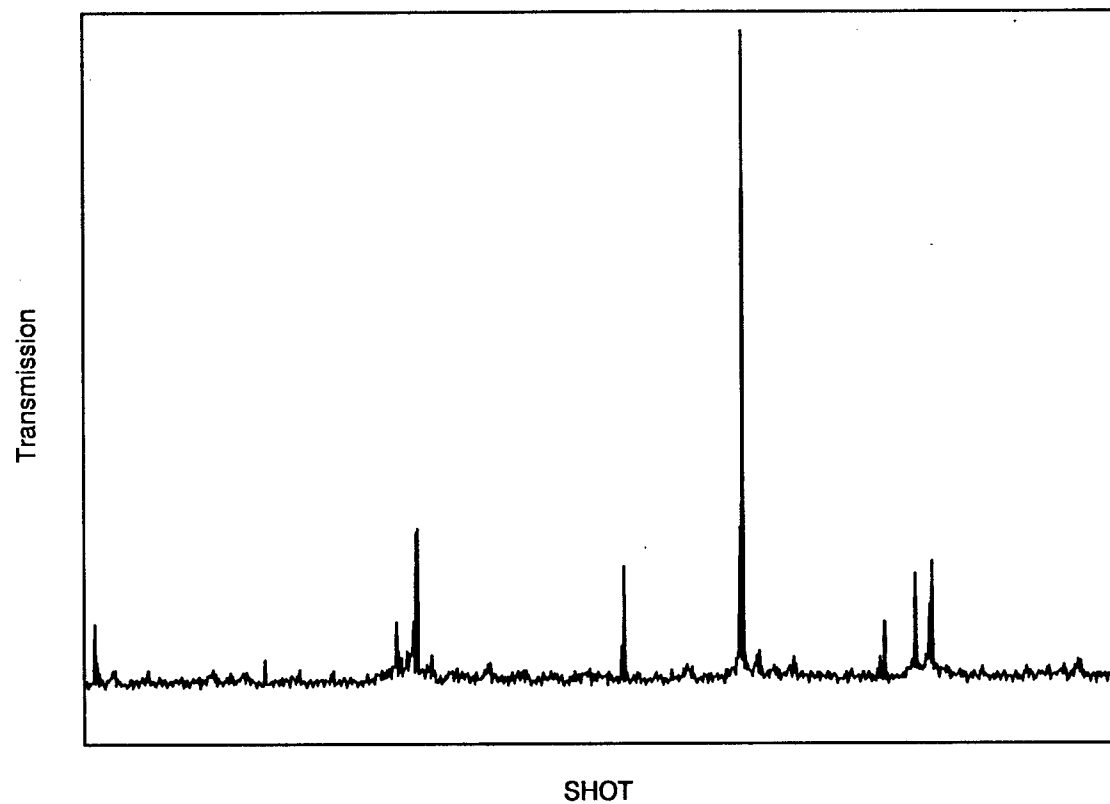


Figure 3.18. Transmission of the 18788.451 cm^{-1} through the I_2 cell.

blocking the photodiode. Apparent are the occasional spikes that arise when the laser output contains one or more additional slave laser modes that fall outside the P53 absorption profile. By taking a CARS spectrum and I_2 transmission spectrum at same time, spikes appear in both spectra at same time. This verifies that those very sharp lines in the CARS spectrum shown in Figure 3.17 are caused by multimode laser shots. These "bad shots" degrade the spectral purity of the source and also produce significant amplitude fluctuations due to mode beating and competition between modes. The latter effects are particularly troublesome in nonlinear experiments such as CARS where the 532 nm output is usually mixed with a multimode dye laser source.

Fig.3.18 suggests that the iodine absorption measurement offers a convenient and positive means of distinguishing good from bad shots, a laser multimode sensor. The problem then is to find a simple and effective way to block those "bad shots" before the resultant CARS signal gets into the boxcar integrator. The *Truth* table of an AND function suggests a way to do so. As can be seen from Table 4.1, two variables A and B must be *True* at same time in order to get a *true* output, in all other cases a *False* output results.

Table 3.1. Truth table for the AND function.

Variables		Result
A	B	M
0(F)	0(F)	0(F)
0(F)	1(T)	0(F)
1(T)	0(F)	0(F)
1(T)	1(T)	1(T)

By applying this principle to our system, we use one photodiode to monitor the Nd:YAG laser output beam to give one AND input and, for the other input, another photodiode monitors the same laser beam after passage through an iodine cell. An AND operation then generates a trigger pulse only for good laser shots and all bad shots are ignored.

Electronic Circuitry

Based on this simple idea, a "bad shots" rejector circuit was designed. A schematic circuit diagram is shown in Fig.3.20. It consists of two channels and a logic operation part. The first channel, a SGD-040 photodiode is used to monitor the basic laser pulse. T_1 is a fast operational amplifier (LH0062) used as a voltage follower to insure that input sees a high impedance. T_2 is an open loop voltage comparator which compares the two input voltages that come from the photodiode and a level adjustment. Any small difference between these two inputs will cause a positive or negative saturated

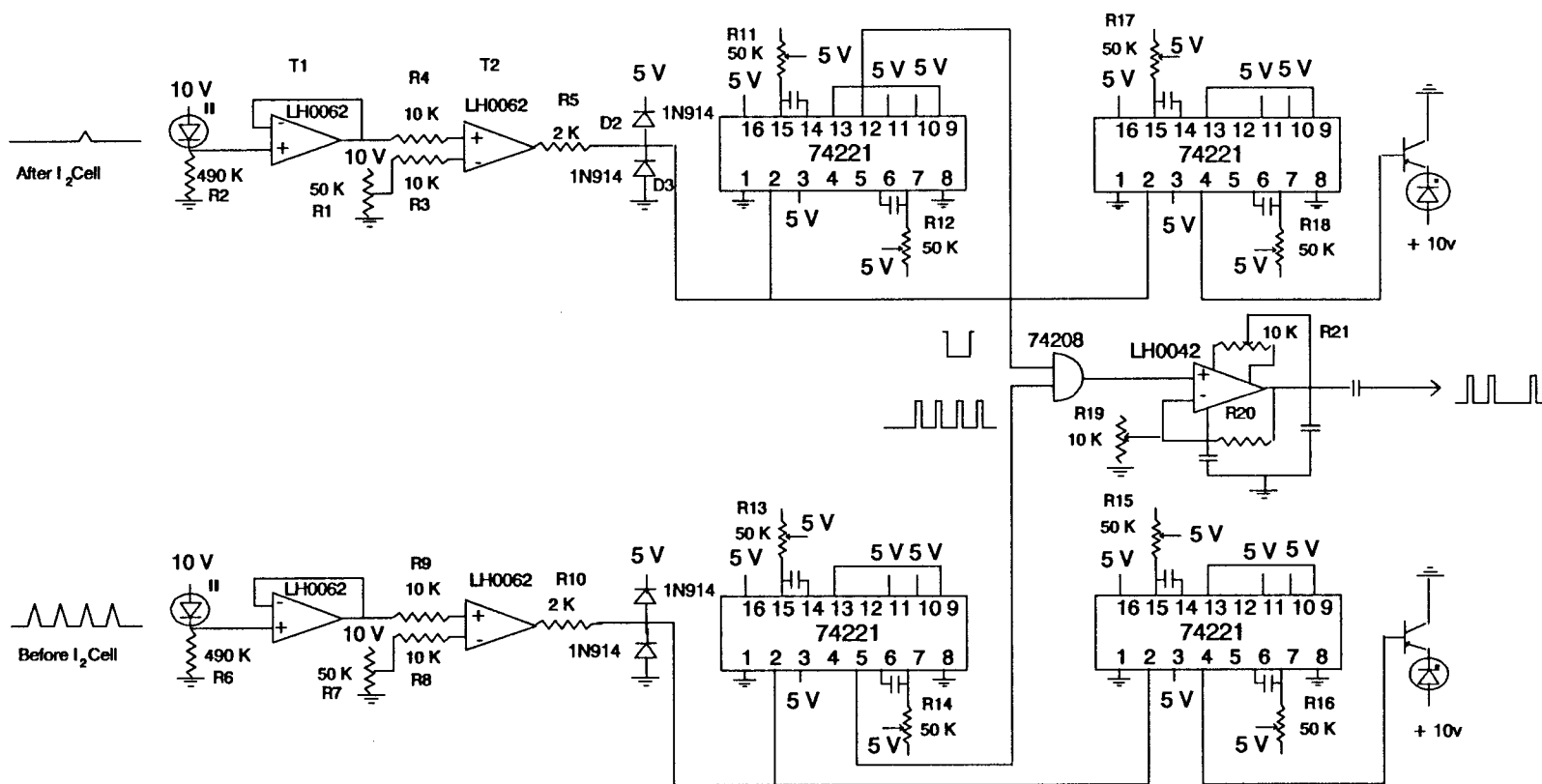


Figure 3.19. "Bad Shot" rejector circuit diagram.

output. A 50 K Ω variable resistor R1 serves as a level adjustment which serves to give flexibility in setting the sensitivity to the frequency jitter of the laser. The two diodes D2 and D3 used on the output of T₂ are to latch the output voltage between 0v and 5v in order to trigger the 74221 flip-flop.^{49,50} The pulse width and time delay of the output of the 74221 can be adjusted by the resistances R11 and R12 in the RC circuit. Those negative pulses are modified in order to have enough width to cover corresponding pulses from the second channel.

The second channel is basically similar to the first channel except it will produce positive pulses every time the laser fires. The outputs of these two channel are send to an AND gate. After the logic operation, only those pulses corresponding to good shots result in a positive 5 volt output which is then sent to gate the boxcar used for signal processing.

The schematic of CARS spectrometer with "bad shot" rejector is shown in Figure 3.20.

Results

As a demonstration of the function of the "bad shots" rejector, CARS spectra of 50 torr of nitrogen gas with and without the "bad shots" rejector. Also, in order to eliminate the Rayleigh scattering near zero shift, the background reduction technique discussed in the first part of this chapter was employed. Fig.3.17, shown previously, shows that the bad shots of the laser that appear as spikes in the

pure rotational spectrum of a 50 torr sample of N_2 . Fig.3.21 shows a similar scan but with the "bad shots" rejector turned on. The absence of "bad shots" in the spectrum shows that the good spectra can now be routinely obtained in this difficult spectral region.

The use of this rejector also yields a improved effective resolution in our experiments. Figure 3.22 shows static high resolution CARS spectra of the vibrational Q-branch of O_2 , taken with and without the multimode rejector. The narrower feature (half width $\approx 0.045 \text{ cm}^{-1}$) results when the rejector eliminates those multimode pulses which occur outside the line width of the I_2 transition. The latter shift and hence broaden the transition (half width $\approx 0.07 \text{ cm}^{-1}$). Also, some small, nonreproducible features on the low frequency side of the transition for spectra are eliminated when the rejector is operational.

Finally, Figure 3.23 shows another comparison of CARS spectra taken by Nancy Triggs with and without the multimode rejector. This is a nonresonant background CARS spectrum of methyl iodide/He in a jet expansion. The top trace was taken without the multimode rejector and, as one can see, there are many spurious peaks in it which are not real because there are no transitions in this vibrational frequency region. The same experiment was then performed with the multimode rejector in and, as one can see from the bottom spectrum, a smoother CARS nonresonant background trace results.

In summary, this work demonstrates that the multimode rejecting method is a very useful technique for three purposes:

LOW-SHIFT NITROGEN ROTATIONAL SPECTRA

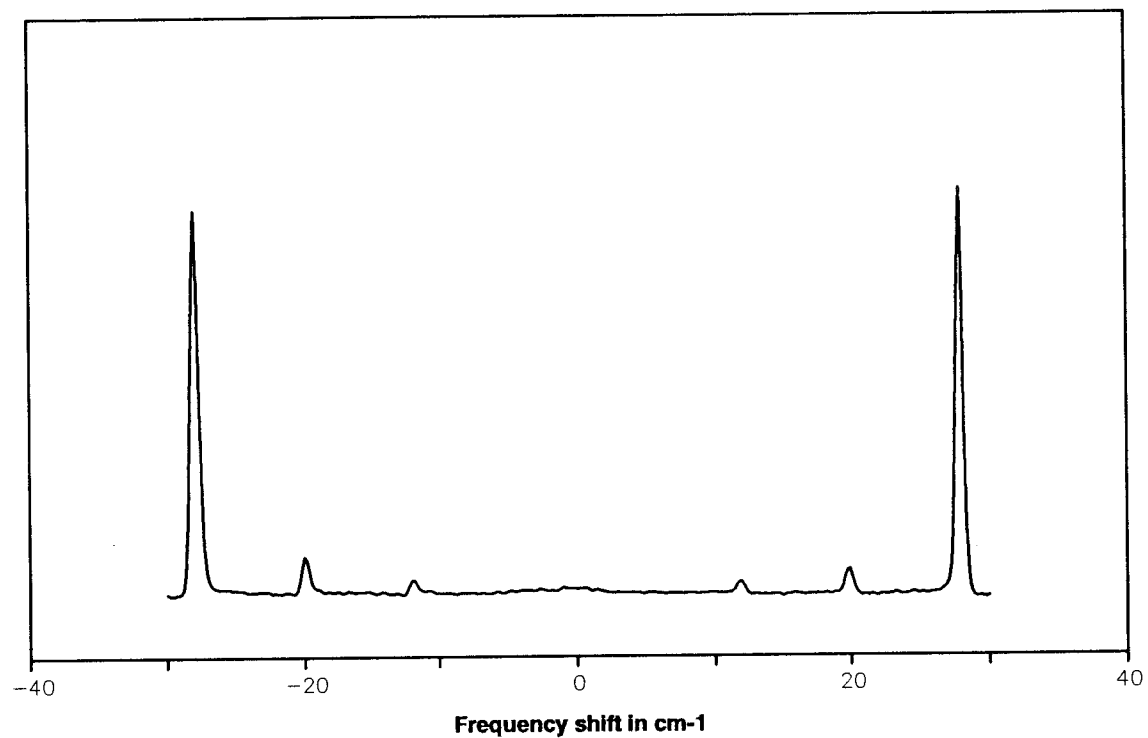


Figure 3.21. Pure rotational CARS spectrum of N_2 taken with "bad shot" rejector.

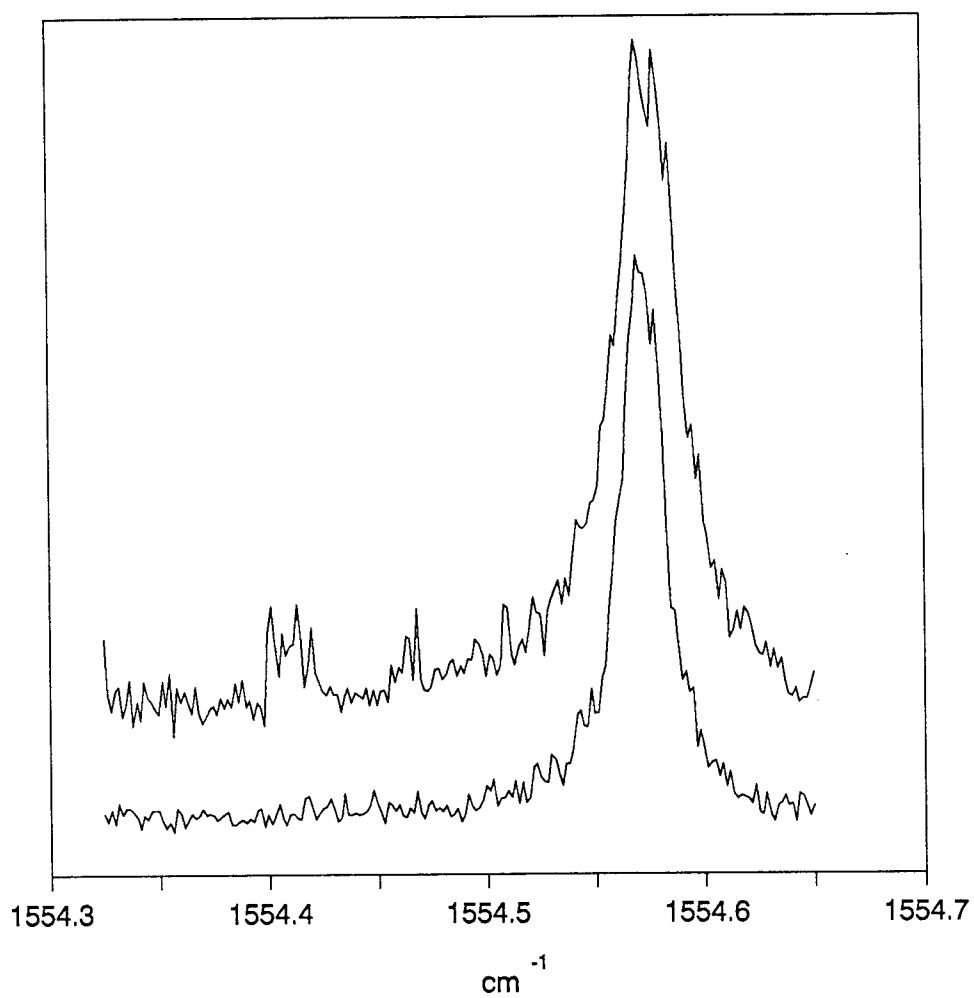


Figure 3.22. O_2 spectra of the Q line taken with and without "bad shot" rejector.

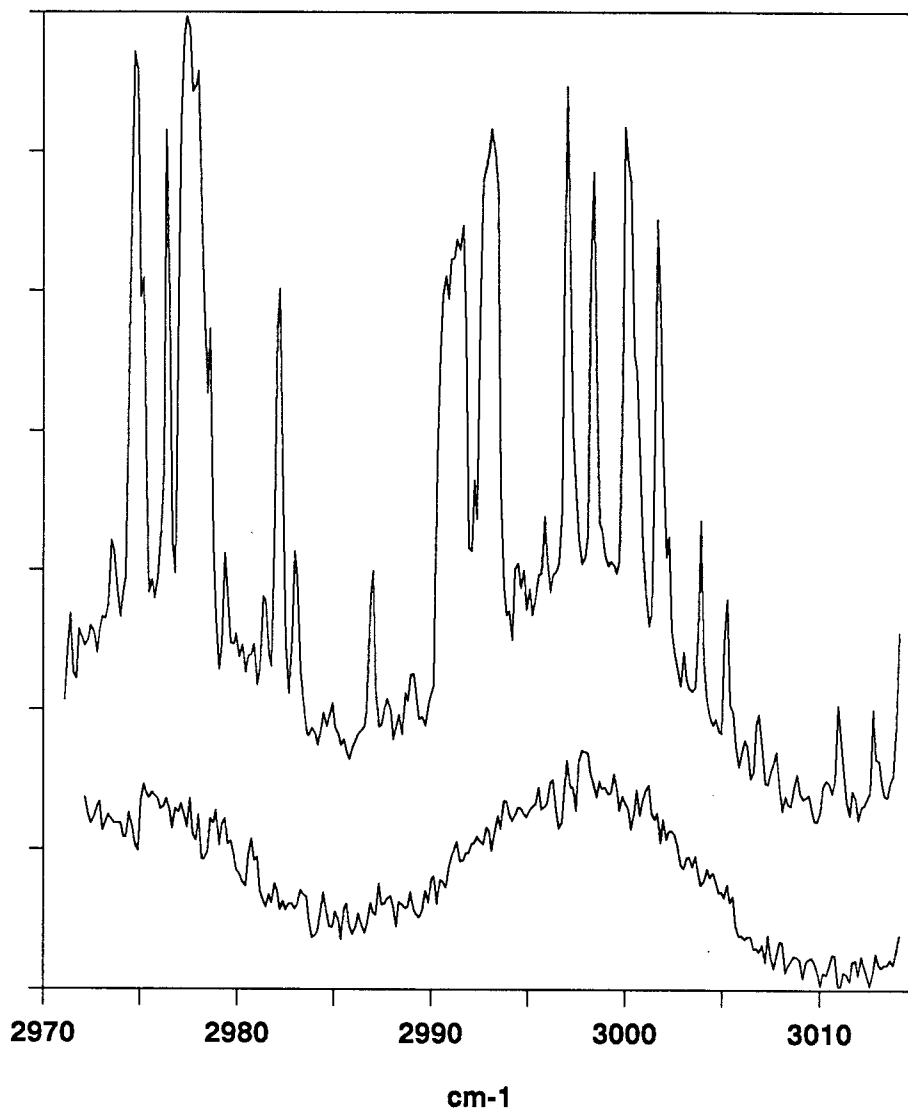


Figure 3.23. Nonresonant background CARS spectrum of methyl iodide/He in jet expansion taken with and without the "bad shot" rejector.

- (a) Detection and rejection of multimode laser shots that cause large amplitude fluctuations in nonlinear CARS experiments.
- (b) Improvement of spectral resolution by ensuring that multimode pulses are rejected and also that single mode pulses not centered on the I_2 absorption are also eliminated
- (c) Elimination of stray ω_1 light propagating with the ω_3 signal by I_2 cell absorption.

The multimode rejector is thus a useful complementary element for the imperfectly seeded Nd:YAG single mode laser for nonlinear spectroscopy and high resolution spectroscopy experiments. Further examples of its use are given in the next two chapters.

CHAPTER 4 APPLICATION OF CARS AND SRL FOR THE STUDY OF INVOLATILE MOLECULES

INTRODUCTION

This chapter presents some preliminary applications of CARS and SRS in a relatively new area of chemistry: the gas phase study of high temperature molecules of low volatility, such as inorganic salt vapors. Small molecular species such as these and their dimer and high polymer aggregate forms, provide an important testing ground for chemical theories of ionic and covalent bonding. Their structures, vibrational frequencies, and thermodynamic properties are of considerable interest. These species are also important technologically in areas concerned with vapor transport and corrosion.^{55,56}

The traditional methods of studying high temperature vapors are mass spectrometry and transpiration but, although these methods are generally successful in establishing the intensity of the species of interest, they provide little or no structural information. For those molecules which are stable at room temperature, such information is obtained either by electron diffraction or by a variety of spectroscopic techniques. In the last ten years or so, these methods have been extended to moderately high temperatures (~ 1000 K) but the considerable difficulties encountered become even more severe at higher temperatures. These problems involve the areas of production, detection, and characterization. For example, the chemical reactivity

of many high temperature species often places a severe constraint on the study of closed systems owing to the lack of a suitable material for the container. This problem can be by-passed by working at low pressures in a molecular beam, but the low concentrations then present serious detection problems, particularly for conventional Raman or infrared spectroscopy. When more sensitive techniques such as UV/vis fluorescence are used, it is found that, although detection is no longer a problem, the spectral richness of ro-vibrational transitions presents new difficulties.⁵⁴ This complexity can be reduced by matrix isolation, where the vapor is quenched by sudden trapping in frozen Ar films, and the application to high temperature chemistry has been used extensively.^{51-53,66-68} Of course, only vibrational transition are seen in matrices and, due to site effects, only an approximation to the desired gas phase frequencies is obtained.

Ideally one would like to maintain a high vapor density while achieving the spectral simplification that comes with cooling. This is not possible under equilibrium conditions for the low volatility samples of interest to us. However, such a result can be achieved under the non-equilibrium cooling environment that occurs in jet expansions. Our goal then was to explore this possibility using the sensitive coherent Raman methods developed in our laboratory. To our knowledge no previous Raman work of this type has been done on non-volatile compounds. Here we present some description of our experimental efforts and spectra of three test molecules: AsCl_3 , HgCl_2 , and CS_2 .

EXPERIMENTAL

High Temperature Nozzle Cell

For effective cooling in a free expansion jet, the high temperature nozzle has to work not only at a temperature up to about 1200 K but also at high pressures of driving gas. In addition the cell has to be corrosion resistant at high temperature. Figure 4.1. shows a high temperature cell design based on the use of either thin wall stainless steel or tungsten tubing (0.01" - 0.02" thickness). Two Swage-locks were used to seal the two ends of the tubing to achieve a high pressure seal and to allow easy loading of solid samples such as AsCl_3 and HgCl_2 . Small diameter stainless steel tubing was connected to one of the Swage-lock to serve as N_2 driving gas feedthrough. The two Swage-locks are also attached to water-cooled copper electrodes which are connected to a low voltage-high current power supply. By passing current through the thin wall cell, resistive heating occurs, with the hottest region near the center of the tube. A small hole of 0.015 mm diameter was drilled in one side of the tube to serve as the nozzle opening and the entire assembly was then placed in a vacuum chamber.

SRL Spectrometer

Since the vibrational and rotational transitions of heavy non-volatile molecules occur in the $0 - 1000 \text{ cm}^{-1}$ range, a low frequency coherent Raman capability was essential for this work. The

Free Jets Expansion Cell

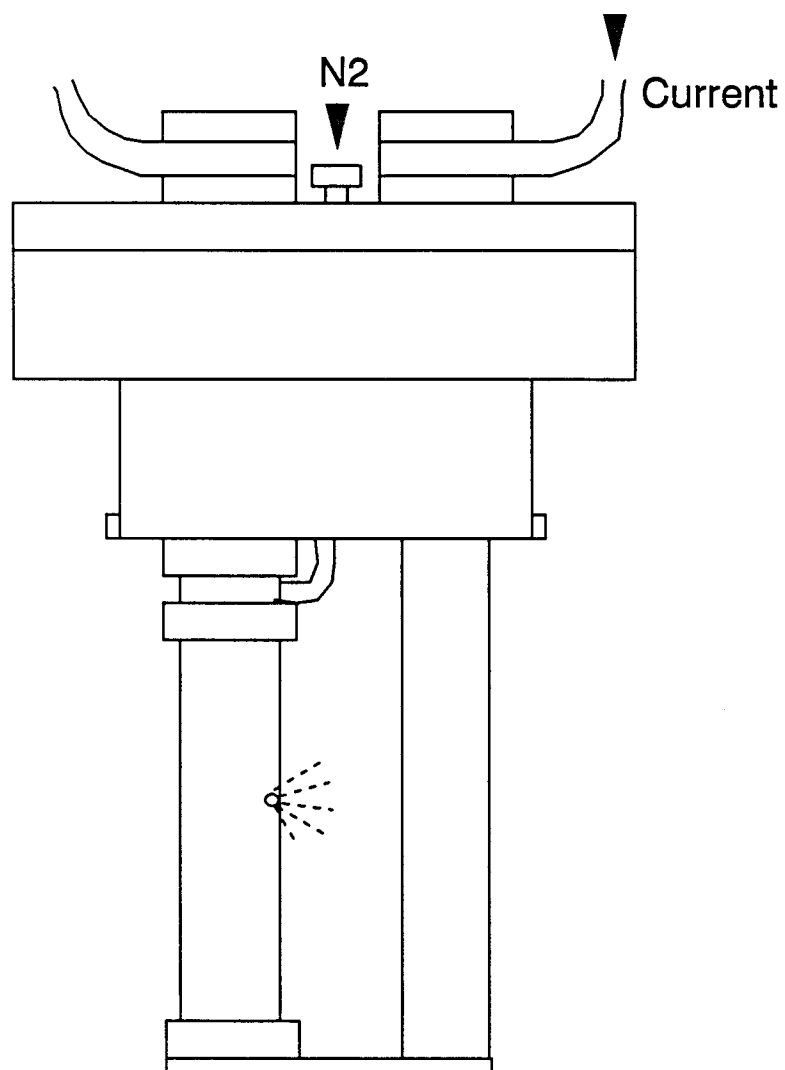


Figure 4.1. High temperature cell.

main features of the experimental system for low frequency CARS have been discussed in the the previous chapter. In this section we will briefly describe the Raman loss system which is used in our high temperature experiment.

Figure 4.2 shows a schematic of the SRL spectrometer. It consists of a tunable pump lasers and a fixed frequency probe laser because in SRS the Raman spectrum is recorded by scanning the frequency difference between two laser interacting with the sample. The pump laser system produces powerful (up to 20 mJ/pulse) single frequency pulses of 10 nsec duration, by injection seeding a home built three stage pulsed dye amplifier (PDA). The probe light comes from a single frequency argon or krypton ion laser. Raman shifts from 4700 to 0 cm^{-1} can be accessed by using different laser lines of the argon or krypton ion laser. The scan range for any given probe laser frequency is given by the range of the PDA, which is about 300 cm^{-1} for a given dye. The detail of tuning ranges can be found in reference 76.

The timing of the YAG laser is adjusted so that the output of the PDA occurs during a 200 μsec probe interval and a small part of the pump light is used to trigger a boxcar integrator. There are two channels in the boxcar integrator. One integrates the transient gain or loss in probe laser power over 12 nsec while the second channel is delayed by 15 nsec and integrates a 12 nsec window of the baseline. This baseline value is then electronically subtracted in an analog module to cancel out baseline shift caused by low frequency noise. The analog output of the boxcar average is then digitized by computer and averaged over many laser shots by a data collection program.

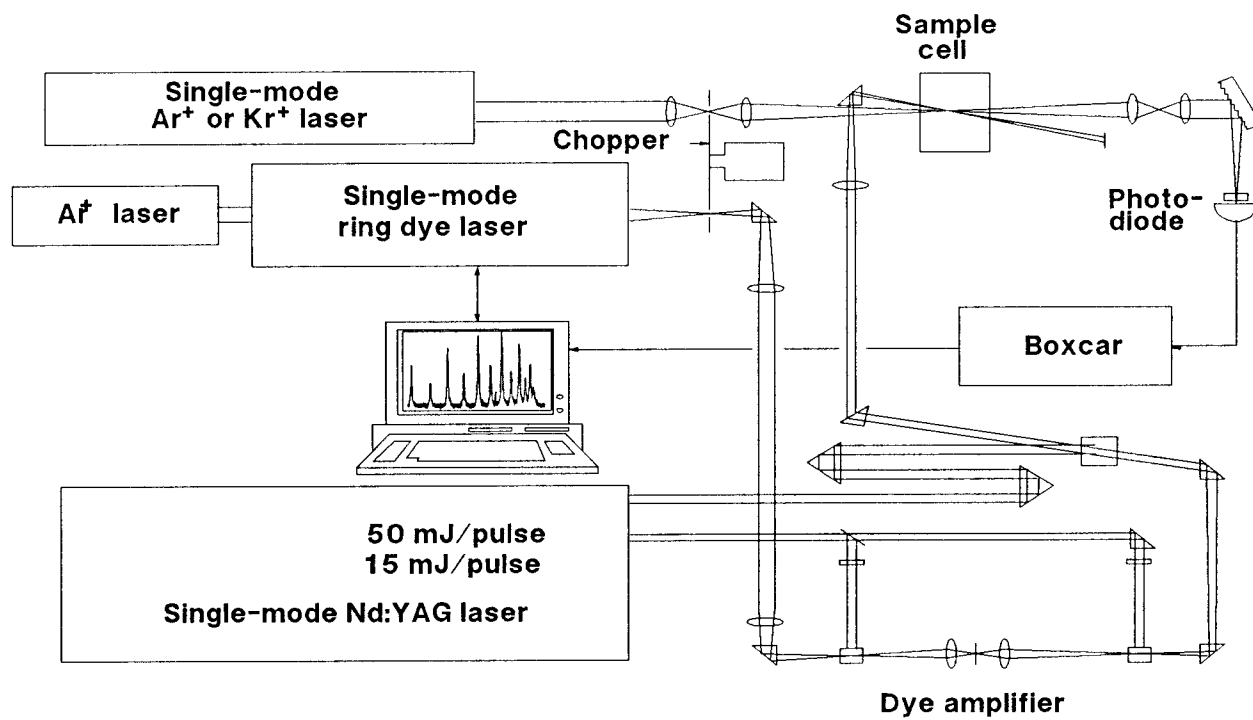


Figure 4.2. Schematic of high resolution stimulated Raman spectrometer.

RESULTS

The AsCl_3 Molecule

AsCl_3 is a simple pyramidal molecule of some importance in the semiconductor industry. The equilibrium vapor contains both monomers and higher aggregates whose composition is of interest but is largely unknown. It thus was viewed as a possible candidate for study by CARS or SRL methods.

Since AsCl_3 is reasonably volatile (300 torr at 383 K), our first efforts involved a CARS study using simply a hot sealed cell at 383 K. Figure 4.3 shows a static pure rotational CARS spectrum of AsCl_3 under these conditions. It is apparent that the spectrum is very complicated and congested. In this spectrum no individual lines were resolved, but reasonable overall agreement of the spectral envelope of overlapping R and S rotational branches was obtained with a calculated spectrum, shown in Figure 4.4. Other spectral contributions come from the overlapping chlorine isotopic bands, and from excited vibrational states. The results show graphically the problem of high temperature studies for such molecules and illustrate the desirability of cooling by jet expansion.

The HgCl_2 Molecule

At this stage in the work, it was decided that HgCl_2 would be a better test case than AsCl_3 because it is known to be linear with simpler spectrum. Also, it is less volatile so that higher temperature

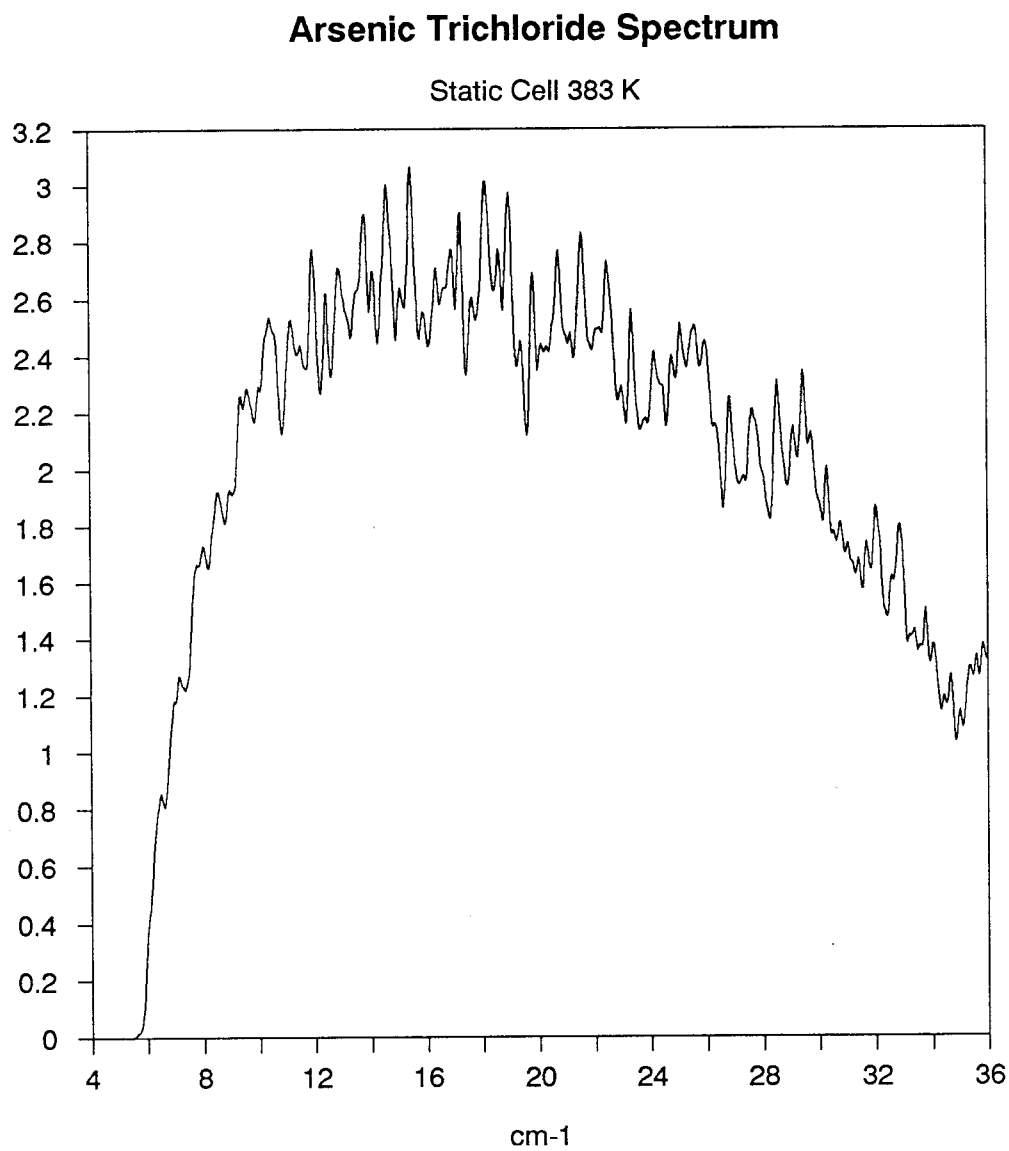


Figure 4.3. Pure rotational Raman loss spectrum of AsCl_3 .

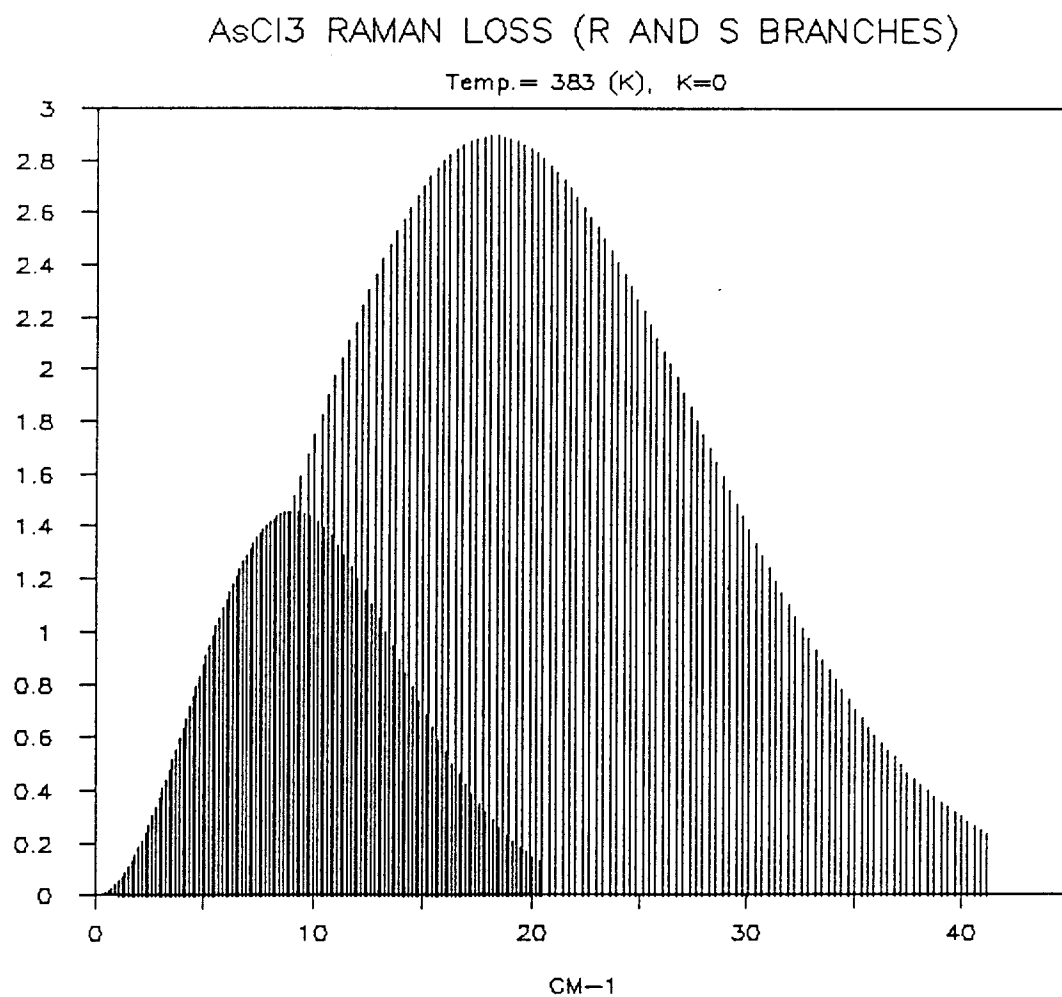


Figure 4.4. Calculated R and S branches spectra of AsCl₃.

are required, one of our design objectives. Finally, gas phase mercuric chloride has been studied previously by infrared, spontaneous Raman, and electronic diffraction, as well as by mass spectrometric methods. Thus a reasonable amount of information is available, although no CARS or SRS spectra have reported.

Figure 4.5 shows two high temperature pure rotational SRS spectra of HgCl_2 , expanded in a jet. The two scans from separate experiments were recorded at nozzle cell temperature of 520 K and at an N_2 driving gas pressure of 10 atmosphere. At the sample point the driving gas rotational temperature was determined to be about 105 K so that significant cooling had occurred. The percentage of HgCl_2 present in the jet was calculated from vapor pressure data to be about 15%.

It is apparent that the congested spectrum is only partially resolved even though we used the high resolution (0.003 cm^{-1}) Raman loss apparatus. The B value of HgCl_2 is known to be 0.0453 cm^{-1} so that the $2B = 0.0906 \text{ cm}^{-1}$ spacing of the pure rotational Raman lines should be easily discerned. Of course, since there is 24% Cl^{37} abundance in nature, three isotopic forms contribute to the spectrum: $\text{Hg}^{35}\text{Cl}_2$ (70%), $\text{Hg}^{35}\text{Cl}^{37}\text{Cl}$ (23%), $\text{Hg}^{37}\text{Cl}_2$ (7%). Using the two most dominant forms, a calculated pure rotational spectrum of HgCl_2 is shown in Figure 4.6. Because of the isotopic effect, the spacing between rotational lines of $\text{HgCl}^{37}\text{Cl}^{35}$ is smaller than that of HgCl_2^{35} lines so that appreciable overlap occurs in the spectrum.

It is interesting to note that, due to molecular spin statistics, $\text{Hg}^{35}\text{Cl}_2$ is expected to show intensity alternation of 10 to 6 for odd J to even J lines ($I = 3/2$ for ^{35}Cl). Because of the overlapping only

HgCl₂ pure rotational spectrum

T=520 K, P=10 atm

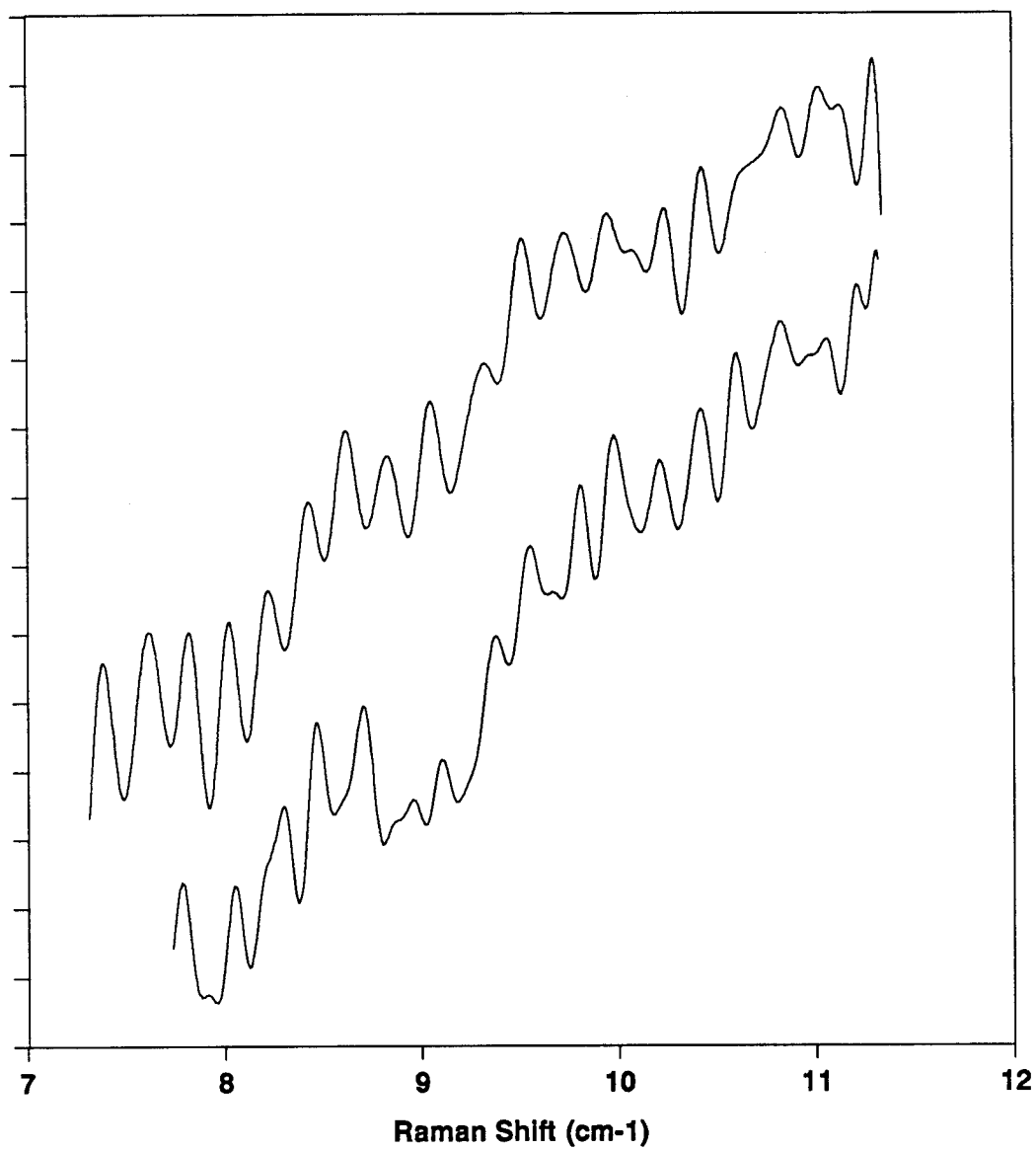


Figure 4.5. Pure rotational jet spectrum of HgCl₂.

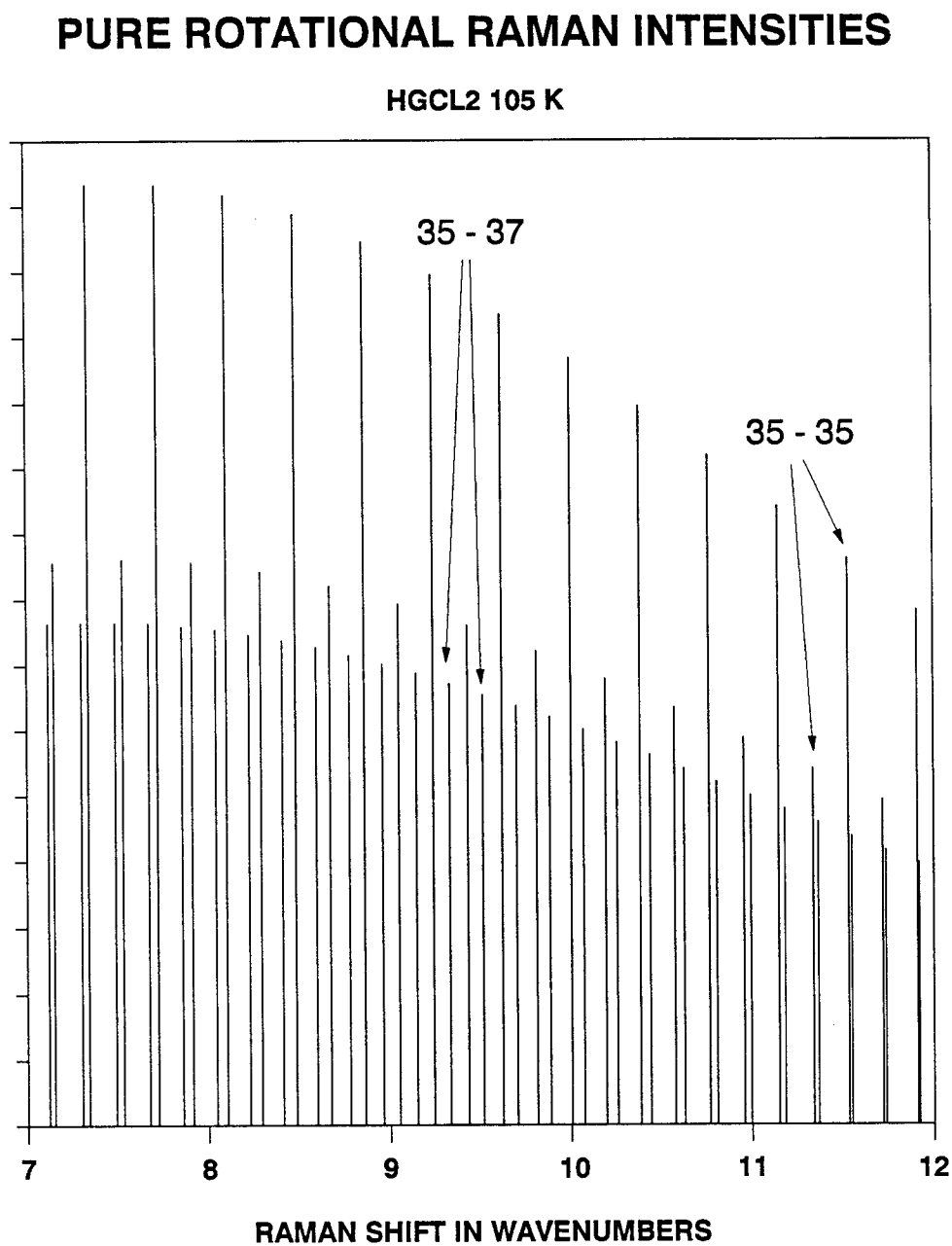


Figure 4.6. Calculated pure rotational spectrum of HgCl_2 .

the more intense odd J lines are distinguishable. Using the frequencies of these, an approximate B value of 0.0493 cm^{-1} was deduced from the spectrum, in fair agreement with a value of 0.453 obtained from conventional spontaneous Raman spectroscopy.⁶² Our B value yields a Hg-Cl bondlength of 2.19 , in close accord with a 2.20 \AA length deduced from electron diffraction experiments.

The CS_2 molecule

CS_2 was chosen as another simple test molecule of low volatility because it is liquid and hence subject to "bumping" in the hot nozzle cell, a possible experimental problem of concern. It's spectrum can also give a direct measure of rotational cooling in the jet whereas, for HgCl_2 , this was inferred only from the N_2 driving gas spectrum. Finally, we were interested in the possible detection of CS_2 clusters that might form in the jet.

Like HgCl_2 , carbon disulfide is a symmetric linear molecule belonging to the point group $D_{\infty h}$. The ground electronic state is $^1\Sigma_g^+$ and, since the spin of the ^{32}S nucleus is zero, all rotational levels of the C^{32}S_2 molecule which are antisymmetric in the simultaneous exchange of equivalent nuclei are absent. For the vibrational ground state this results in the absence of all rotational levels with $J = \text{odd}$. In these studies both pure rotational and ν_1 vibrational regions were examined.

(a) Pure rotational region

Both the background reduction technique and the Nd:YAG laser multimode rejector presented in chapter 3 were used for a CS₂ pure rotational CARS experiment. Figure 4.7 shows a spectrum of equilibrium CS₂ at room temperature, while figure 4.8 shows a jet spectrum. By comparing these, it is apparent that, because of the cooling from the jet expansion, the low rotational state transitions are enhanced. A rotational temperature of ~ 100 K was obtained by fitting the spectrum in figure 4.8 to a theoretically calculated spectrum. The rotational spacings are in good accord with those deduced from the known B value for CS₂ (0.0109 cm^{-1}).

Some effort was made to detect CS₂ clusters in the jet. The phase transitions of vapor to liquid for CS₂ is 163 K so liquid formation could have occurred in the 100 K jet. However no evidence of liquid or solid cluster features was seen in either the low frequency region or at low vibrational frequencies space (lattice mode region). Accordingly, a search was then made in the higher CS stretching frequency region by using SRS techniques.

(b) Vibrational region

Vibrational spectra generally are dominated by Q-branch rotational lines which are more closely spaced than R and S lines. For this reason we employed the higher resolution Raman loss technique to study the Q branch of the ν_1 symmetric stretching vibration of CS₂. Figure 4.9 shows several ν_1 Q-branch spectra at different nozzle

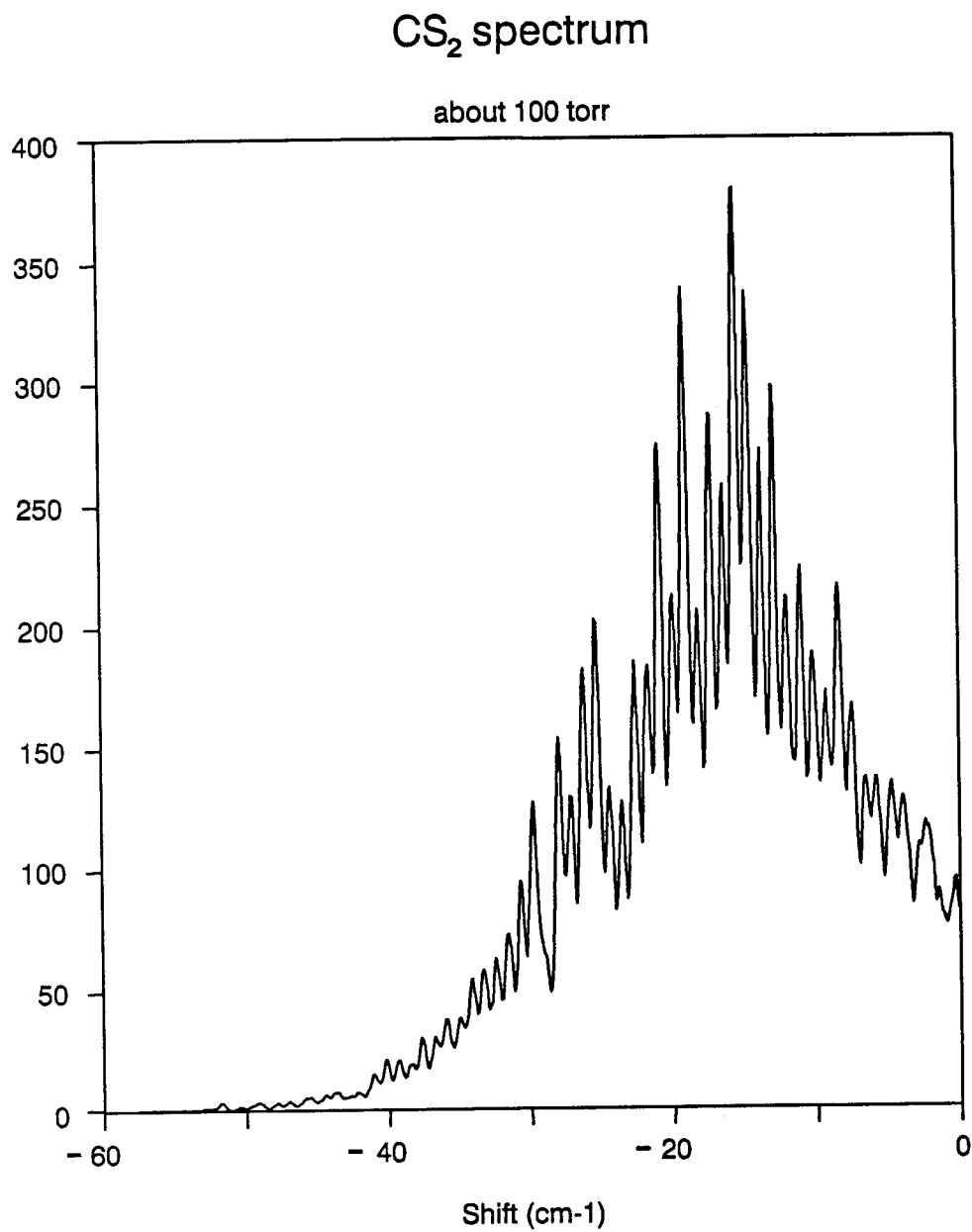


Figure 4.7. Pure rotational equilibrium CARS spectrum of CS_2 .

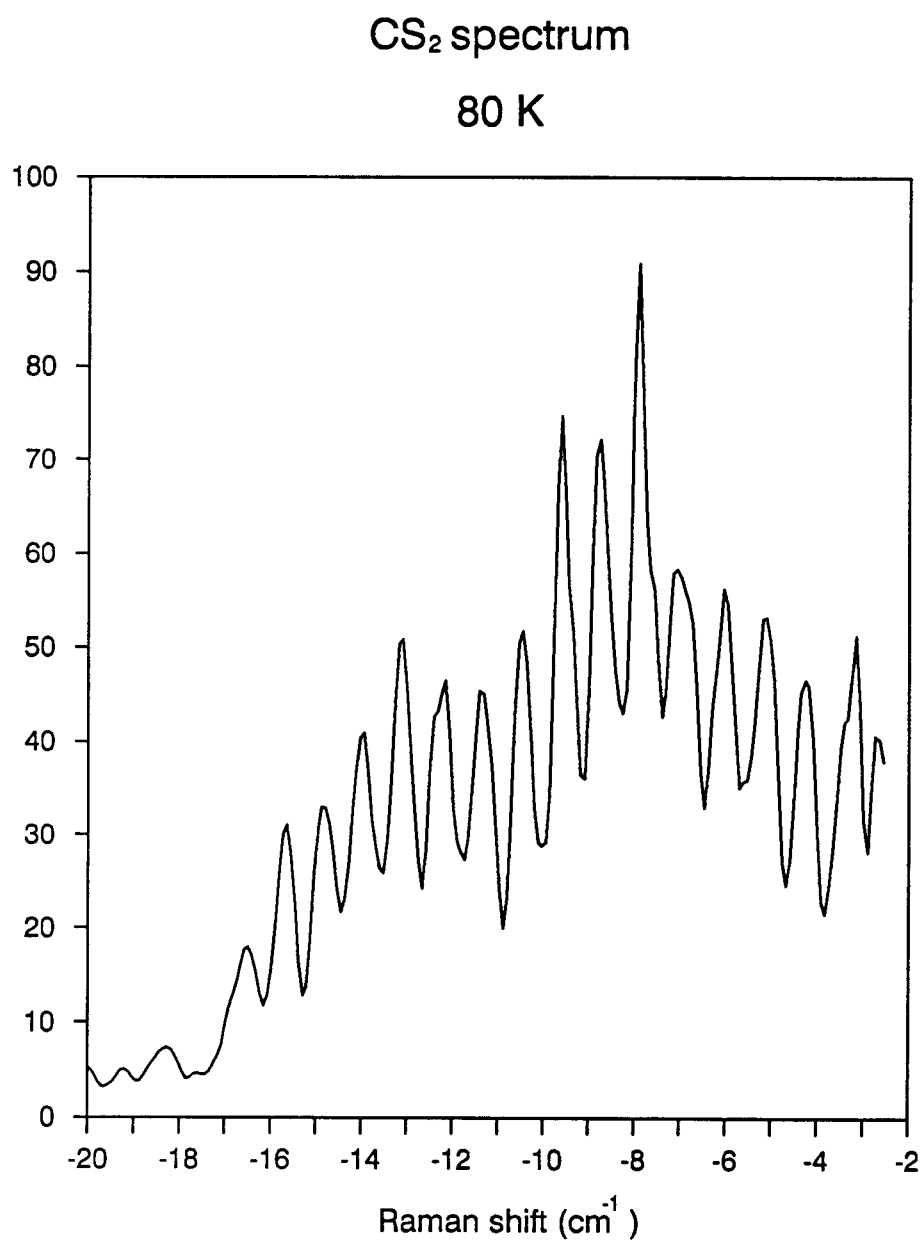


Figure 4.8. Pure rotational CARS spectrum of CS_2 in jet.

CS₂ Q-branch spectra

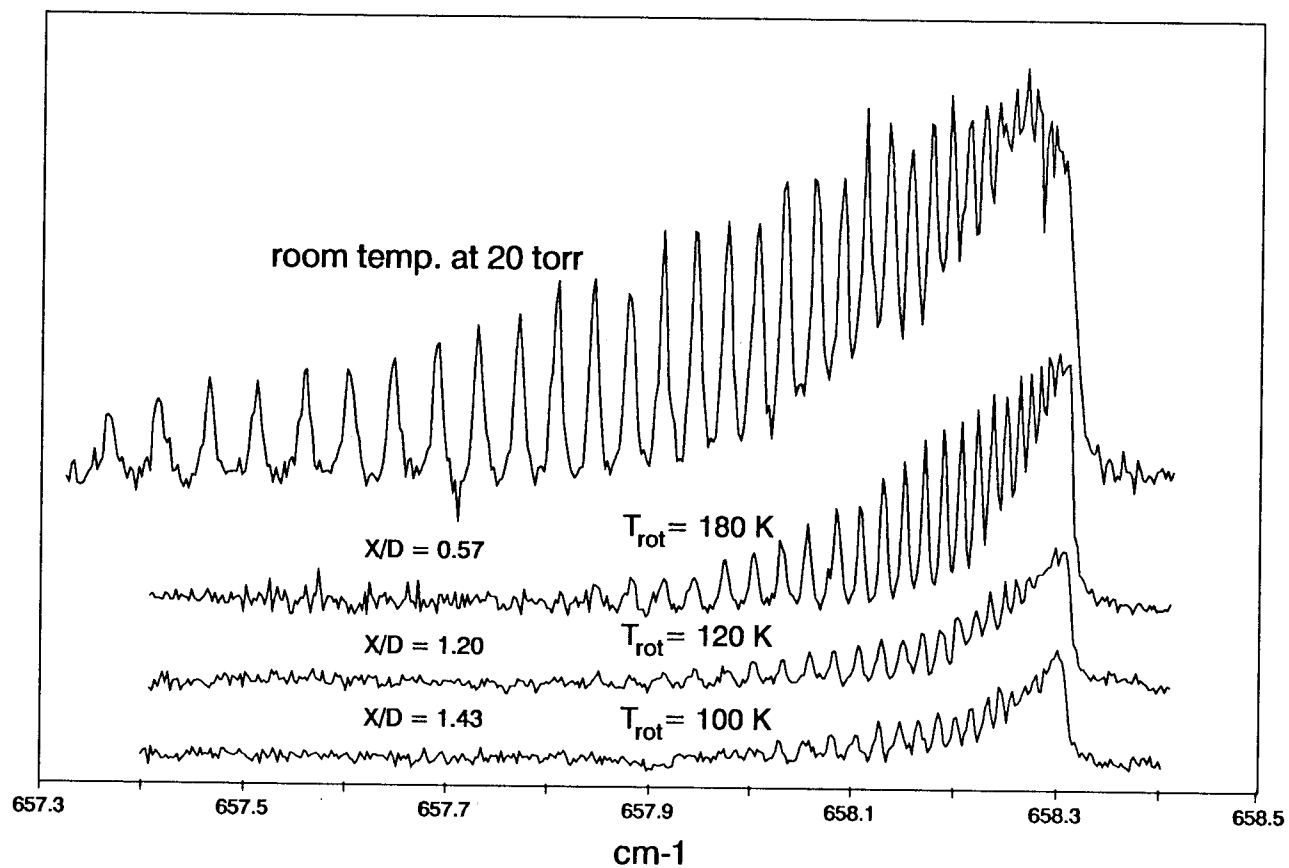


Figure 4.9. High resolution equilibrium and jet spectra of CS₂.

distances (X/D). As one can see, the rotational temperature becomes colder as X/D increases. The S/N is good and these results offer encouragement for continuation of such studies of "heavy" molecules. However, under the conditions of the experiments, no evidence of cluster features were seen in either this ν_1 vibrational region nor at lower frequencies. The absence of low frequency feature is perhaps understandable if any clusters formed simply supercool (as seen for N_2 in the next chapter) and hence produce no lattice vibrations. However liquid feature in the ν_1 region should be detectable and further efforts to examine this region by the more sensitive CARS method are desirable.

SUMMARY

Initial spectra obtained for $AsCl_3$ in a hot cell are highly congested and illustrate the need for spectral simplification by cooling. Subsequent studies demonstrate that CARS and SRS spectra can be obtained for cold jets of relatively low volatility molecules contained in a heated nozzle cell. Spectra of $HgCl_2$ and CS_2 show rotational temperatures of the order of 100 K, factors of about 4 to 5 lower than the nozzle temperatures.

Although these results are modest at this stage, they do serve to define the primary problem with coherent Raman studies of this type. It is clear that further work on the nozzle cell is needed to increase the sample volume since currently spectra can only be recorded for about 30 minutes before the cell is empty. Also, problems with

plugging of the nozzle opening occurred in the HgCl_2 experiments and a larger sample volume would allow increase of this nozzle hole diameter.

One unfortunate aspect of a CW nozzle cell of the type used in this work is the poor utilization of sample since probing occurs only during the 10 ns laser pulse for each 100 ms period, a duty factor of only 10^{-7} . It would be highly desirable to develop a heated pulsed value assembly for which a more favorable duty cycle would be obtained. One way to achieve this might be to use part of the 10 ns laser pulse itself to vaporize sample of interest into a pulsed gas jet just prior to expansion. Sample decomposition may be a possible concern here, as is the mechanism for replenishing the sample at the vaporization point. Further work to explore these various possibilities is suggested.

CHAPTER 5 STUDIES OF SMALL CLUSTERS IN FREE JET EXPANSIONS BY HIGH RESOLUTION CARS

INTRODUCTION

Condensation or nucleation processes occur frequently in every day life (e.g. in the birth of raindrops in Oregon), and it also plays a very important role in many areas of science such as meteorology, aerodynamics, jets propulsion and even astronomy. The nucleation event involves the "sticking together" of gas molecules through many-body interactions, to form small clusters by the release of a certain amount of energy associated with a change to the liquid phase, and even to the solid phase. Condensation or nucleation processes thus impact wide areas of science and the details are interesting to many scientists.

From the spectroscopic point of view, we would like to see how the vibrational frequency of molecules changes during nucleation as that can give insight into the role of attractive and repulsive forces during the cluster bonding process. As discussed later, such studies can also give an indication of the thermodynamic temperatures and cluster sizes in free jet expansions used in recent years to prepare small aggregates.

Some theoretical and experimental studies have been made in the last ten years on the unusual physical properties of small "ultrafine" particles in the 1 - 100 nm diameter size range. For example, several research groups have used molecular dynamics simulations to study the

size dependence of the liquid-solid phase transition temperature in argon.^{68,69} The influence of impurities and charged species in the nucleation process has also been studied.⁷⁴

More recently in our laboratory the N_2 nucleation process has been studied by Rainer Beck using the SRS technique.⁷⁵ This chapter describes a similar study using an alternative high resolution coherent Raman technique (CARS) to study cluster formation in a free jet expansion. The influence of impurities such as CO_2 in the nucleation process of N_2 , and a comparison of high resolution CARS and SRS techniques in studying the cluster formation are discussed. The effect of nozzle shape is examined and the cooling and phase transition of the clusters are probed. The mean clusters size formed in our jet expansions was estimated from cooling curves to be 16 to 33 nm. A gradual "isothermal" model is considered to be the best to explain the freezing process during these jet expansion. An extrapolation formula was deduced for the supercooled liquid N_2 to give temperature prediction for the microdrops and the results fit the gradual "isothermal" model well.

EXPERIMENTAL

High Resolution CARS Spectrometer

Figure 5.1 shows a schematic of the high resolution CARS spectrometer which basically contains the same main elements as that of the stimulated Raman spectrometer, such as the Coherent 699-29

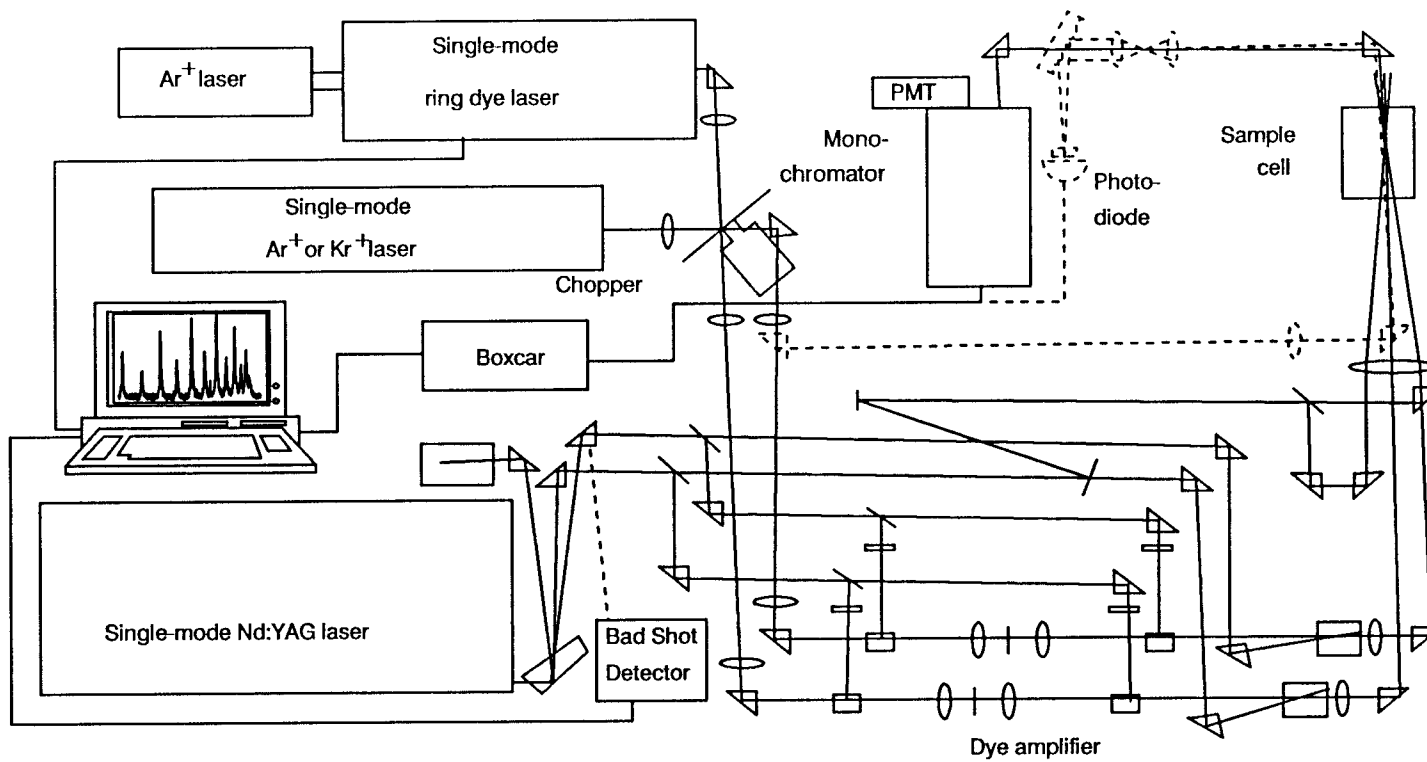


Figure 5.1. Schematic diagram of high resolution CARS spectrometer.

tunable ring dye laser, single mode Nd:YAG laser and home-built injection seeded three stage dye amplifier. Each of these components has been discussed in preceding chapters. Experimentally, the main differences in the high resolution CARS and SRS setups are the laser beam arrangements and the signal detection systems. For crossed beams BOXCARS two ω_1 beams and one tunable ω_2 beam are needed. By using different laser lines of the Ar^+ or Kr^+ laser and a second home-built injection-seeded dye pulse amplifier as shown in Figure 5.1, a different frequency of ω'_1 can be produced. By combining the ω'_1 and green beam ω_1 as well as the tunable dye beam as ω_2 , we can cover all of the molecular rotation and vibration energy region. Unlike the signal detection system in the SRS spectrometer, a photomultiplier and monochromator are used in the CARS system.

Frequency Calibration

The frequencies of the I_2 absorption in the visible range are known very accurately⁴⁹ and were used to calibrate the frequencies of the ring dye laser and the Nd:YAG pulsed laser. The output frequency of the Nd:YAG laser was tuned to an I_2 absorption at $18788.451 \text{ cm}^{-1}$ which serves two purposes that were discussed in chapter 3. An absorption spectrum of I_2 was recorded simultaneously with the CARS spectrum by sending portion of the cw ring dye beam through a I_2 cell with a pressure of 0.25 torr at room temperature. By knowing the exact frequencies of ω_1 and ω_2 , the CARS signal ω_3 can be accurately deduced.

One concern for CARS frequency measurements (compared to SRS) is the extent to which nonresonant background χ_{NR} contributes to frequency shifting, especially for the large χ_{NR} case when the sample is heavily diluted by driving gas. The relation between the frequency shift $\delta\omega$ and χ_{NR} can be obtained by setting the frequency derivative of $\chi^{(3)}$ to zero,¹⁵ that is

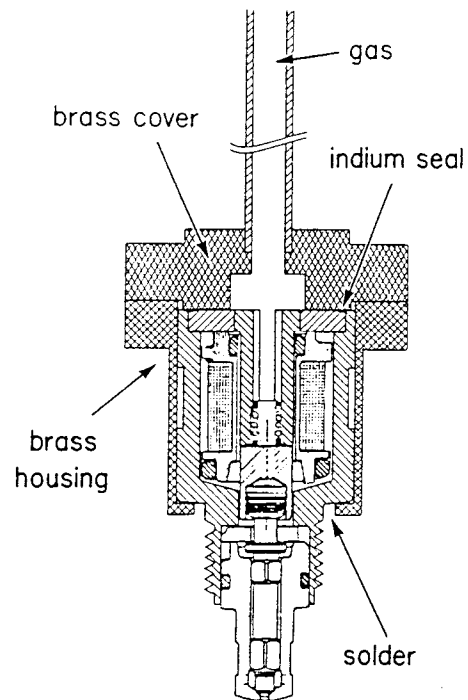
$$\frac{\delta\omega}{\Gamma} = - \frac{\chi_{\text{MAX}}''}{2\chi_{\text{NR}}} \pm \left[\left(\frac{\chi_{\text{MAX}}''}{2\chi_{\text{NR}}} \right)^2 + 1 \right]^{1/2} \quad (5.1)$$

From this it can be seen that the + sign corresponds to the peak maximum which is shifted by amount 0 to Γ as $\frac{\chi_{\text{MAX}}''}{2\chi_{\text{NR}}}$ decreases from a large value to zero. For nitrogen $\Gamma \approx 0.05 \text{ cm}^{-1}$ and for neat clusters, $\frac{\chi_{\text{MAX}}''}{2\chi_{\text{NR}}} \approx 0.05$ so that the maxima shift is about 0.0025 cm^{-1} which is close to our spectrometer resolution. Therefore, this effect was ignored in our cluster frequency measurements.

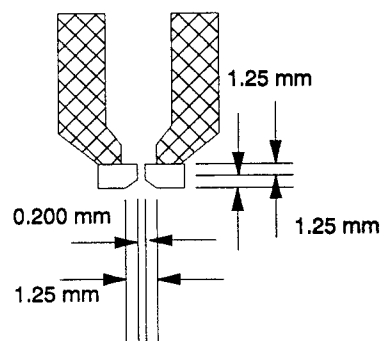
Pulsed Jet Assembly

A cooled, pulsed nozzle is required for cluster formation studies. Our nozzle is based on a commercially available BMW fuel injector valve, as modified extensively by George Pubanz.⁷⁶ The details of the pulsed nozzle is shown in Figure 5.2a.

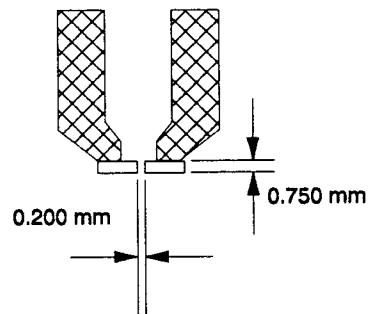
To favor cluster formation during jet expansions, the valve assembly is cooled about -100°C by a stream of cold air produced by blowing dried compressed air through a large reservoir of liquid N_2 .



(a)



(b)



(c)

Figure 5.2. (a) Cross-section of pulsed nozzle assembly. (b) Cross-section of cone nozzle tip. (c) Cross-section of shim nozzle tip.

The temperature of the valve assembly can be adjusted by changing the flow rate of compressed air. The temperature of the sample gas was measured with a thermocouple placed inside the valve housing.

Several round and slit nozzles were tested by Rainer Beck and a long channel nozzle was found suitable for his experiment⁷⁵. I went a little bit further in testing the nozzle geometry most favorable to the formation of clusters in free jet expansions and found that a cone nozzle, a nozzle whose diameter increases along the flow direction, was better in enhancing the formation of clusters. The flow becomes supersonic inside the nozzle and the cooling actually condenses the vapor into microdrops on the inside of the nozzle. The details of the dimensions of the cone nozzle are shown in Figure 5.2b. One of the advantages of the cone nozzle in comparison with the channel or pinhole nozzle is the greater number of collision experienced by the flowing molecules for a given temperature drop.⁷⁷ The disadvantage is that probing of the early stages of droplet formation was not possible for the expansion condition used in these studies. In the closing phase of this work, a second shim nozzle (Figure 5.2c) was used for comparison purposes. This too gave clusters, but at somewhat colder nozzle conditions and higher driving pressure.

RESULTS

Comparison of High Resolution CARS and SRS in Studying Cluster Formation in Free Jet Expansion

It is instructive to give a comparison of the two techniques, CARS and SRS, in studying cluster formation in the free jet expansion at this point. In the Raman loss technique, the signal is superimposed on a high background, but the CARS signal virtually lies on a zero background. Therefore, the CARS signal should be more sensitive. Beside this, the CARS signal is proportional to the square of the density difference of the upper lever and lower lever but the SRS signal is linearly proportional to the density difference (see Chapter 2).

Figure 5.3 shows experimental results of the comparison of CARS and SRS in measuring of N_2 cluster formation in the jet expansion. The experiment measured the liquid region from the tip of the nozzle to the point of the liquid to β -phase solid transition. The experimental results clearly show that the over all signal to noise ratio of CARS technique is better than that of SRS technique. Therefore, we chose the CARS technique was used in our subsequent studies of cluster formation in the free jet expansion.

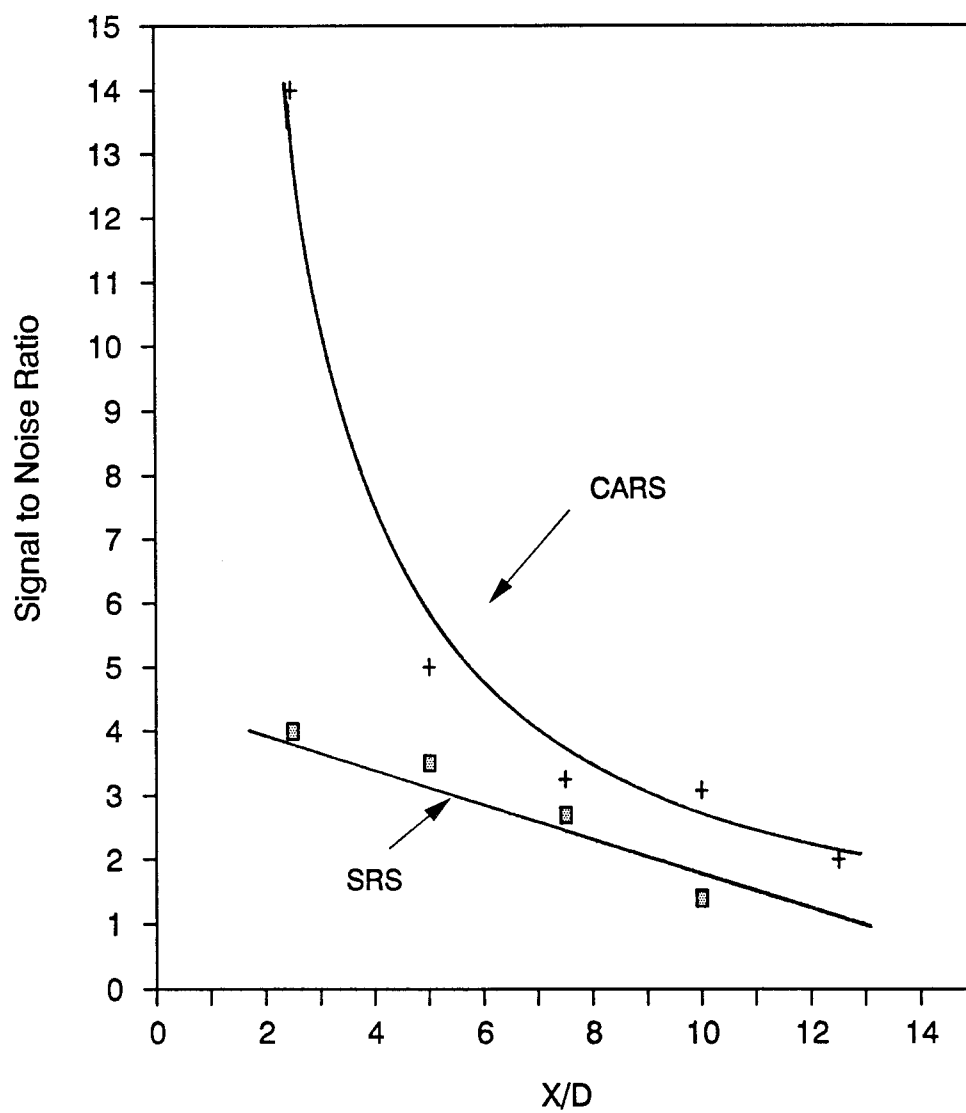


Figure 5.3. Comparison of the signal to noise of CARS and SRS.

Vibrational Raman Spectrum of Condensed Phases

Two structures of low pressure solid phases of N_2 are known. Figure 5.4a shows a crystal structure of β -nitrogen which is orientationally disordered. Open circles defining the cage structure denote hcp positions of the molecules. Only the central molecule is illustrated and all molecules precess about the c axis at an angle $\theta \cong 54.7^\circ$. This structure is stable between 63.1 K and 35.6 K. At lower temperatures a crystal structure is favored which is more highly ordered is shown in Figure 5.4b. The four molecules of the bases occupy half the corners of the small nested cube and it is stable below 35.6 K.

Figure 5.5 shows a series of SRS vibrational spectra taken by Rainer Beck⁷⁵ of equilibrium samples of bulk nitrogen in liquid and β and α solid phases. As one can see, liquid phase and solid phase transitions are easily produced at known temperatures simply by cooling. The frequency shift with temperature in the liquid and solid phases can be understood as the density of liquids and solids change with temperature.⁷⁵ High pressure Raman experiments⁷⁹ indicate that at densities higher than that at the triple point, the vibrational frequency will increase with density and at very high pressure it will reach beyond the gas frequency.

The interesting thing in these spectra is that the vibrational frequency of each phase shifted significantly and monotonically as the temperature changed. In the liquid region, the frequency shift was toward lower frequency as the temperature decreased. After the point

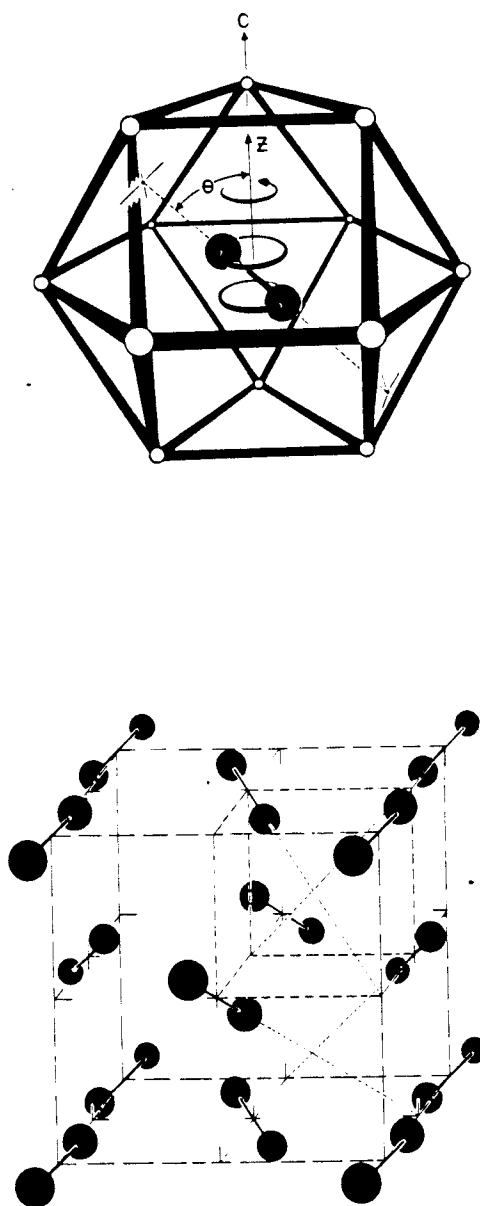


Figure 5.4. Crystal structures of solid nitrogen from ref 78.
Top: the β -solid. Bottom: the α -solid.

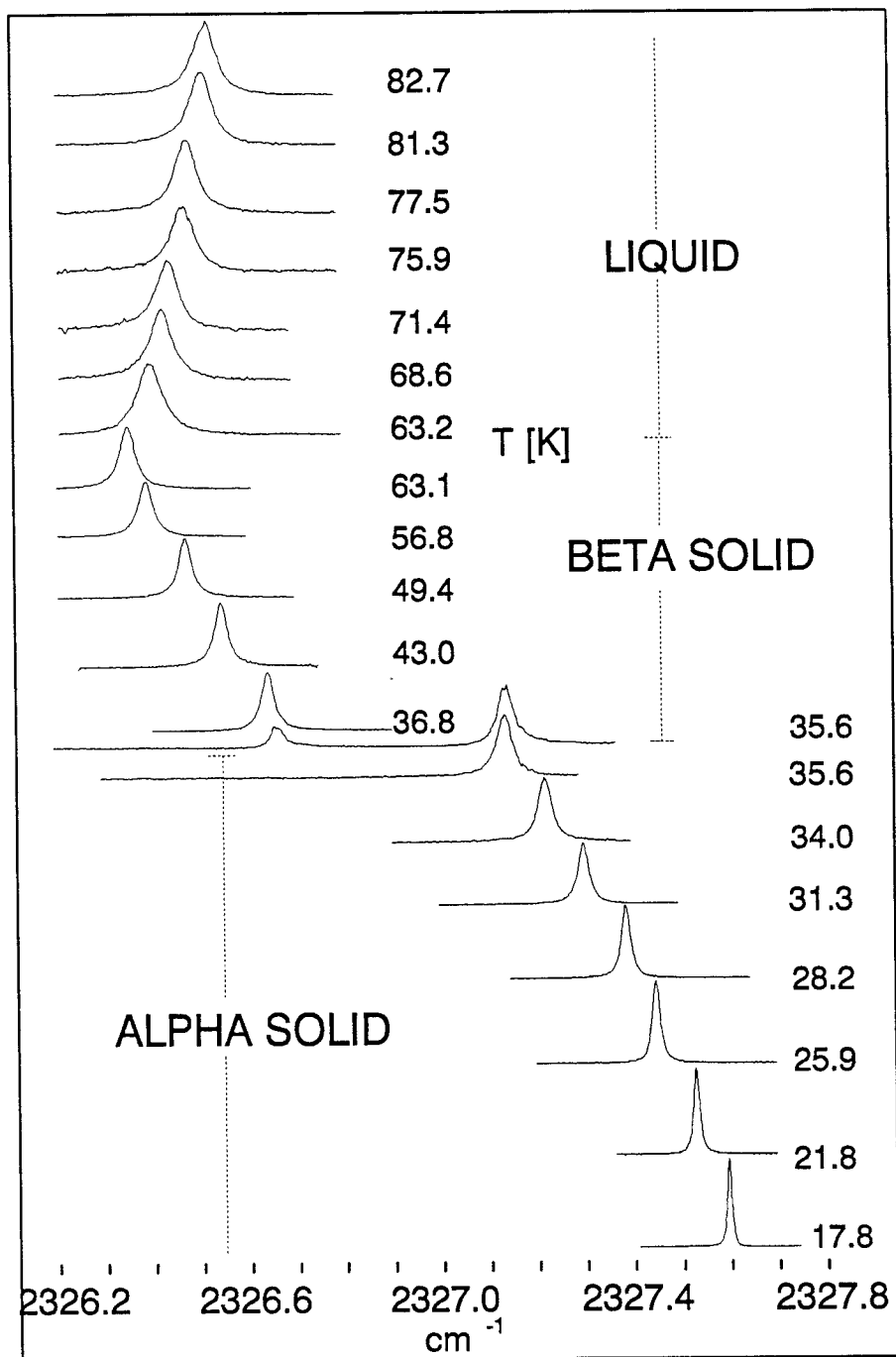


Figure 5.5. CW-SRS spectra of the internal vibration of nitrogen in the condensed phase from ref 75.

of the liquid to solid phase transition, the frequency turned around to higher value as the temperature was lowered. The frequency then increased suddenly when the point of the β -phase to α -phase transition was reached, a clear indication that molecular rearrangement had taken place. Finally, the vibrational frequency then shifted to still higher values as the temperature continued to decrease. For equilibrium samples, accurate frequency measurements can thus serve to measure temperature, a procedure we have used below in our treatment of the large clusters produced in our expansion.

Conditions for Forming Clusters in Jet Expansion

Unlike the equilibrium experiment in which the phase transition can be achieved by simply reducing the temperature of the sample, the conditions for forming clusters and for producing phase transitions during a nonequilibrium jet expansion are more difficult to obtain. Parameters such as nozzle diameter and shape, along with gas pressure and temperature, are the important variables in determining cluster formation and size in such expansions.

To search for suitable conditions to form clusters with a cone nozzle, a series of experiments were performed by fixing the nozzle temperature and stepping the driving pressure or fixing the driving pressure and stepping the nozzle temperature. The results of these experiments can be summarized as follows:

- (1) First, we note that, for strong CARS signals, high driving pressures are desirable to produce high sample densities.

However 600 psi was the maximum pressure at which our pulsed valve functioned properly. With the cone nozzle at 133 K and 600 psi one can see the formation of very large clusters which caused huge scattering easily visible to the eye. Under these conditions, the CARS signal was too noisy to give good spectra. However, when the nozzle temperature was raised to 135 K at the same pressure the huge scattering was gone and stable CARS signals were obtained. Therefore, nozzle temperature of 133K and a driving pressure of 600 psi define effective limits for forming suitable size clusters for coherent Raman probing.

- (2) At a pressure of 600 psi and higher nozzle temperature clusters were still detectable. However, at 173 K only liquid clusters could be seen near the nozzle tip and no phase transition of liquid to solid was observed. Weak scattering of laser beams was still visible near the nozzle. At higher temperature this scattering and all CARS signals for cluster disappeared.
- (3) From these studies, the best conditions for forming N_2 clusters in both liquid and solid phase with the cone nozzle were: Temperature between 153 to 160 K.

Pressure between 500 to 600 psi.

Phase Transitions in the Jet Expansion

Using the conditions determined in the last section, several

complete experiments were performed for neat nitrogen jet expansions from a 200 μm cone nozzle. The details of each phase transitions seen in such expansions will be discussed in the following sections.

The Vapor-Liquid Phase Transition

During the initial jet expansion of N_2 gas, the internal energy of the gas quickly transfers to kinetic energy and the vibrational and rotational temperatures rapidly drop. Many molecules collide with each other at this high density stage and some of them stick together to form clusters which are in liquid form. Figure 5.6 shows several scans that were taken at different distances from the nozzle.

The liquid cluster feature of N_2 at 2326.45 cm^{-1} appears to present already at the cone nozzle tip. The cluster peak then decreases in intensity as X/D increases. This indicates that the cone shape nozzle assists initial condensation inside of the cone nozzle, and only evaporation and collisional cooling take place after these clusters leave the nozzle. In contrast, the SRS studies of Beck with a channel nozzle showed continued cluster formation outside of the nozzle. Subsequent signal decrease is due to cluster density fall off as they travel downstream. Since these small clusters have a very big surface-to-volume ratio, they have a high vapor pressure and they tend to evaporate rapidly while traveling along the expansion axis. The evaporating molecules carry energy away from the liquid clusters and consequently they freeze at a certain point in the expansion.

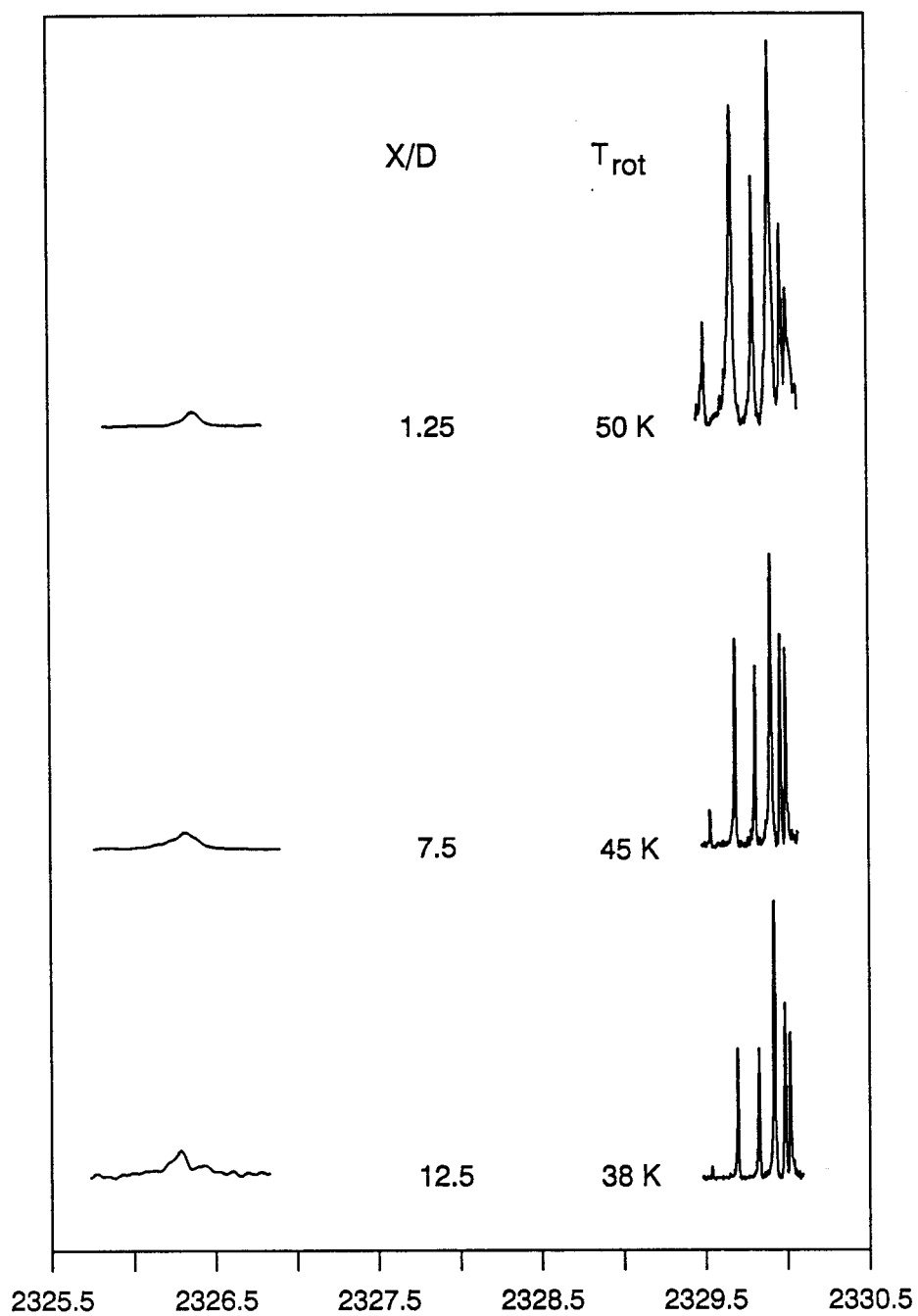


Figure 5.6. High resolution CARS spectra of nitrogen monomer Q-branch and cluster at different X/D values in the jet expansion.

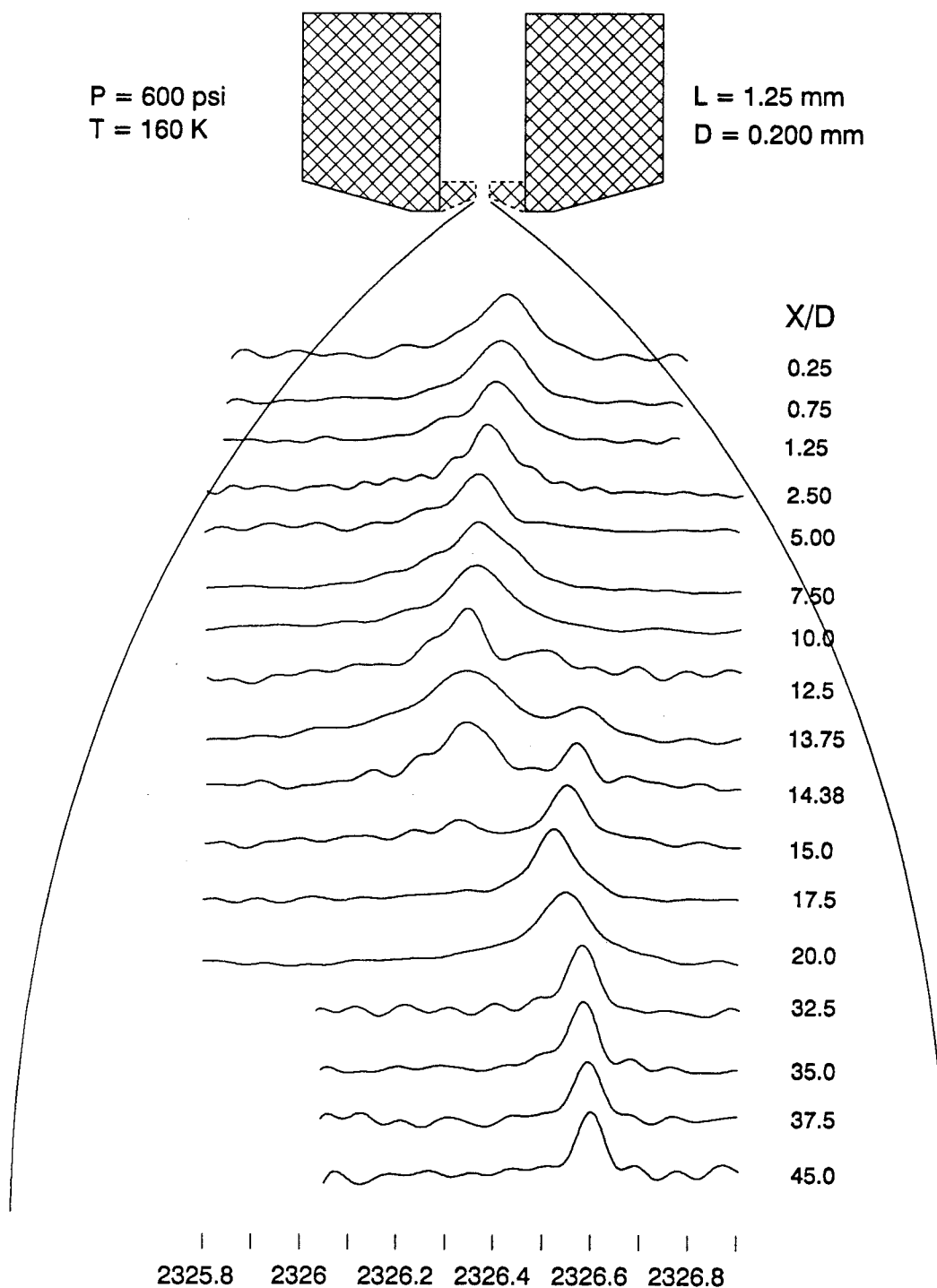


Figure 5.7. CARS spectra of the aggregate band at different points along the axis of expansion.

The Liquid-Solid Phase Transition

Eventually, the liquid will freeze at some point during the expansion because of evaporative cooling. For our experimental conditions of 600 psi pressure and 160 K in temperature, the liquid to solid phase transition occurred at $X/D \cong 12.5$, as shown in Figure 5.7. At the beginning of the freezing zone, a shoulder appears on the high frequency side of the liquid peak and this then gradually grows into a separate peak. Concurrently, the liquid peak starts to disappear. The frequency of the new peak is consistent with the assignment of the β -phase of solid nitrogen which, as mentioned earlier, is stable between 63.1 K to 35.6 K. The β -phase solid nitrogen peak can be detected out to $X/D \cong 100$ and no indication of a further transition to α -phase solid nitrogen was observed for the neat nitrogen jet expansions.

The α - β Phase Transition

The reasons for not seeing the β -phase to α -phase transition in our neat nitrogen jet experiments might be (1) too high a phase transition energy barrier, necessitating a supersaturated β -phase solid in order to have a phase transition; (2) insufficient cooling so that the internal temperature of β -phase solid cannot decrease below the point of the phase transition at 35.6 K.

For the first reason it might help to have some foreign molecules to serve as a nucleation center which can reduce the phase transition energy barrier. Based on this idea, an experiment was carried out

with 3% of CO_2 mixing with N_2 in a jet expansion. Figure 5.8 shows the spectra of the mixture which indicates that the foreign molecules do indeed help in the initial nucleation process. As one can see from the spectra β -solid has already formed at the beginning of the expansion and it then cools further as one moves out from the nozzle. However, the β -phase to α -phase transition was still not observable out to $X/D \approx 16$, at which point the S/N become poor. The N_2 probably does not need to cool down very much to form solid clusters because the CO_2 serves as a nucleation center for the N_2 . From the β -phase solid frequency, the temperature of these N_2 solid clusters was not very low (~ 39.5 K at $X/D \approx 16$). The transition from the β -phase to α -phase apparently requires greater supercooling for an appreciable rate during the ~ 5 μs of the expansion

Greater cooling in expansions can be achieved by using an atomic driving gas which does not have rotational and vibrational motions, only translational motion. Therefore, He can be used to assist the N_2 cooling during a jet expansion. A 50% mixture of He and N_2 was used in an experiment to see if α phase could be formed under those colder condition. Figure 5.9 shows the spectra obtained from the 50% N_2 in He expansion. They show the same initial phase transitions as for pure nitrogen expansions, but in a smaller range of X/D values. Comparing this with the spectra of equilibrium sample shown in Figure 5.5 one can see that the solid peak frequency measured here shifts further to the frequency between the β -solid and α -solid. This leads to the interpretation that the β -phase to α -phase transformation was slowly occurring but was not complete in the ~ 1 μs time necessary to travel

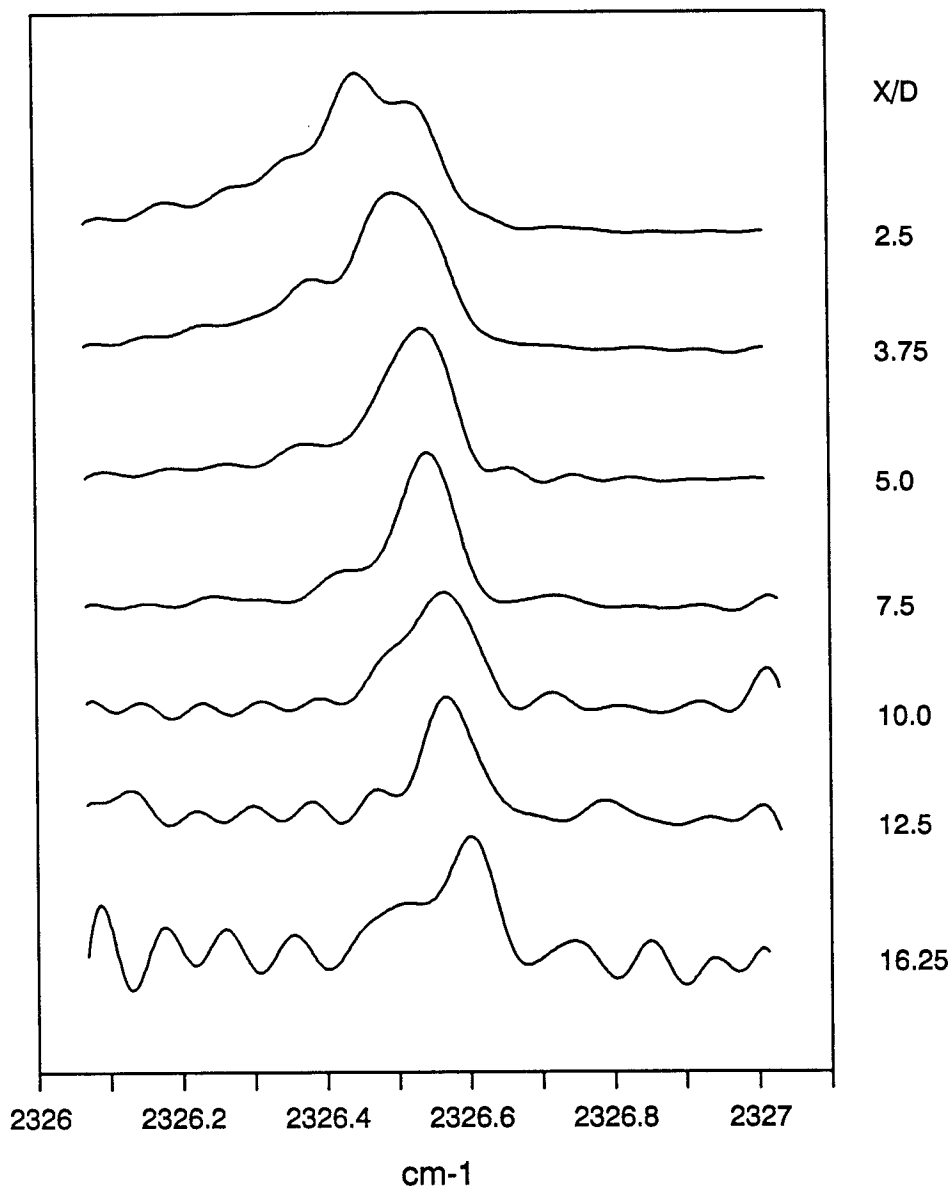


Figure 5.8. CARS spectra of the aggregate band at different points along the axis of an expansion of a mixture of N_2 (97%) and CO_2 (3%) expansion.

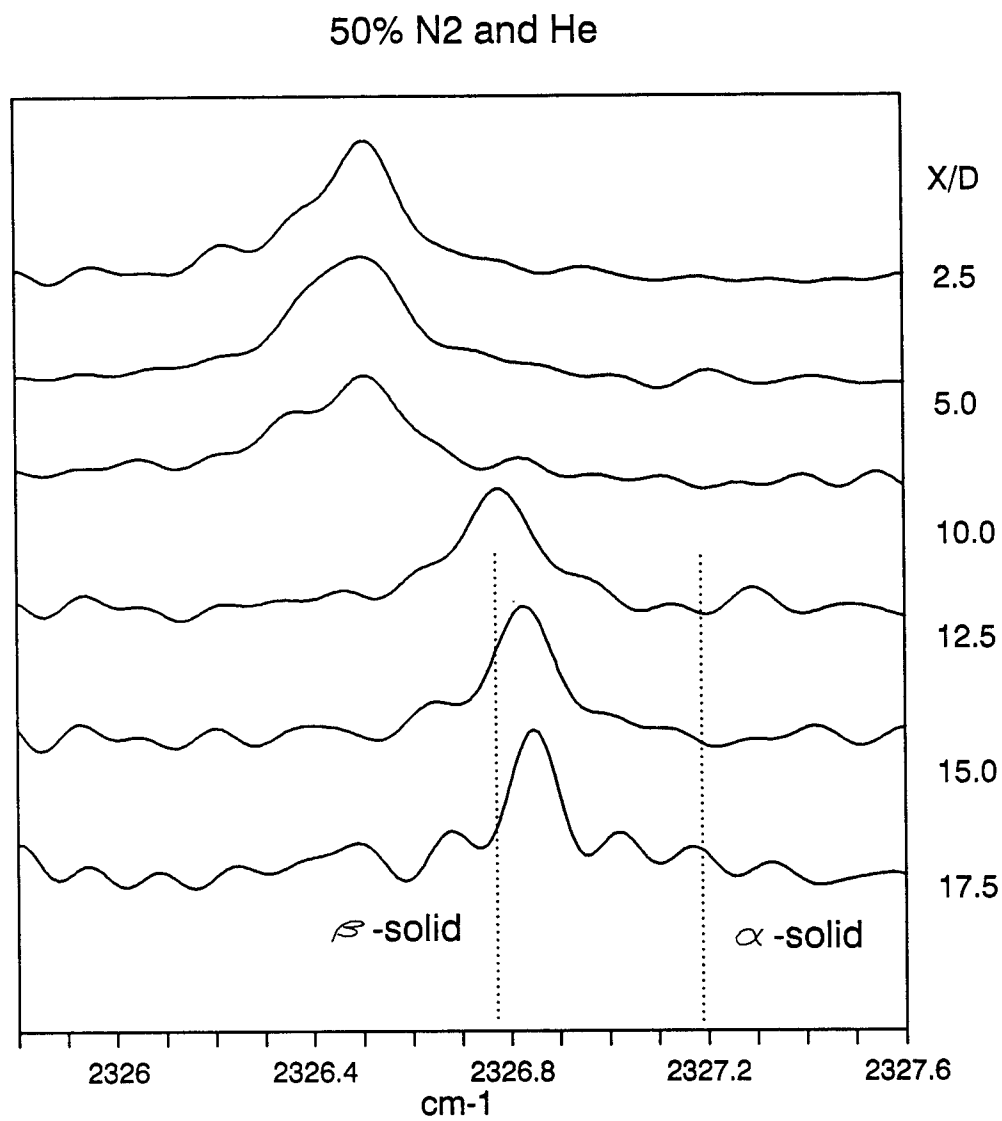


Figure 5.9. Aggregate spectra in Helium expansion containing 50% nitrogen.

from 12.5 to 17.5. Thus a clear α -phase solid peak was not seen (Figure 5.9). The disruptive transformation is going from β to α solid apparently takes longer time so that complete conversion to α from is hard to see in the jet.

Temperature of Liquid Aggregate

Assuming the clusters are large enough to have bulk properties, their internal temperatures can be calculated by using the Raman frequencies of the static liquid and solid nitrogen. A static sample of liquid N_2 would freeze at the triple point, 63.15 K. Comparing the frequency results from the CARS experiments with those from equilibrium SRS experiments,⁸¹ it is very interesting that the N_2 comes out from the cone nozzle already supercooled. This shows that the initial condensation and cooling takes place inside of the cone nozzle.

Unfortunately the temperature of the supercooled liquid N_2 droplets can not be determined directly from the vibrational frequency since there are no such equilibrium spectra available below 63.2 K. A linear extrapolation of the measured frequency-temperature curve to the region below 63.2 K was judged incorrect by R. Beck since the liquid temperature obtained from the linear extrapolation was higher than that of solid.⁷⁵ Also recent results of high pressure experiments of N_2 by Kroon⁷⁹ et al. and quadratic fitting of his high temperature data led Beck to predict a vibrational frequency turnaround (Figure 5.10) because of density increase as the temperature dropped.

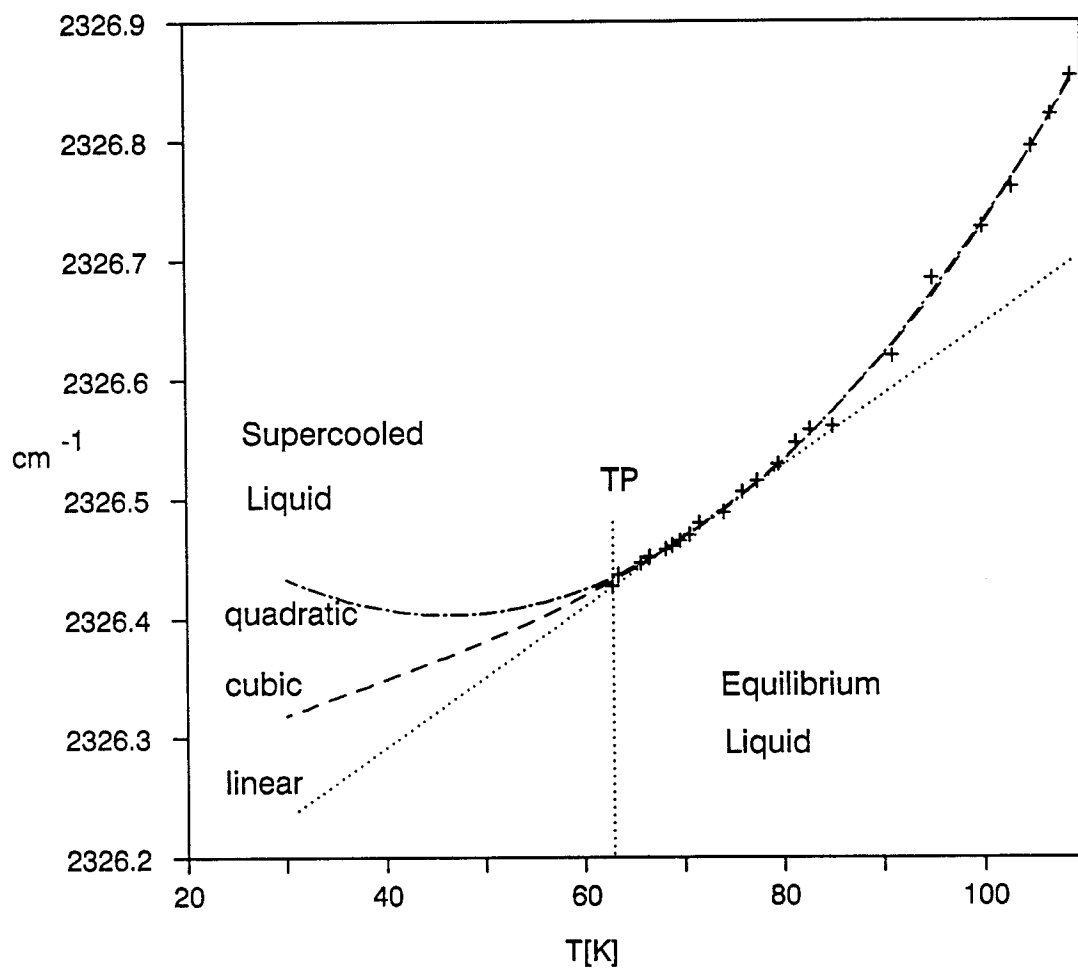


Figure 5.10. Three different extrapolation choices for obtaining supercooled liquid temperature.

This turnaround is not seen in his and my experimental results. From the form of the quadratic fit (Figure 5.10) Beck concluded that the frequency data would not give accurate temperatures of the supercooled drops.

However, in my work after considering the combination of liquid and solid temperatures seen for clusters, I have chosen a cubic functional form ($aX + bX^2 + cX^3 + d$) for the extrapolation of frequency vs temperature. A least squares fit of the high temperature data showed that the cubic parameters were well determined and significant. Figure 5.10 shows the three different extrapolation choices and the dashed line in the middle is the cubic extrapolation formula which was used to obtain the temperatures for the supercooled liquid. As discussed below the results deduced from the function are in reasonable agreement with an "isothermal" model of the freezing zone.

The Freezing Zone

The liquid to solid phase transition near $X/D \approx 10$ to 20 is the most interesting and complicated region in the spectra (Figure 5.11). Both liquid and solid N_2 exist in this zone, with complete conversion to solid occurring within 3 microseconds. One can observe that the frequency, and hence the temperature, of the liquid peak remains essentially constant in this liquid and β -solid phase coexistence region. The solid peak initially starts from a shoulder and gradually grows into a distinguishable peak on the high frequency side of liquid

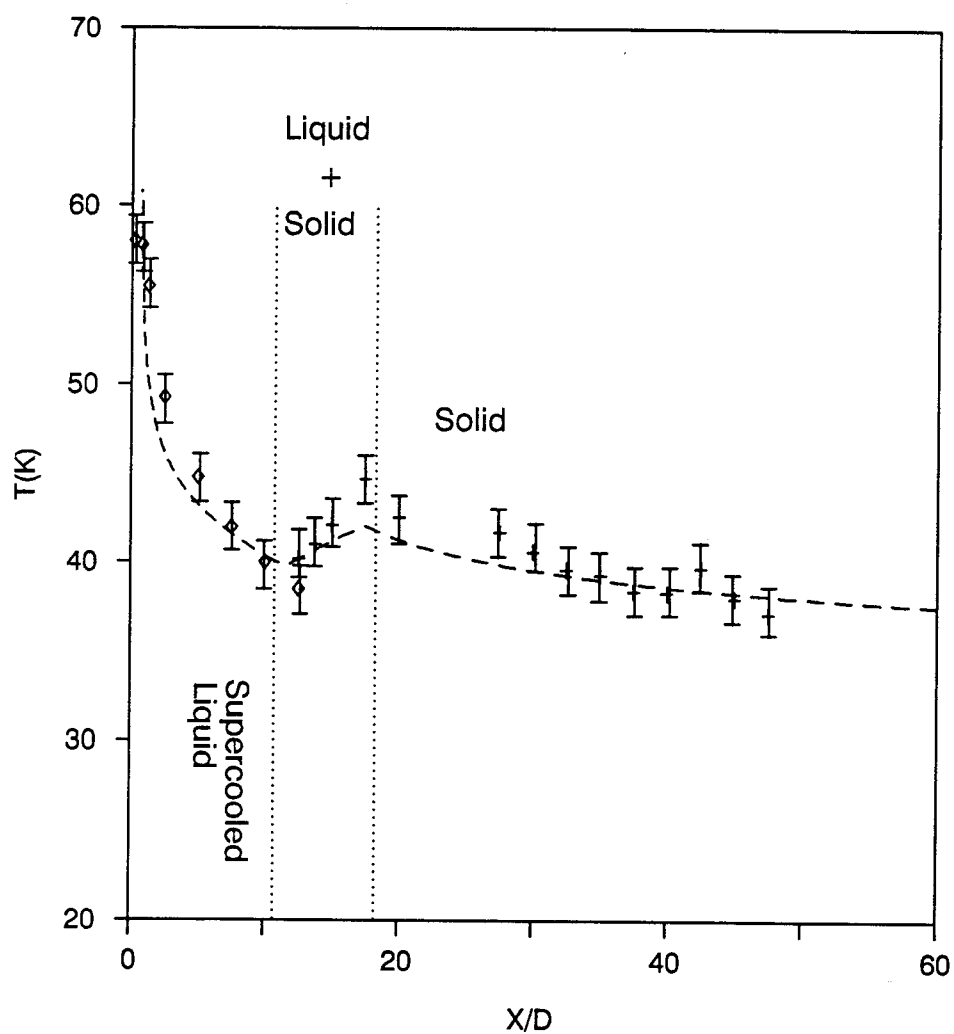


Figure 5.11. Supercooled liquid and β -solid temperatures in the free jet expansion and temperatures obtained from "isothermal" freezing model in dashed line.

peak. The first distinguishable solid peak appears at a relative high frequency and which then shifts to a lower frequency. After the liquid peak disappears the solid peak starts to shift toward higher frequency. This indicates that the solids warm up a little as the phase transition is in process and once the liquid has completely disappeared, the solid cools from 46 K to 36 K as it moves out in the expansion.

To explain this a gradual "isothermal" model of the freezing is introduced. We assume that the temperature of supercooled liquid N_2 is the same as that of the solid that first appears in the phase transition region and that both liquid and solid exist in the same droplet. Freezing then involves the gradual conversion of liquid to solid in a given droplet as it passes through the freezing zone between $X/D \approx 12.5$ and 15. The rate of freezing can be obtained from the areas of the liquid and solid peaks as a function of X/D position and in this way the fusion heat input for a drop for a given size can be estimated. This heating effect competes with the evaporative cooling of the outer surface of the spherical cluster which we assume to be β -phase solid. After all the liquid is frozen the cooling mechanism changes to pure evaporation of the solid. Using the gradual "isothermal" freezing model, a cooling curve covering the supercooled liquid, the liquid/solid coexistence region and the pure solid is computed. We assume a terminal cluster diameter of 33 nm as deduced in a later section. Overall this, admittedly simplistic, model shows good agreement with the experimental data for the solid and with the supercooled liquid temperature estimated from the cubic extrapolation

formula.

Rotational Temperature of the Monomer

The rotational temperature of the N_2 monomer was also deduced from the Q-branch intensity distribution and all the temperature data for all phase seen in the jet are shown in Figure 5.12. The monomer rotational temperatures overall are lower than the cluster internal temperature, which is expected because the energy released from condensation mostly heats up the liquid cluster. But, as one can see in Figure 5.12 the cooling rate of monomer is reduced in the region of liquid to β -solid transformation. This shows that the monomer is heated up by part of the heat of fusion released from phase transition. It is also likely that, at such small X/D (~ 12), there are substantial collisions between monomers and clusters and a close agreement of their temperatures might be expected. In contrast to this result for a cone nozzle, Beck found the freezing zone for a channel nozzle to be at much great X/D value (~ 30) where only evaporation effects should be important and the monomer was significantly colder than the clusters.

Cluster Size Estimate

The size distributions of the clusters formed in these jet expansion are of interest but difficult to obtain. Most optical scattering methods measure particle diameter ranging from few hundred to few thousand nm.^{90,91}

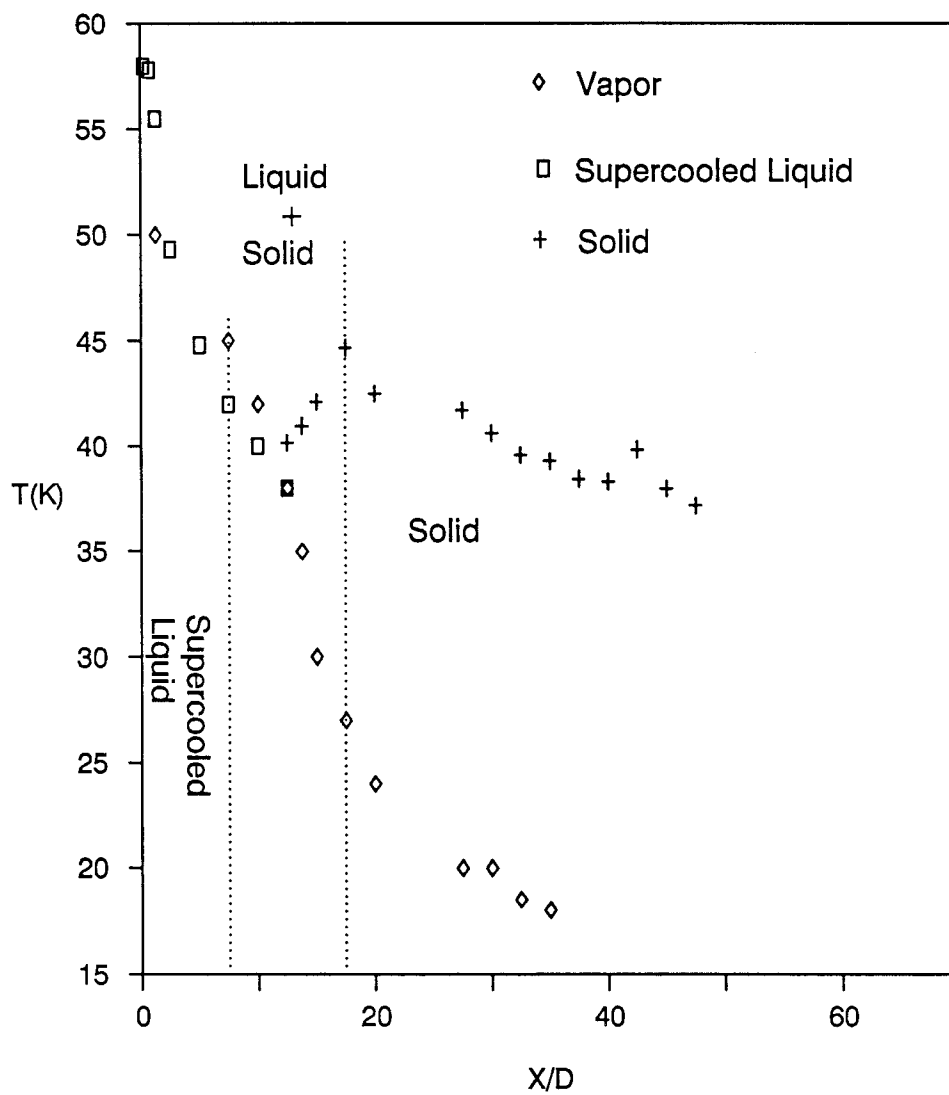


Figure 5.12. Temperatures of monomer, liquid, and solid in the free jet expansion.

A new method which we have developed in our laboratory is to estimate mean cluster size from measured cooling rates of the solid clusters. Far away from nozzle tip evaporation is considered to be the main cooling mechanism and the cooling rate can be calculated from the vapor pressure of solid and the surface area. Higher cooling rates occur for small clusters than for large ones since the surface-to-volume ratio for small clusters is large. By integrating in time for the flight along the axis of jet one obtains calculated cooling curves for various cluster diameters. From comparison with experimental data sets (Figure 5.13a and 5.13b) a mean diameter of 33 nm and crude cluster size range of 16-70 nm was deduced for the clusters formed in the cone nozzle.

The cone nozzle is expected to favor the formation of larger clusters. To achieve smaller clusters, while still keeping sample densities high, several experiments were done with the shim nozzle ($D = 200 \mu\text{m}$ and $L = 750 \mu\text{m}$). Clusters were seen have as well but with the freezing zone occurring at somewhat larger X/D values. As expected, modelling of slide cooling curves for two different experiments give a smaller mean diameter of 18 nm and a size range of about 9 to 50 nm as shown in Figure 5.14a and 5.14b. This mean size is significantly smaller than a values of 33 nm formed from cone nozzle and 35 nm formed from channel nozzle which was essentially a "thicker" shim nozzle of 2.5 mm thickness and 0.18 mm hole size.⁷⁵ This fourfold increase in channel length apparently favors the cooling and formation of larger clusters in the more directed expansion beam that results.

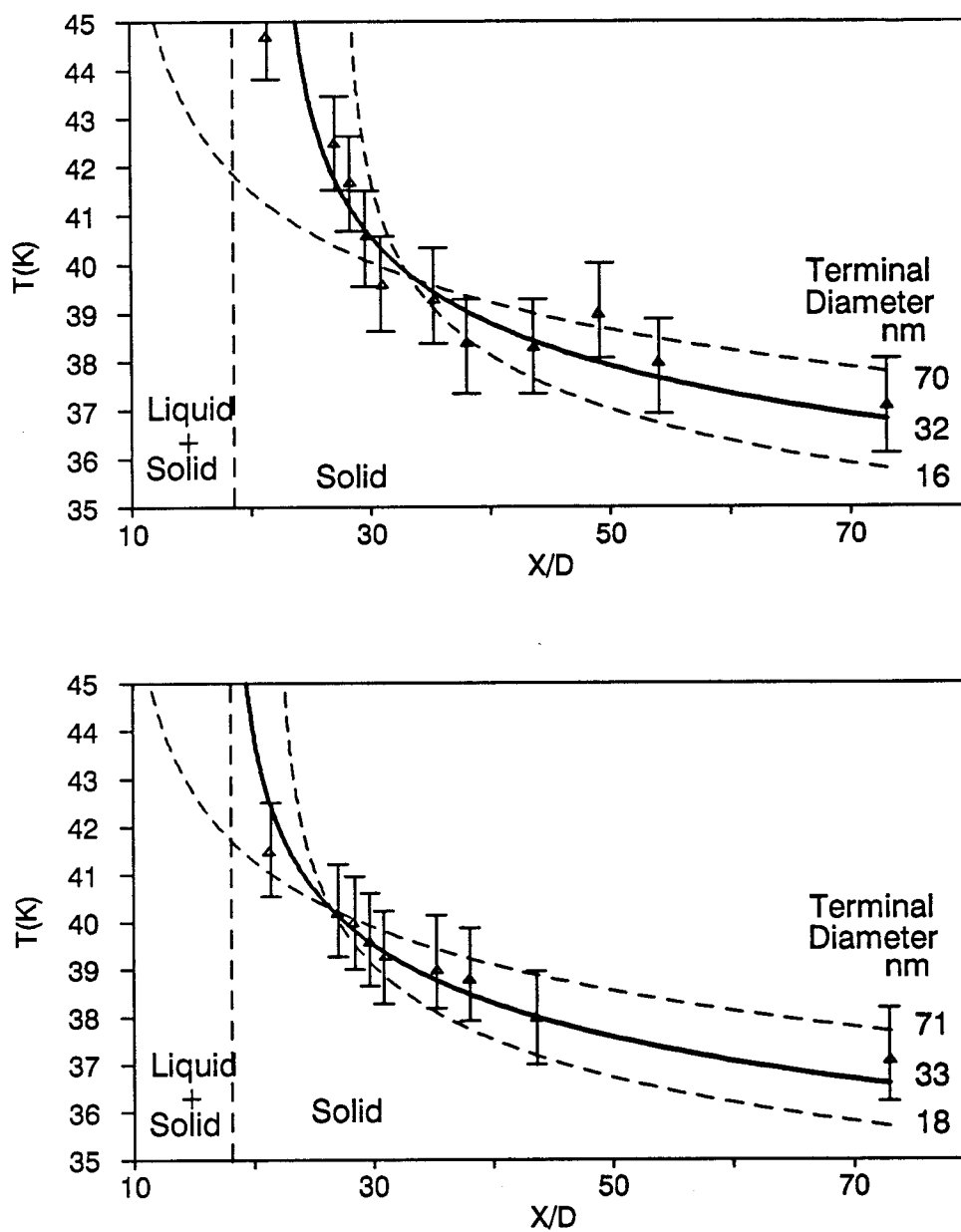


Figure 5.13. The cluster size estimation from cooling curves for two different cone nozzle experiments.

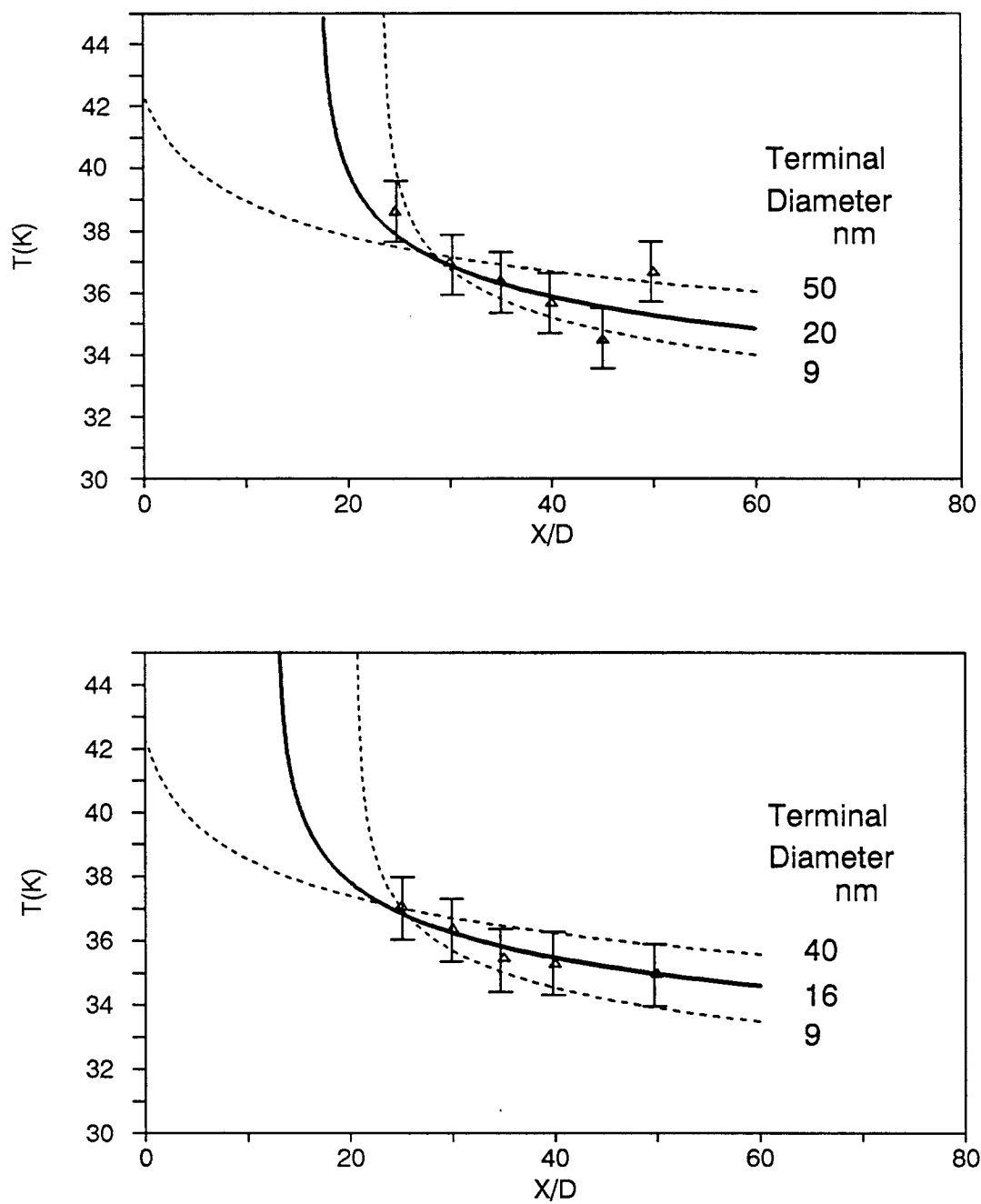


Figure 5.14. The cluster size estimation from cooling curves for two different shim nozzle experiments.

Surface Tension Effect on Cooling Curves

The vapor pressures of the above solid clusters used in the calculation of cooling curves is based on the assumption that these clusters can be treated as bulk solid. The accuracy of estimation of cluster size is critically dependent on this assumption and, therefore we examine the possible errors that the finite size of the particle may have in this section.

It is well-known⁸⁸ that the vapor pressure becomes size dependent for very small particles simply because of the curved surface. This results in an excess Laplace pressure of $2\gamma/r$, where γ is the surface tension of the material and r is its radius. The affect on the vapor pressure of a small particle is given by the Kelvin equation

$$\begin{aligned} P &= P_0 \exp [P_L V_m / RT] \\ &= P_0 \exp [2\gamma V_m / rRT] \end{aligned} \quad (5.2)$$

where P_∞ , P_L and V_m are vapor pressure for a flat surface, the Laplace pressure, and the molar volume, respectively.

It is widely believed that γ also depends upon drop size in a manner more or less as given by Tolman's relation^{82,83}

$$\gamma(r, T) = \gamma_\infty(T) / (1 + 2\delta/r) \quad (5.3)$$

where γ_∞ is the surface tension for a flat surface and δ is the

parameter which is of the order of 10^{-8} cm. Figure 5.15 shows a comparison of P/P_0 calculated for a liquid N_2 drop with the surface tension considered as a constant or as a function of cluster size. As one can see, the curves are nearly superimposeable and thus, in the following treatment the surface tension is considered to independent of the particle size.

It is also well known that the surface tension is a function of temperature, the general equation often used is the as following:^{88,89}

$$\gamma = E^s + T \, d\gamma/dT \quad (5.4)$$

where γ and E^s are the surface tension and the total surface energy respectively, and the slope $d\gamma/dT$ is negative value.

For most liquids the surface tension increases with decreasing temperature in a nearly linear fashion and the most widely used form, originated by van der Waals in 1894 but developed further by Guggenheim, is

$$\gamma = E^s (1 - T/T_c) \quad (5.5)$$

where the E^s is the total surface energy and the T_c is the critical temperature of the material. This equation also can be considered to apply to the solid region.⁸⁸

From equation (5.5) and equation (5.2), one can see that the effect on the vapor pressure will be the greatest for small, cold particles. This is shown in lower part of Figure 5.15 where several

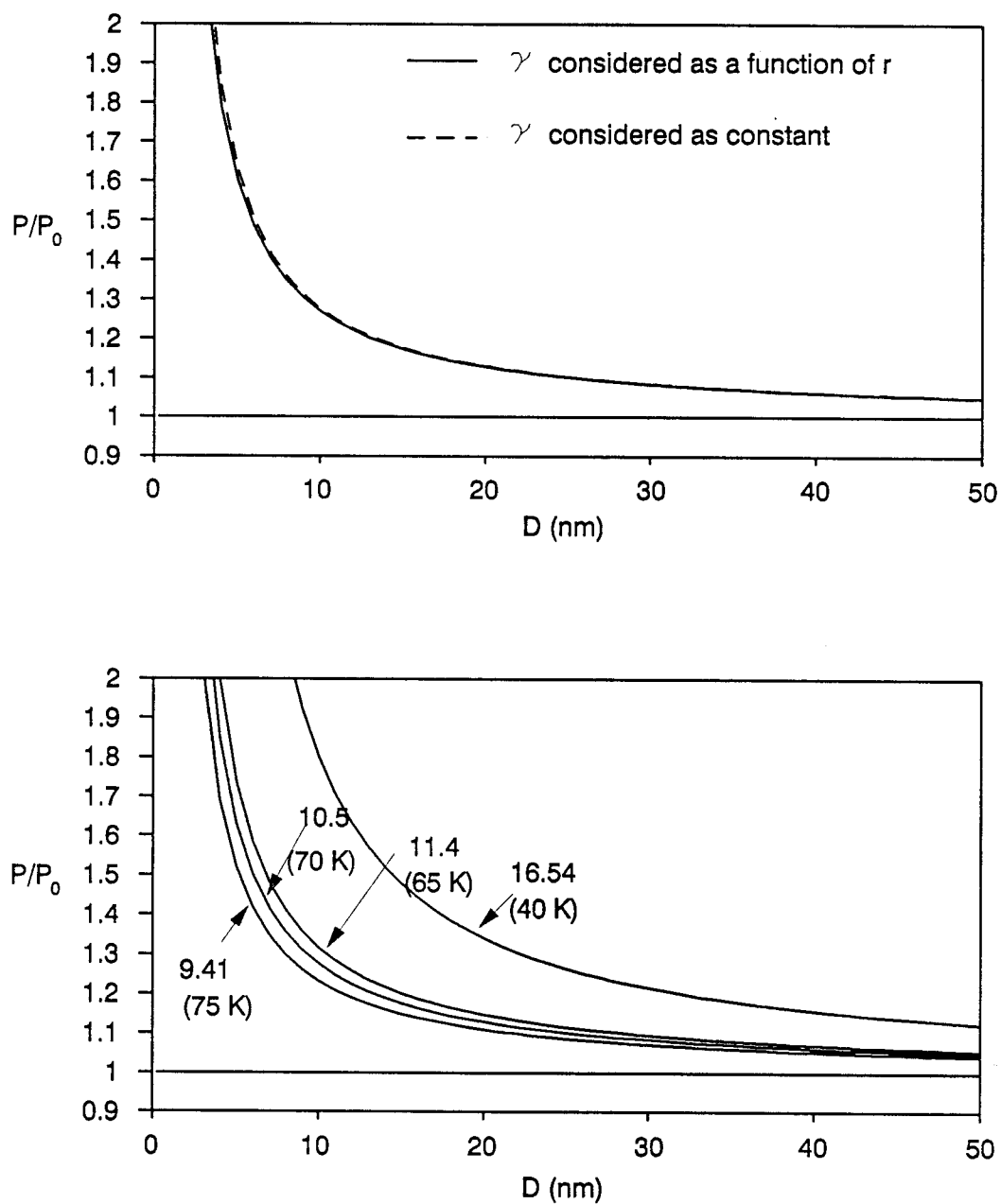


Figure 5.15. Calculated P/P_0 changes with the size of drop for nitrogen. Top: considering the surface tension as a function of cluster size. Bottom: for several different temperatures.

P/P_0 versus size curves are plotted for different $\gamma(T)$ values. This shows that a supercooled droplet of 10 nm diameter has nearly twice the vapor pressure of the equilibrium sample. This high value suggests that clusters of diameter less than 10 nm may not exist far away from nozzle since they evaporate so fast. For a solid cluster size around the 33 nm diameter seen in our cone nozzle experiment, a correction factor 1.2 might be deduced from the figure, if this is used to "correct" the vapor pressure in our model, the "best" mean cluster size is found to increase only slightly, to 38 nm. In obtaining this result equations (5.2) and (5.5) were used and the corrections were calculated in each X/D value in our model. A general comparison of the size estimated for model calculation with and without the surface correction is given in table 5.1.

Table 5.1. Comparison of size estimation by considering vapor pressure as a function of temperature only and as a function of temperature, surface tension and size of clusters.

	$P = f(T)$	$P = f(T, \gamma, r)$
Cluster size (nm)	7	26
	9	17
	16	24
	40	47
	50	57
	70	78

As one can see, the discrepancy becomes larger as the cluster size becomes smaller. The surface effect is especially dramatic when the cluster size is less than 9 nm, therefore the correction is defiantly

necessary for cluster in this size region.

SUMMARY

The results presented in this chapter indicate that the high resolution CARS technique is useful for studying the nucleation and subsequent freezing of microcluster formed by a free jet expansion. The spectra can provide frequency and internal temperature information on clusters, and serve to distinguish different phase in clusters. A comparison of high resolution CARS and SRS shows that the CARS technique has somewhat higher sensitivity than SRS in probing these clusters formed in free jet expansions.

The influence of a small amount of CO_2 used as a nucleation center in N_2 expansion was studied and it was found that instead of supercooled liquid, solid N_2 cluster were formed inside the nozzle. This CO_2 seed thus acts to overcome the high energy barrier in the pure nitrogen nucleation and freezing processes. No further transition from β to α phase N_2 solid was seen in this case nor in neat N_2 expansions but some partial conversion was seen under the more extreme cooling conditions produced by adding He as a driving gas.

The experimental results from a cone nozzle indicate that this shape is better in assisting cluster formation than is a shim or channel nozzle. The size distribution of those clusters is also found to be from 16 to 70 nm. For a thin shim nozzle, the cluster rang was 9 to 50 nm with a mean diameter of about 18 nm.

A simple gradual "isothermal" freezing model was successfully

used to describe the phase transition that takes place during the freezing process and overall the model fits the experimental results well. An extrapolation formula was deduced for supercooled liquid and the temperatures of supercooled liquid microdrops calculated from the formula are in good agreement with those of the gradual "isothermal" model.

The surface effect on the evaporative cooling of small clusters was also considered. It was found that the cluster size is less than 9 nm the surface effect must included in the model for calculating the right size of clusters.

REFERENCES

1. C. V. Raman and K. S. Krishnan, *Nature* **121**, 501 (1928).
2. R. S. Krishnan, in The Raman effect, Vol. 1, A. Anderson, ed (Marcel Dekker, New York, 1971)
3. D. A. Long, Raman Spectroscopy, McGraw-hill, New York, (1977).
4. G. Herzberg, Molecular Spectra and molecular Structure, Princeton, New Jersey (1945).
5. E. J. Woodbury and W. K. Ng, *proc. IRE* **50**, 2367 (1962).
6. R. W. Terhune, *Bull. Am. Phys. Soc.* **8**, 359 (1963).
7. R. W. Terhune and P. D. Maker, in Nonlinear Optics, Vol. 2, A. K. Levine, ed (Dekker, New York, 1968) p. 294.
8. J. A. Armstrong, N. Bloembergen, J. Ducuing, and P. S. Pershan, *Phys. Rev.*, **127**, 1918 (1962).
9. N. Bloembergen, Nonlinear Optics, Benjamin, New York, (1965).
10. P. D. Maker and R. W. Terhune, *Phys. Rev. A*, **137**, 801 (1965).
11. C. Flytzanis, in Quantum Electronics, Vol. 1, H. Rabin and C. L. Tang, ed (Academic, New York, 1975).
12. H. C. Anderson and B. S. Hudson, in Molecular Spectroscopy, Vol. 5, R. F. Barrow, D. A. Long and J. Sheridan ,ed (The Chemical Society, 1978).
13. P. N. Butcher, *Nonlinear Optical Phenomena*, Ohio State Univ. Engineering Publication, Columbus, (1965).
14. J. J. Valentini, in Spectrometric Techniques, Vol. 4, Ch. 1. (Academic Press, New York, 1985).
15. J. W. Nibler and G. V. Knighten, in "Raman Spectroscopy Gases and Liquids," Topic in Current Physics, Vol 11, A. Weber, ed (Springer-Verlag, Berlin and New York, 1979).
16. M. D. Levenson and J. J. Song, in "Coherent Raman Spectroscopy,"

- Topic in Current Physics, Vol 21, M. S. Feld, ed (Springer-Verlag, Berlin and New York, 1980).
17. J. W. Nibler and G. A. Pubanz, *ibid* Ch. 1.
 18. G. Placzek, *Handbuch der Radiologie*, Leipzig (1934).
 19. J. A. Gordmaine and W. Kaiser, *Phys. Rev*, **144**, 676 (1966).
 20. D. H. Levy, *Annu. Rev. Phys. Chem.* **31**, 197 (1980)
 21. H. Ashkenas and F. S. Sherman in Rarefied Gas Dynamics, J. H. de Leeuw, ed. Vol. II (Academic Press, New York, 1966).
 22. J. E. McDonald, *Amer. J. Phys.*, **30**, 870 (1962).
 23. J. E. McDonald, *Amer. J. Phys.*, **31**, 31 (1963).
 24. F. C. Wang in Condensation in High-Speed Flows, A. A. Pouring, ed (The American Society of Mechanical Engineers, New York 1977).
 25. F. Moya, S. A. J. Druet, and J. P. Taran, *Opt. Comm.* **13**, 169 (1975).
 26. A. C. Eckbreth and R. J. Hall, *Combustion and Flame* **36**, 87 (1975).
 27. G. L. Switzer, W. M. Roquemore, R. B. Bradley, P. W. Schreiber, and W. B. Roh, *Appl. Optics*, **18**, 2343 (1979).
 28. I. A. Stenhouse, D. R. Williams, D. R. Cole and M. D. Swords, *Appl. Optics* **18**, 3819 (1979).
 29. P. R. Regnier and J. P. Taran, *Appl. Phys. Lett.* **23**, 240 (1973).
 30. M. Pealat, J. P. Taran, J. Taillet, M. Bacal, and A. M. Buuneteau, *J. Appl. Phys.* **52**, 2687 (1981).
 31. W. M. Tolles, J. W. Nibler, J. R. McDonald and A. B. Harvey, *Appl. Spectrosc.* **31**, 253 (1977).
 32. J. J. Valentini, D. S. Moore and D. S. Bomse, *Chem. Phys. Lett.* **83**, 217 (1981).
 33. M. Pealat, D. Debarre, J. J. Marie, J. P. Taran, A. Tramer and

- C. B. Moore, Chem. Phys. Lett. **98**, 299 (1983).
34. A. C. Eckbreth and P. W. Schreiber, in Chemical Applications of Nonlinear Raman Spectroscopy, H. B. Harvey, ed (Academic Press 1981).
 35. J. A. Shirley, R. J. Hall, and A. C. Eckbreth, Opt. Lett. **5**, 380 1980
 36. Y. Prior, Appl. Opt. **19**, 1741 (1980).
 37. L. A. Carreira, R. Nelson, M. L. Horovitz, and L. Azarraga, Appl. Opt. **36**, 390 (1982).
 38. Y. K. Park, G. Giuliani and R. L. Byer, Opt. Lett. **5**, 96 (1980).
 39. Y. K. Park, G. Giuliani and R. L. Byer, IEEE J. Quantum Electron. **QE-20**, 117 (1984)
 40. L. A. Rahn, Applied Optics vol. 24, **7**, 940 (1985).
 41. P. Esherick and A. Owyong, Opt. Soc. **4**, 41 (1986).
 42. S. W. Henderson, E. H. Yuen and E. S. Fry, Opt. Soc. Vol. 11 **11**, 715 (1986).
 43. W. Koechner, Solid-State Laser Engineering, Springer-Verlag, New York, (1976).
 44. E. S. Fry, and S. W. Henderson, Appl. Opt. Lett. **5**, 96, (1986).
 45. F. H. Read, "Electromagnetic Radiation", (Chichester, New York Brisban, Toronto, 1980).
 46. M. Young, "Optics and Laser", (springer-verlag, New York, 1977).
 47. Users Manual of Model 6300 Injection Seeding System, Spectra-Physics, (1988).
 48. S. Gerstenkorn and P. Luc, Rev. Phys. Appl. **14**, 791 (1979).
 49. R. F. Coughlin and F. F. Driscoll, Operational Amplifiers and Linear Integrated Circuits, Englewood Cliffs, New Jersey, (1987).
 50. R. A. Gayakard, OP-AMPS and Linear Inregrated Circuits,

- Englewood Cliffs, New Jersey, (1988).
51. Jr. W. Weltner, Adv. High Tem. Chem. **2**, 85 (1969).
 52. J. W. Hastie, R. H. Hauge and J. L. Margrave, in Spectroscopy in Inorganic Chemistry, Vol 1, 58 (1970).
 53. A. Snelson, in Vibrational Spectroscopy of Trapped Species, Wiley, Ch 6, 203 (1973).
 54. W. Klempeper, J. Chem. Phys. **24**, 353 (1955).
 55. T. Tomita, C. E. Sjogren, P. Klaeboe, G. N. Papatheodorou and E. Rytter, J. Raman Spec. **14**, 415 (1983).
 56. P. Klaeboe, E. Rytter and C. E. Sjogren, J. Mol. Stru., **113**, 213 (1984).
 57. J. Martens, H. Uchtmann and F. Hensel, J. Phys. Chem. **91**, 2489 (1987).
 58. D. White, G. V. Calder and S. Hemple, J. Chem. Phys., **59**, 6645 (1973).
 59. D. M. Adams and D. J. Hills, J.C.S. Dalton, 776 (1978).
 60. L. Wharton, R.A. Berg and W. Klemperer, J. Chem. Phys. **39**, 2023 (1963).
 61. B. Lunelli and G. Cazzoli, J. Mol. Spec., **100**, 174 (1983).
 62. K. Wittel and R. Manne, J. Chem. Phys. **63** 1322 (1975).
 63. C. E. Sjogren and P. Klaeboe, Spectrochimica Acta, **40A**, 457 (1984).
 64. M. C. Drake and G. M. Rosenblatt, J. Chem. Phys., **65**, 4067 (1976).
 65. I. R. Beattie, T. R. Gilson and S. N. Jenny, Opt. Eng., **22**, 314 (1983).
 66. J. S. Ogden, in "Matrix Isolation Spectroscopy", A. J. Barnes ed., pp 207 - 230 (1981)

67. A. Givan and A. Loewenschuss, J. Chem. Phys. **65**, 1851 (1976).
68. C. L. Briant, and J. J. Burton, J. Chem. Phys. **63**, 2045 (1975).
69. T. L. Beck, J. Jellinek and R. S. Berry, J. Chem. Phys. **87**, 545 (1985).
70. E. Burgos and R. Righini, Chem. Phys. Lett., **96**, 584 (1983).
71. A. Anderson, P. J. Grout, J. W. Leech and T. S. Sun, Chem. Phys. Lett., **21**, 9 (1983).
72. N. C. Baenziger and W. L. Duax, J. Chem. Phys., **48**, 2974 (1968).
73. A. Givan, A. Loewenschuss, K. D. Bier and H. J. Jodl, J. Chem. Phys. **106**, 151 (1986).
74. A. W. Castleman Jr. and R. G. Keese, Chem. Rev. **86**, 589 (1986).
75. R. D. Beck, Ph.D. Thesis Oregon State University (1990).
76. G. A. Pubanz, Ph.D. Thesis Oregon State University (1987).
77. L. S. Bartell and T. S. Dibble, J. Am. Chem. Soc. **112**, 890 (1990).
78. T. A. Scott, Physics Reports **27**, 89 (1976).
79. R. Kroon, M. Gaggen and A. Lagendijk, J. Chem. Phys. **91**, 74 (1989).
80. R. Beck and J. W. Nibler, Chem. Phys. Lett. **148**, 271 (1988).
81. R. Beck, M. F. Hineman and J. W. Nibler, J. Chem. Phys. **92**, 7068 (1990).
82. R. C. Tolman, J. Chem. Phys. **17**, 333 (1949).
83. R. C. Tolman, J. Chem. Phys. **17**, 118 (1949).
84. O. Sinanoglu, J. Chem. Phys. **75**, 463 (1981).
85. M. Hooper and S. Nordholm, J. Chem. Phys. **81**, 2432 (1984).
86. J. G. Kirkwood and F. P. Buff, J. Chem. Phys. **17**, 338 (1949).

87. V. V. Sychev, A. A. Vasserman, A. D. Kozlov, G. A Spiridonov and V. A. Tsymarny, in Thermodynamic Properties of Nitrogen, Vol 2, National Standard Reference Data Service of the USSR.
88. A. W. Adamson, Physical Chemistry of Surface, 1967.
89. J. J. Bikerman, Surface Chemistry, 1958.
90. H. C. Van De Hulst, Light Scattering by Small Particles, 1957
91. I. J. Valha and D.J.Ryley, in Condensation in High-Speed Flows, A. A. Pouring, ed (The American Society of Mechanical Engineers, New York 1977).

APPENDICES

Appendix A: Data Collection Program for CARS Experiment

```

DECLARE SUB SHIFT (A%, SO!, d!, S1!, M!)
DECLARE SUB MCU3 (NP%, DI!, ES%)
DECLARE SUB AEROTCH (SS, R!)
DECLARE SUB ECHO (DYE0!, SHIFTO!, MONO!, order%)
DECLARE FUNCTION HILO! (X!, Y!)
DECLARE SUB SNDDATA (DATAOUT%)
DECLARE SUB COMMOUT (COMMAND%)
DECLARE FUNCTION CHKBUSY ()
DECLARE FUNCTION CHKIBF ()
DECLARE FUNCTION CHKOBF ()
DECLARE SUB PLOTROUTINE (NDPTS%, AERO0, AER1, steps, Sig0(), FILE$)
DIM Sig0(3000), X(3000), Sig1(3000)
COMMON /ADDRESSES/ PORT, DBA, DBB, DBC, AOUT, AIN

' *****
' *
' *      PROGRAM:      GRATE.BAS
' *
' *      A QUICK BASIC 4.5 PROGRAM TO COLLECT CARS/PARS
' *      SIGNALS. THE ROUTINE WILL STEP THE PDL-1 DYE
' *      LASER AND THE MCPHERSON VIA THE AEROTECH AND
' *      MCU -3 RESPECTIVELY.
' *
' *
' *      WRITTEN BY: MING YANG
' *      Jan. 1988
' *
' *****

' ----- PARAMETERS -----
SHIFT0 = 3372.8#
order% = 4
AERO% = 9999
APS = .0521
angperstep = .12 / order%
OMEG0 = 18788.415#
address = 1808

PORT = &H303
DBA = &H300
DBB = &H301
DBC = &H302
AOUT = &H89
AIN = &H99

RAMAX% = &HF0
RAMIN% = &H50
ACCDEC% = 500

```

```

ACCDECLO% = &HF4
ACCDECHI% = &H1
INIT% = &H26

```

```

INITPORT:
  OUT PORT, AOUT
  OUT DBB, &H1F

```

```

RESET:
  OUT DBB, &H17
  OUT DBB, &H1F

  go.time = TIMER + .5
  WHILE TIMER < go.time: WEND

```

```

COMMAND% = INIT%
CALL COMMOUT(COMMAND%)

```

```

DATAOUT% = RAMAX%
CALL SNDDATA(DATAOUT%)

```

```

DATAOUT% = RAMIN%
CALL SNDDATA(DATAOUT%)

```

```

DATAOUT% = ACCDECLO%
CALL SNDDATA(DATAOUT%)

```

```

DATAOUT% = ACCDECHI%
CALL SNDDATA(DATAOUT%)

```

```

menu:      , ----- MENU -----
  SCREEN 0, 0, 0
  CLS
  LOCATE 3, 20
  COLOR 0, 7
  PRINT "                MAIN MENU                "
  COLOR 7, 0
  PRINT
  LOCATE 8, 20
  PRINT "(1) Scan wavelength of McPherson"
  LOCATE 10, 20
  PRINT "(2) Slew to new position (AeroTech and McPherson)"
  LOCATE 12, 20
  PRINT "(3) Begin scanning"
  LOCATE 14, 20
  PRINT "(4) Plot data"
  LOCATE 16, 20
  PRINT "(5) Quit"

  LOCATE 6, 8: PRINT CHR$(201)                '218
  LOCATE 6, 72: PRINT CHR$(187)               '191

```

```

LOCATE 18, 8: PRINT CHR$(200)          '192
LOCATE 18, 72: PRINT CHR$(188)         '217
FOR I = 9 TO 71
    LOCATE 6, I: PRINT CHR$(205)        '196
    LOCATE 18, I: PRINT CHR$(205)       '196
NEXT I
FOR I = 7 TO 17
    LOCATE I, 8: PRINT CHR$(186): LOCATE I, 72: PRINT CHR$(186)  '179
NEXT I

```

```

' LINE (170, 245)-(530, 275), , B
LOCATE 20, 22
PRINT "Make your choice: #1-5          ",
COLOR 0, 7
LOCATE 20, 55: PRINT "  "
COLOR 7, 0
CHOICE$ = INPUT$(1)
CHOICE% = VAL(CHOICE$)

```

```

CLS
SELECT CASE CHOICE%

```

```

' ----- CASE 1 -----

```

```

CASE 1
GETLAM:
INPUT "DO YOU WANT ROUGH SLEW OR FINE SLEW (R or F)? ", SL$
IF SL$ = "R" THEN GOTO 40 ELSE GOTO 50
40 :
PRINT "CURRENT WAVELENGTH IS:          ", LAMDAO
INPUT "IS THIS CORRECT          ", ans$
IF ans$ = "Y" OR ans$ = "y" THEN
    INPUT "ENTER FINAL WAVELENGTH:          ", LAMDA1
    IF LAMDA1 = LAMDAO THEN 30
    NPLUS% = ABS(INT((LAMDA1 - LAMDAO) / .0521))
    DIR = HILO(LAMDAO, LAMDA1)
    ESTP% = 18
    CALL MCU3(NPLUS%, DIR, ESTP%)
ELSEIF ans$ <> "N" OR ans$ <> "n" THEN
    INPUT "ENTER CURRENT WAVELENGTH          ", LAMDAO
    GOTO 40
END IF

```

```

' -----

```

```

30 :
PRINT :
INPUT "DO YOU WANT TO SLEW THE MC. IN FINE INC.: ", AB$
IF AB$ = "Y" OR AB$ = "y" THEN
50 :
ESP% = 1
INPUT "GO UP or GO DOWN (0 or 1) ", DIR

```

```

10 :
  INPUT "ENTER THE STEPS  [99 = Return]", DUM%
  IF DUM% = 99 THEN GOTO 20
  IF DUM% < 0 THEN GOTO 50
  IF DUM% <> 0 THEN M% = DUM%
  CALL MCU3(M%, DIR, ESP%)
  GOTO 10
20 :
  END IF

```

GOTO menu

' ----- CASE 2 -----

CASE 2

SLE:

INPUT "ENTER CURRENT AEROTECH POSITION----->", AERO%

' ----- CALCULATE DYELASER AND MONOCHROMATOR POSITION-----

CALL SHIFT(AERO%, SHIFTO, DYE0, SHIFT1, MON0)

INPUT "ENTER NEW AEROTCH POSITION ----->", AER1%

CALL SHIFT(AER1%, SHIFTO, DYE1, SHIFT2, MON1)

PRINT : PRINT

PRINT "SLEW AEROTCH FROM ", AERO%, "TO", AER1%

PRINT "CORRESPONDING RAMAN SHIFT ", SHIFT1; "TO", SHIFT2

AER1 = AER1%: AERO = AERO%

INPUT "CHANGE ANYTHING ", ans\$

IF ans\$ = "Y" OR ans\$ = "y" THEN

AERO% = 9999

GOTO SLE

END IF

IF AER1% = AERO% THEN

GOTO menu

ELSE

AERSTEP = ABS(AER1 - AERO)

DIRO = HILO(AER1, AERO)

CALL AEROTCH(AERSTEP, DIRO)

DIRM = HILO(MON0, MON1)

npulsmon% = ABS(INT((MON1 - MON0) / APS))

ES% = 18

IF MON0 < MON1 THEN npulsmon% = npulsmon% + 500

CALL MCU3(npulsmon%, DIRM, ES%)

IF MON0 > MON1 GOTO skip

NPU% = 500

DIRM = HILO(MON1, MON0)

CALL MCU3(NPU%, DIRM, ES%)


```

skip:      DYE0 = DYE1
          SHIFT1 = SHIFT2
          MON0 = MON1
          AERO% = AER1%
          CALL ECHO(DYE0, SHIFTO, MON0, ORDER%)
          END IF
          GOTO menu

' ----- CASE 3 -----

CASE 3

' ----- SCANNING PART -----

OPSC:
  INPUT "ENTER THE INITIAL AEROTECH POSITION----->", AERO%
  INPUT "ENTER THE FINAL AEROTECH POSITION----->", AER1%
  INPUT "ENTER # OF STEPS /POINT (1,2,3..) ", steps%
  AERO0% = AERO%
  steps = steps%
  NDPTS% = (AER1% - AERO%) / steps% + 1
  IF NDPTS% > 4000 OR NDPTS% < 0 THEN
    PRINT "DATA POINTS OUT OF RANGE, TRY AGAIN"
    GOTO OPSC:
  END IF
  INPUT "ENTER THE NUMBER OF SHOTS TO AVERAGE ", SHOTS%
  INPUT "DO YOU WANT TO COLLECT DATA ON CH1 TOO? "; ans$
  IF ans$ = "Y" OR ans$ = "y" THEN ATOD% = 2
  IF ans$ = "N" OR ans$ = "n" THEN ATOD% = 1
  PRINT : PRINT "SCANNING FROM ", AERO%, "TO", AER1%
  CALL SHIFT(AERO%, SHIFTO, DYE0, SHIFT1, MON0)
  CALL SHIFT(AER1%, SHIFTO, DYE1, SHIFT2, MON1)
  PRINT "CORRESPONDING RAMAN SHIFT: ", SHIFT1, "TO", SHIFT2
  PRINT "CORRESPONDING MCPHERSON : ", MON0, "TO", MON1
  IF ATOD% = 1 THEN
    PRINT " COLECTING DATA ON CH 0 ONLY"
  ELSEIF ATOD% = 2 THEN
    PRINT "COLLECTING DATA ON CH 0 AND CH 1"
  END IF
  AER1 = AER1%: AERO = AERO%
  DIR = HILO(AER1, AERO)
  DIRM2 = HILO(MON0, MON1)
  PRINT
  INPUT "CHANGE ANYTHING? "; ans$
  IF ans$ = "Y" OR ans$ = "y" THEN
    AERO% = 9999
    GOTO OPSC
  END IF
  PRINT "PAUSE-----<CR> TO SCANNING"
  WHILE INKEY$ = "RETURN": WEND
' WRITE BYTE TO BOARD: ENABLE EXTERNAL START CONVERSION
  X = INP(address + 6)

```

```

OUT address + 4, 128
OUT address + 4, 132
OUT address + 5, 0          ' WRITE CHANNEL 0 TO THE BOARD

' -----
CLS
SCREEN 3
VIEW (1, 1)-(680, 298), , 1
WINDOW (1, 0)-(NDPTS%, 10)
VIEW PRINT 24 TO 25
IF ATOD% = 2 THEN
    LINE (1, 8)-(NDPTS%, 8)
END IF
LOCATE 24, 5: PRINT "RAMAN SHIFT:"
LOCATE 24, 48: PRINT "INTENSITY:"
MOP2 = ABS(MONO - MON1) / (NDPTS% * APS)
MOP1 = 0
FOR I = 1 TO NDPTS%
    SUM0 = 0
    SUM1 = 0
    FOR j = 1 TO SHOTS%
' =====
'
' IF TWO A/D'S ARE TAKEN RESTORE ADDRESS FOR A/D ON CH 0
'
' =====
        IF ATOD% = 2 THEN
            OUT (address + 4), 132          'A/D EXTERNAL START
            OUT (address + 5), 0           'ON CHANNEL 0

        END IF

100 :      IF INP(address + 4) < 128 THEN 100 'END CONVERSION?
            LO = INP(address + 5) AND 255
            HI = INP(address + 6) AND 15
            TOT = 256 * HI + LO
            IF TOT > 32767 THEN TOT = TOT - 65536
            DUM0 = TOT / 409.6
            SUM0 = SUM0 + DUM0
            IF ATOD% = 1 THEN 300          'SECOND A/D?
                OUT (address + 4), 128
                OUT (address + 5), 1       'A/D ON CH 1
                OUT (address + 6), 0       'START CONVERSION

200 :      IF INP(address + 4) < 128 THEN 200
            LO = INP(address + 5) AND 255
            HI = INP(address + 6) AND 15
            TOT = 256 * HI + LO
            IF TOT > 32767 THEN TOT = TOT - 65536
            DUM1 = TOT / 409.6
            SUM1 = SUM1 + DUM1

300 :

```

```

Sig0(I) = SUM0 / SHOTS%
Sig1(I) = SUM1 / SHOTS%
NEXT j

```

'-----PLOT THE DATA -----'

```

IF I = 1 THEN 700
IF ATOD% = 1 THEN
    LINE (I - 1, Sig0(I - 1))-(I, Sig0(I))
END IF
IF ATOD% = 2 THEN
    PRESET (I - 1, Sig0(I - 1) * .8)
    LINE (I - 1, Sig0(I - 1) * .8)-(I, Sig0(I) * .8)
    PRESET (I - 1, Sig1(I - 1) * .2 + 8)
    LINE (I - 1, Sig1(I - 1) * .2 + 8)-(I, Sig1(I) * .2 + 8)
END IF
700 :
    IF I = 1 THEN SHIFT2 = SHIFT1
    LOCATE 24, 20: PRINT USING "####.##"; SHIFT2
    AER00% = AER00% + steps
    LOCATE 24, 58: PRINT USING "##.###"; Sig0(I)
    CALL AEROTCH(steps, DIR)
    CALL SHIFT(AER00%, SHIFT0, d, SHIFT2, MON1)
    X(I) = SHIFT2
    ES% = 0
500 :
    DUM = (MON0 - MON1) / APS
REM=====
REM    DUM = NPULSES TO McPHERSON, IF LESS THAN 1, WAIT TIL
REM    NEXT TIME THRU. NPULS%= 0 WILL STEP McPHERSON 1 STEP,
REM    NPULS%= 1 WILL STEP 2 ETC. SO WE NEED TO SUBTRACT 1
REM    FROM THE CALCUALTED NUMBER OF PULSES.
REM=====
    IF DUM < 1 THEN 600
    NP% = INT(DUM - 1)
    CALL MCU3(NP%, DIRM2, ES%)
    MON0 = MON0 - (NP% + 1) * APS
600 :
    NEXT I

1000 :
    INPUT "DO YOU WANT TO SAVE DATA TO DISK ? ", SA$
    IF SA$ = "Y" OR SA$ = "y" THEN 1200 ELSE 1100
1100 :
    IF SA$ = "N" OR SA$ = "n" THEN 1900 ELSE 1000
1200 :
    INPUT "WHICH DRIVE (A: B: OR C:) ", WW$
    IF WW$ = "a" OR WW$ = "A" THEN WW$ = "A:"
    IF WW$ = "b" OR WW$ = "B" THEN WW$ = "B:"
    IF WW$ = "c" OR WW$ = "C" THEN WW$ = "C:"

```

```

INPUT " FILE NAME ", FILE$
OPEN WW$ + FILE$ FOR OUTPUT AS #1
PRINT #1, AERO%, AER1%
PRINT #1, steps%, SHOTS%
PRINT #1, SHIFTO, ATOD%
IF ATOD% = 1 THEN
FOR N = 1 TO NDPTS%
    PRINT #1, X(N), Sig0(N)
NEXT N
ELSEIF ATOD% = 2 THEN
FOR N = 1 TO NDPTS%
    PRINT #1, X(N), Sig0(N), Sig1(N)
NEXT N
END IF

CLOSE #1
1900 :
    WHILE INKEY$ <> "": WEND
    SCREEN 0
    GOTO menu
REM =====
CASE 4
CALL PLOTROUTINE(NDPTS%, AERO, AER1, steps, Sig0(), FILE$)
GOTO menu

Handler:
    Number = ERR
    IF Number = 53 THEN
        CLOSE #2
        PRINT "File Not Found"
        PRINT "Press <RETURN> to resume program"
    END IF
    ans$ = INPUT$(1)
    RESUME redo: GOTO menu
redo:
    GOTO menu

CASE 5
END SELECT
END

SUB AEROTCH (SS, R)                                ' CONTROL port address

PORT = 1823
OUT PORT, &H80
IF R = 1 THEN
    OUT PORT - 1, 255
ELSEIF R = 0 THEN
    OUT PORT - 1, 0
END IF

```

```

FOR I = 1 TO SS - 1
  FOR j = 1 TO 5
    OUT PORT - 3, 255
  NEXT j
  FOR j = 1 TO 5
    OUT PORT - 3, 0
  NEXT j
NEXT I
OUT PORT - 3, 255

END SUB

FUNCTION CHKBUSY

  SHARED PORT, DBA, DBB, DBC, AOUT, AIN

  OUT DBB, &H7F                                     ' POLL FOR BUSY = 0
  CHKBUSY = 1
POLL2:
  OUT DBB, &H7C                                     ' 1100=READ STATUS
  STATUS% = INP(DBC)                                ' READ STATUS
  OUT DBB, &H7E
  IF (STATUS% AND 4) = 0 THEN
    GOTO OVERANDOUT
  ELSE
    GOTO POLL2
  END IF
OVERANDOUT:
  OUT DBB, &H1F
  END FUNCTION

FUNCTION CHKIBF

  SHARED PORT, DBA, DBB, DBC, AOUT, AIN

  OUT DBB, &H7F                                     ' POLL FOR IBF = 0
  CHKIBF = 1
POLL1:
  OUT DBB, &H7C                                     ' 1100=READ STATUS
  STATUS% = INP(DBC)                                ' READ STATUS
  OUT DBB, &H7E
  IF (STATUS% AND 2) = 0 THEN
    GOTO DONE
  ELSE
    GOTO POLL1
  END IF
DONE:
  OUT DBB, &H1F
  END FUNCTION

FUNCTION CHKOBF

```

```

    SHARED PORT, DBA, DBB, DBC, AOUT, AIN
                                ' SHARED PORT, DBA, AIN, DBRB

    OUT PORT, AIN                ' SET PORT A FOR INPUT

    CHKOBF = 1                    ' POLL FOR BUSY = 0
POLL:
    OUT DBB, &HF
    OUT DBB, &HC                  ' 1100=READ STATUS
    OUT DBB, &HE                  ' READ STATUS
    STATUS% = INP(DBA)
    IF (STATUS% AND 1) = 0 THEN CHKOBF = 0
    IF CHKOBF <> 0 THEN GOTO POLL

    END FUNCTION

    SUB COMMOUT (COMMAND%) STATIC

    SHARED PORT, AOUT, DBA, DBB

    BUSY = CHKBUSY
    OUT DBA, COMMAND%             ' PUT DATA IN A
    OUT DBB, &H1A                 ' 1010=WRITE COMMAND
    OUT DBB, &H1E                 ' TOGGLE WRITE
    END SUB

    SUB ECHO (DYE0, SHIFTO, MON0, order%)

    PRINT "                        "
    PRINT "CURRENT SETTING ARE:"
    PRINT "MONOCHROMATOR: "; MON0
    PRINT "DYELASER: "; DYE0; "    DYELASER READING ", order% * DYE0
    PRINT "THESE CORRESPOND TO A SHIFT OF "; SHIFTO

    END SUB

    FUNCTION HILO (X, Y)

    IF X > Y THEN
        HILO = 1
    ELSEIF X < Y THEN
        HILO = 0
    END IF

    END FUNCTION

    SUB MCU3 (NP%, DI, ES%)

    ,
    MCU-3 INTERFACE VIA METRABYTE PIO12 24BIT PARALLEL INTERFACE

    CONSPEED:

```

```

IF DI = 0 THEN
  COMMAND% = &H44
ELSEIF DI = 1 THEN
  COMMAND% = &H4C
END IF
  RATE% = 255
  PULSELO% = NP% MOD 255
  PULSEHI% = (NP% - PULSELO%) / 255
  IF PULSEHI% < 0 THEN PULSEHI% = 0
  CALL COMMOUT(COMMAND%)
  DATAOUT% = RATE%
  CALL SNDDATA(DATAOUT%)
  DATAOUT% = PULSELO%
  CALL SNDDATA(DATAOUT%)
  DATAOUT% = PULSEHI%
  CALL SNDDATA(DATAOUT%)
  DATAOUT% = 0
  CALL SNDDATA(DATAOUT%)
END SUB

```

```

SUB PLOTROUTINE (NDPTS%, AERO, AER1, steps, sig(), FILE$)
DIM SIGX(3000)
DEFINT A-H
SCREEN 0, 0, 0
CLS

```

```

GOSUB OUTPUT.TYPE
GOSUB GET.DAT
GOSUB X.Y.TICK
GOSUB LABLES
GOSUB PLOT.DAT
GOSUB TITLES
GOSUB CHOICE.PARAMETERS
PRINT #1, "sp;pu-30 0;"
CLOSE #1
LJP$ = "L"
GOSUB PRINT.MESSAGE
EXIT SUB

```

OUTPUT.TYPE:

```

again1:
LOCATE 10, 10: PRINT "Would you like to plot this on the HP7470A"
LOCATE 11, 10: PRINT "or the LASERJET [H OR L]?"
LOCATE 12, 10: PRINT "Q to quit"
  ans$ = UCASE$(INPUT$(1))
  IF ans$ = "H" THEN HPlot$ = ans$ ELSE HPlot$ = ""
  IF ans$ = "L" THEN LJP$ = ans$ ELSE LJP$ = ""
  IF HPlot$ = "H" THEN OPEN "COM1: 9600" FOR OUTPUT AS #1

```

```

IF LJP$ = "L" THEN
  defile1$ = "C:\QB45\OUTPUT.PLT"

```

```

LOCATE 10, 1: PRINT SPACE$(79): LOCATE 11, 1: PRINT SPACE$(79)
LOCATE 12, 1: PRINT SPACE$(79): LOCATE 11, 1: PRINT SPACE$(79)
LOCATE 10, 5
PRINT "The Output file will be called "; defile1$
' PRINT "Enter the name of the Output file: [default = "; defile1$;"]"
' LOCATE 11, 5
' PRINT "It is best to use a .PLT extension until you are familiar"
' LOCATE 12, 5
' PRINT "with the LaserPlotter program"
' LOCATE 13, 5: INPUT FILE1$
'   set.time = TIMER + 2: WHILE TIMER < set.time: WEND
'   LOCATE 10, 5: PRINT SPACE$(79): LOCATE 11, 1: PRINT SPACE$(79)
'   IF FILE1$ = "" THEN FILE1$ = defile1$
'   FILE1$ = UCASE$(FILE1$)
'   OPEN FILE1$ FOR OUTPUT AS #1
'   END IF

IF ans$ = "Q" THEN CLOSE #1: EXIT SUB
IF ans$ = "" THEN
  LOCATE 8, 10: PRINT " You must answer ": GOTO again1
END IF
RETURN

```

```

GET.DAT:
REM =====
again2:
CLS
defile2$ = FILE$
LOCATE 10, 5
PRINT "Enter the name of the data file ": LOCATE 11, 5
PRINT "plus the path: [default = "; defile2$;
INPUT "]" ", FILE0$
IF FILE0$ = "" AND defile2$ <> "" THEN FILE0$ = defile2$
IF FILE0$ = "" THEN EXIT SUB
FILE0$ = UCASE$(FILE0$)
LOCATE 10, 1: PRINT SPACE$(79): LOCATE 11, 1: PRINT SPACE$(79)
ON ERROR GOTO Handler
OPEN FILE0$ FOR INPUT AS #2
INPUT #2, AERO, AER1
INPUT #2, steps, SHOTS
INPUT #2, SHIFTO, ATOD%
' AERO = SHIFTO + AERO
' AER1 = SHIFTO + AER1
NDPTS% = (AER1 - AERO) / steps + 1
IF ATOD% = 1 THEN
FOR idat = 1 TO NDPTS%
  INPUT #2, SIGX(idat), sig(idat)
  LOCATE 10, 10: PRINT USING "####.##    +##.###"; SIGX(idat);
  sig(idat)
NEXT idat

```



```

ELSEIF ATOD% = 2 THEN
FOR idat = 1 TO NDPTS%
    INPUT #2, SIGX(idat), sig(idat), DUMMY
    LOCATE 10, 10: PRINT USING "####.##    +##.###"; SIGX(idat);
    sig(idat)
NEXT idat
END IF
CLOSE #2
AERO = SIGX(1)
AER1 = SIGX(NDPTS%)
RETURN
REM      =====

X.Y.TICK:
REM      =====

Xtic = NDPTS% / 10: ytic = 1
xbox = Xtic / 10                ' Box around Data point
ybox = ytic / 10                ' Part of the Box
mx = NDPTS% / 200: my = 10 / 200

PRINT #1, "IN IP 0 0 10300 7560 SC"; .13 * -NDPTS%; 1.3 * NDPTS%; -2;
10.8; "; "
PRINT #1, "SP 1 PU PA"; 0; 0; "PD"; 0; 10; NDPTS%; 10; NDPTS%; 0; 0;
0; "; "
    FOR X = Xtic TO NDPTS% STEP Xtic
        PRINT #1, "PU PA"; X; my; "PD"; X; "0 PU; "
        IF LJP$ = "" THEN
            set.time = TIMER + .5: WHILE TIMER < set.time: WEND
        END IF
    NEXT X
    PRINT #1,
    FOR Y = ytic TO (10) STEP ytic
        PRINT #1, "PA"; 0; Y; "PD"; mx; Y; "PU; "
        IF LJP$ = "" THEN
            set.time = TIMER + .2: WHILE TIMER < set.time: WEND
        END IF
    NEXT Y
    Xlabel$ = "PU####.#,-.2;CP-3.5 -.5;LB####.##" + CHR$(3) + "; "
    FOR X = 0 TO 1.05 * NDPTS% STEP 2 * Xtic
        Xlabel = AERO + (X / NDPTS%) * (AER1 - AERO)
        PRINT #1, USING Xlabel$; X; Xlabel
        IF LJP$ = "" THEN
            set.time = TIMER + 1: WHILE TIMER < set.time: WEND
        END IF
    NEXT X
    IF LJP$ = "" THEN set.time = TIMER + 5: WHILE TIMER < set.time: WEND
    Ylabel$ = "PU0,##.##;CP-5.25 -.25;LB##.##" + CHR$(3) + "; "
    FOR Y = 0 TO 10 STEP 2
        PRINT #1, USING Ylabel$; Y; Y
        IF LJP$ = "" THEN

```

```

        set.time = TIMER + 1: WHILE TIMER < set.time: WEND
    END IF
NEXT Y
RETURN
REM =====

LABELS:
REM =====
REM          This routine lables the axes with x = wavenumbers and
REM          y = volts

Term$ = CHR$(3)
Xlable$ = "WAVENUMBERS"
Xlbl = LEN(Xlable$) + 1
PRINT #1, "PU"; NDPTS% / 2; -1; "CP"; -(Xlbl / 2); -.5; "LB"; Xlable$;
Term$
IF LJP$ = "" THEN set.time = TIMER + .5: WHILE TIMER < set.time: WEND
    Ylable$ = "VOLTS"
    ylbl = LEN(Ylable$)
    PRINT #1, "PU"; -.1 * NDPTS%; 5; "DI 0 1"; "CP"; -(ylbl / 2), 0; "LB";
    Ylable$; Term$
    RETURN

REM =====

PLOT.DAT:
REM =====

PRINT #1, "SP 2;"
IF LJP$ = "" THEN set.time = TIMER + 15: WHILE TIMER < set.time: WEND

    PRINT #1, "PA PU"; 1; sig(1); ";"
    FOR I = 1 TO NDPTS%
        PRINT #1, "PD"; I; sig(I); ";"
        IF LJP$ = "" THEN
            set.time = TIMER + .08: WHILE TIMER < set.time: WEND
        END IF
    NEXT I
    PRINT #1, "PU;SP;"
    RETURN
REM =====

TITLES:
REM =====
REM          The routine Titles inputs the title of the plot

LOCATE 10, 1: PRINT SPACE$(79): LOCATE 11, 1: PRINT SPACE$(79)
LOCATE 10, 1
INPUT "What is the Title"; title$
RETURN

```

```
REM =====
```

```
CHOICE.PARAMETERS:
```

```
REM =====
```

```
CLS
```

```
LOCATE 10, 1: PRINT SPACE$(79)
```

```
LOCATE 8, 3: PRINT CHR$(201) '218
```

```
LOCATE 8, 72: PRINT CHR$(187) '191
```

```
LOCATE 20, 3: PRINT CHR$(200) '192
```

```
LOCATE 20, 72: PRINT CHR$(188) '217
```

```
FOR I = 4 TO 71
```

```
LOCATE 8, I: PRINT CHR$(205) '196
```

```
LOCATE 20, I: PRINT CHR$(205) '196
```

```
NEXT I
```

```
FOR I = 9 TO 19
```

```
LOCATE I, 3: PRINT CHR$(186): LOCATE I, 72: PRINT CHR$(186) '179
```

```
NEXT I
```

```
LOCATE 4, 12: PRINT "YOU HAVE THE FOLLOWING CHOICES FOR PLOT  
INFORMATION"
```

```
LOCATE 10, 5
```

```
PRINT "YOU MAY: ": LOCATE 12, 5
```

```
PRINT "Print data acquisition parameters from a menu "
```

```
LOCATE 14, 5
```

```
PRINT "Input your own text "
```

```
LOCATE 16, 5
```

```
PRINT "Print the title only ":
```

```
LOCATE 18, 5
```

```
PRINT "or <RETURN> for none of the above "
```

```
LOCATE 22, 20: PRINT "Choose [1,2,3 or Return] ",
```

```
COLOR 0, 7
```

```
LOCATE 12, 60: PRINT CHR$(0) + "1" + CHR$(0)
```

```
LOCATE 14, 60: PRINT CHR$(0) + "2" + CHR$(0)
```

```
LOCATE 16, 60: PRINT CHR$(0) + "3" + CHR$(0)
```

```
LOCATE 18, 59: PRINT "Return"
```

```
COLOR 7, 0
```

```
ans3$ = INPUT$(1)
```

```
ans3 = VAL(ans3$)
```

```
IF ans3 = 1 THEN GOSUB PARAMETERS
```

```
IF ans3 = 2 THEN GOSUB SOME.TEXT
```

```
IF ans3 = 3 THEN GOSUB PRINT.TITLE
```

```
PRINT #1, "sp;pu-30 0;"
```

```
RETURN
```

```
PARAMETERS:
```

```
REM
```

```
REM This routine gives a menu of parameters and allows the changing  
REM of the values. Only the parameters in the menu may be printed.
```

```
CLS
mopt = 0
MENU2:
```

```
LOCATE 10, 1: PRINT SPACE$(79)
LOCATE 8, 1
LOCATE 6, 3: PRINT CHR$(201)           '218
LOCATE 6, 72: PRINT CHR$(187)          '191
LOCATE 18, 3: PRINT CHR$(200)          '192
LOCATE 18, 72: PRINT CHR$(188)         '217
FOR I = 4 TO 71
    LOCATE 6, I: PRINT CHR$(205)        '196
    LOCATE 18, I: PRINT CHR$(205)       '196
NEXT I
FOR I = 7 TO 17
LOCATE I, 3: PRINT CHR$(186): LOCATE I, 72: PRINT CHR$(186) '179
NEXT I
FOR I = 0 TO 8
    LOCATE 8 + 2 * (I \ 2), 6 + 40 * (I MOD 2): PRINT I + 1
NEXT I
```

```
LOCATE 8, 11: PRINT "PMT";
LOCATE 8, 51: PRINT "MON SLIT";
LOCATE 10, 11: PRINT "GAIN";
LOCATE 10, 51: PRINT "TIME CST";
LOCATE 12, 11: PRINT "DYE BM";
LOCATE 12, 51: PRINT "PRESSURE";
LOCATE 14, 11: PRINT "STEPS";
LOCATE 14, 51: PRINT "SHOTS";
LOCATE 16, 11: PRINT "OD";
```

```
NNUM:
```

```
PRINT
LOCATE 8, 25: PRINT SPACE$(7): LOCATE 8, 25: PRINT PMT;
LOCATE 8, 65: PRINT SPACE$(7): LOCATE 8, 65: PRINT MON.SLIT;
LOCATE 10, 25: PRINT SPACE$(7): LOCATE 10, 25: PRINT GAIN;
LOCATE 10, 65: PRINT SPACE$(7): LOCATE 10, 65: PRINT TIME.CST;
LOCATE 12, 25: PRINT SPACE$(7): LOCATE 12, 25: PRINT DYE.BM;
LOCATE 12, 65: PRINT SPACE$(7): LOCATE 12, 65: PRINT PRESS;
LOCATE 14, 25: PRINT SPACE$(7): LOCATE 14, 25: PRINT steps;
LOCATE 14, 65: PRINT SPACE$(7): LOCATE 14, 65: PRINT SHOTS;
LOCATE 16, 25: PRINT SPACE$(7): LOCATE 16, 25: PRINT OD;
PRINT
PRINT : PRINT
IF mopt <> 0 GOTO CHANGE.PARAM
LOCATE 3, 5
PRINT "Would you like to change the parameters? [Y/N] ",
ans1$ = UCASE$(INPUT$(1))
LOCATE 3, 1: PRINT SPACE$(79);
IF ans1$ = "Y" GOTO CHANGE.PARAM
```

```

LOCATE 4, 5
PRINT "WOULD YOU LIKE TO PRINT THE PARAMETERS? [Y/N] ",
ANS2$ = UCASE$(INPUT$(1))
LOCATE 4, 1: PRINT SPACE$(79)
IF ANS2$ = "Y" GOTO PRINT.PARAM
IF ANS2$ = "N" GOTO CHOICE.PARAMETERS
RETURN

```

CHANGE.PARAM:

```

LOCATE 20, 5
INPUT "Enter the number of the parameter to be changed: [0 to quit] ",
mopt
LOCATE 20, 1: PRINT SPACE$(79)
IF mopt = 0 GOTO NNUM

LOCATE 21, 1: PRINT SPACE$(79): LOCATE 21, 5
INPUT "Enter the new value ", new
LOCATE 21, 1: PRINT SPACE$(79)
IF mopt = 1 THEN PMT = new
IF mopt = 2 THEN MON.SLIT = new
IF mopt = 3 THEN GAIN = new
IF mopt = 4 THEN TIME.CST = new
IF mopt = 5 THEN DYE.BM = new
IF mopt = 6 THEN PRESS = new
IF mopt = 7 THEN steps = new
IF mopt = 8 THEN SHOTS = new
IF mopt = 9 THEN OD = new
GOTO NNUM

```

PRINT.PARAM:

```

GOSUB PRINT.TITLE
PRINT #1, "PU 2 1;LBPMT "; SPACE$(5); PMT; TAB(23); "MON SLITS ";
MON.SLIT; TAB(44); "GAIN "; GAIN; lf$
IF LJP$ = "" THEN set.time = TIMER + 7: WHILE TIMER < set.time: WEND
PRINT #1, "PU 1 1;LBTIME.CST "; TIME.CST; TAB(23); "DYE BM ";
DYE.BM; TAB(44); "PRESS "; PRESS; lf$
PRINT #1, "PU 0 1;LBSTEPS "; SPACE$(3); steps; TAB(23); "SHOTS ";
SHOTS; TAB(44); "OD "; OD; Term$
IF LJP$ = "" THEN set.time = TIMER + 4: WHILE TIMER < set.time: WEND
' PRINT #1, "PU -1 1;LB"; param4$; lf$
' PRINT #1, "PU -2 1;LB"; param5$; Term$
RETURN

```

SOME.TEXT:

```

REM
REM This Subroutine allows the input of 5 lines of your own choosing
REM after the file name and the title have been printed

```

CLS

```

LOCATE 7, 5
PRINT "5 lines of text may be written at this point. {E will exit}"
LOCATE 8, 5: PRINT "Type <Return> to begin."
LOCATE 9, 5
PRINT "Type <Return> at the end of each line.": LOCATE 11, 5
ans1$ = UCASE$(INPUT$(1))
IF ans1$ = "E" GOTO CHOICE.PARAMETERS
LINE INPUT "1.) "; Text1$: LOCATE 12, 5
LINE INPUT "2.) "; Text2$: LOCATE 13, 5:
LINE INPUT "3.) "; Text3$: LOCATE 14, 5
LINE INPUT "4.) "; Text4$: LOCATE 15, 5
LINE INPUT "5.) "; Text5$:
GOSUB PRINT.TITLE
IF LJP$ = "" THEN set.time = TIMER + 2: WHILE TIMER < set.time: WEND

    PRINT #1, "PU 2 1; LB"; Text1$; lf$
    PRINT #1, "PU 1 1; LB"; Text2$; lf$
    IF Text1$ = "" THEN GOTO skip1
IF LJP$ = "" THEN set.time = TIMER + 7: WHILE TIMER < set.time: WEND
skip1:
    PRINT #1, "PU 0 1; LB"; Text3$; lf$
    PRINT #1, "PU -1 1; LB"; Text4$; lf$
    IF Text3$ = "" THEN GOTO skip2
IF LJP$ = "" THEN set.time = TIMER + 5: WHILE TIMER < set.time: WEND
skip2:
    PRINT #1, "PU -2 1; LB"; Text5$; Term$
    RETURN

REM =====

PRINT.TITLE:
REM =====
    Term$ = CHR$(3)
    lf$ = CHR$(10) + CHR$(13) + CHR$(3)
    PRINT #1, "SP 1;"
IF LJP$ = "" THEN set.time = TIMER + 2: WHILE TIMER < set.time: WEND
PRINT #1, "SC -30 5 -1 1;"
PRINT #1, "DI 0 -1; SI .298 .405;PU 5 1; CP 0,-1;LB"; FILE0$; " ";
    title$; Term$
PRINT #1, "DI 0 -1; SI .19 .27;PU 5 1; CP 0,-3;LBDate: "; DATE$;
    SPACES$(5); "Time: "; TIME$; lf$
    RETURN

REM =====

PRINT.MESSAGE:
CLS
LOCATE 5, 1
IF LJP$ = "L" THEN
PRINT "The file you wish to plot using the LaserJet has"
PRINT "been sent to a print file called ["; FILE1$; "]"
PRINT "In order to print this file now you need to have DESQview"

```

```

PRINT "installed. If you have installed DESQview tap the ALT key to"
PRINT "invoke it. Then hit S and switch programs to LaserPlotter."
PRINT "[If you have not installed LaserPlotter type LP to get it"
PRINT "going.]"
PRINT "You will now be in the LaserPlotter program. Choose Files and"
PRINT "then "; FILE1$; "."
PRINT "The LaserPlotter program will run in the background but you"
PRINT "must return and hit any key to continue."
PRINT "S allows you to switch back and forth among the programs."
PRINT "It is not a good idea to switch when in the Screen (3) "
PRINT "graphics plotting mode. Good Luck!"
END IF
LOCATE 19, 1: PRINT "Hit any key to return": ans$ = INPUT$(1)
RETURN
END SUB

DEFSNG A-H
SUB SHIFT (A%, S0, d, S1, M) STATIC
,
SHARED OMEGO, order%, angperstep
,
d = (10 ^ 8 / (OMEGO - S0)) + A% * angperstep
S1 = OMEGO - 10 ^ 8 / d
M = 1 / (OMEGO + S1) * 10 ^ 8

END SUB

SUB SNDDATA (DATAOUT%) STATIC

SHARED PORT, AOUT, DBA, DBB

IBF = CHKIBF
OUT DBA, DATAOUT%
OUT DBB, &H1B
OUT DBB, &H1F
END SUB
' PUT DATA IN A'
' 1011=WRITE DATA
' TOGGLE WRITE

```

Appendix B: Seeded Nd:YAG Laser Scan Program

```

DECLARE SUB TIME (TM!)
DECLARE SUB DAOUT (VOL!, ADDRESS!)
DECLARE SUB ADIN (TOT!, ADDRESS!)
ADDRESS = 1808
DIM SIG(6000), V(6000)
' *****
' *
' *      PROGRAM:      SCAN Nd:YAG.BAS
' *
' *
' *      A QUICK BASIC PROGRAM TO SEND
' *      VOTAGE TO MING'S SCAN BOX WHICH
' *      WILL SCAN THE Nd:YAG LASER ABOUT
' *      2 cm-1
' *
' *
' *      WRITTEN BY: MING YANG
' *      Jan. 1989
' *****
,
110 :
CLS :
INPUT "ENTER INITIAL voltage (> 3.5 V) ", V0
IF V0 < 3.5 THEN 110
INPUT "ENTER FINAL voltage (< 7 V) ", V1
IF V1 > 7 THEN 110
INPUT "ENTER THE INCREMENT (mv) ", IN
INPUT "ENTER THE SHOTS TO AVERAGE ", SHOTS%
INPUT "ENTER HOW MANY SECONDS YOU WANT TO WAIT ", TM
,
'WRITE BYTE TO BOARD:ENABLE EXTERNAL START
X = INP(ADDRESS + 6)
OUT ADDRESS + 4, 128
OUT ADDRESS + 4, 132
OUT ADDRESS + 5, 0
,
NP% = INT(ABS(V1 - V0) * 1000 / IN)
PRINT :
INPUT "CHANG ANYTHING ", AN$
IF AN$ = "Y" OR AN$ = "y" THEN GOTO 110
PRINT "PAUSE----><CR> TO SCANNING"
WHILE INKEY$ = "RETURN"
WEND
,
SCREEN 3
VIEW (2, 2)-(680, 260), , 1
WINDOW (1, 0)-(NP%, 6)
VIEW PRINT 23 TO 25

```



```

,
LOCATE 24, 5: PRINT "X VOLTAGE  "
LOCATE 24, 40: PRINT "Y SIGNLE  "
VI = V0

FOR I = 1 TO NP%
    V(I) = VI
    CALL DAOUT(VI, ADDRESS)
    VI = VI + IN / 1000
    SUMO = 0
CALL TIME(TM)
    FOR J = 1 TO SHOTS%
        CALL ADIN(TOT, ADDRESS)
        DUM = TOT / 409.5
        SUMO = SUMO + DUM
    NEXT J
    SIG(I) = (SUMO / SHOTS%) + 1
LOCATE 24, 15: PRINT V(I)
LOCATE 24, 55: PRINT SIG(I)
, -----PLOT THE DATA -----
,
IF I = 1 THEN 200
LINE (I - 1, SIG(I - 1))-(I, SIG(I))
200 :
NEXT I
,
400 :
INPUT "DO YOU WANT TO SAVE DATA TO DISK  ", SA$
IF SA$ = "Y" OR SA$ = "y" THEN 500 ELSE 300
300 :
IF SA$ = "N" THEN 900 ELSE 400
500 :
INPUT "WHICH DRIVE (A: B: OR C:) ", WW$
IF WW$ = "a" OR WW$ = "A" THEN WW$ = "A:"
IF WW$ = "b" OR WW$ = "B" THEN WW$ = "B:"
IF WW$ = "c" OR WW$ = "C" THEN WW$ = "C:"
,
INPUT "FILE NAME  ", W$
OPEN WW$ + W$ FOR OUTPUT AS #1
    PRINT #1, IN / 1000
    FOR N = 1 TO NP%
        PRINT #1, V(N), SIG(N)
    NEXT N
CLOSE #1
900 :
WHILE HALT$ = ""
    HALT$ = INKEY$
WEND
GOTO 110

SUB ADIN (TOT, ADDRESS) STATIC
,

```

```
10 :  
  IF INP(ADDRESS + 4) < 128 THEN 10  
  LO = INP(ADDRESS + 5) AND 255  
  HI = INP(ADDRESS + 6) AND 15  
  TOT = 256 * HI + LO  
  IF HI > 7 THEN TOT = TOT - 4096
```

```
END SUB
```

```
SUB DAOUT (VOL, ADDRESS) STATIC  
,
```

```
  DECIMAL = 409.5 * VOL - 2048  
  DECIMAL = INT(DECIMAL)  
  HIGH = INT(DECIMAL / 256)  
  LOW = DECIMAL - (256 * HIGH)  
  IF HIGH < 0 THEN HIGH = 16 + HIGH  
,
```

```
  OUT ADDRESS + 1, HIGH  
  OUT ADDRESS, LOW
```

```
END SUB
```

```
SUB TIME (TM)
```

```
5 :  
ST = TIMER  
30 :  
FI = TIMER  
DT = FI - ST  
IF DT < 0 THEN 5  
IF DT < TM THEN 30
```

```
END SUB
```

Appendix C: LASER "BAD SHOT" DETECTOR MANUAL

MING YANG

DESCRIPTION OF FRONT PANEL:

POWER SWITCHThis power switch is for the *bad shot detector*. It has two positions *ON* and *OFF*.

POWER LIGHTWhen the power switch is in *on* position, the light should be *ON*.

TEST POINT SELECTIONThis switch has three positions:

Position 1. When switch is in this position, CH 1 and CH2 monitor the two photodiode outputs.

Position 2. When switch is in this position, CH1 and CH2 monitor the adjustable detection levels.

Position 3. When switch is in this position, CH1 and CH2 monitor the TTL output pulse. The channel 1 has negative pulses and the channel 2 has positive pulses.

LEVEL ADJUSTMENT ...When the *test point selection switch* is in *position 2*. The pots can be adjusted to choose the discriminator level at which a bad shot is to be determined.

GATE WIDTH AND DELAY These two pots can be used to adjust the output gate width and delay.

TWO INDICATION LIGHTS The green light should flash when laser light enters the detector box. The red one normally will be on but not flash, except when the laser has a bad shot.

OUTPUT Normally the output should be a positive TTL pulse when you let the laser light into the detector. When the laser goes multimode (bad shot) the TTL pulse should disappear.

"BAD SHOT" DETECTOR SETUP

1. First one should carefully choose the intensity of laser light into the detector so as not to saturate the I₂ absorption.
2. After properly choosing the incident beam intensity, one should check the photo diode output, level, and both channel TTL outputs. By adjusting the width and delay, the output TTL pulse width and delay can be chosen.
3. After these adjustment, one should block the seeder to see whether or not the output pulse disappears. If it does then everything should be OK, if not check the seeder frequency which can be adjusted on the other box named YAG laser scanner.

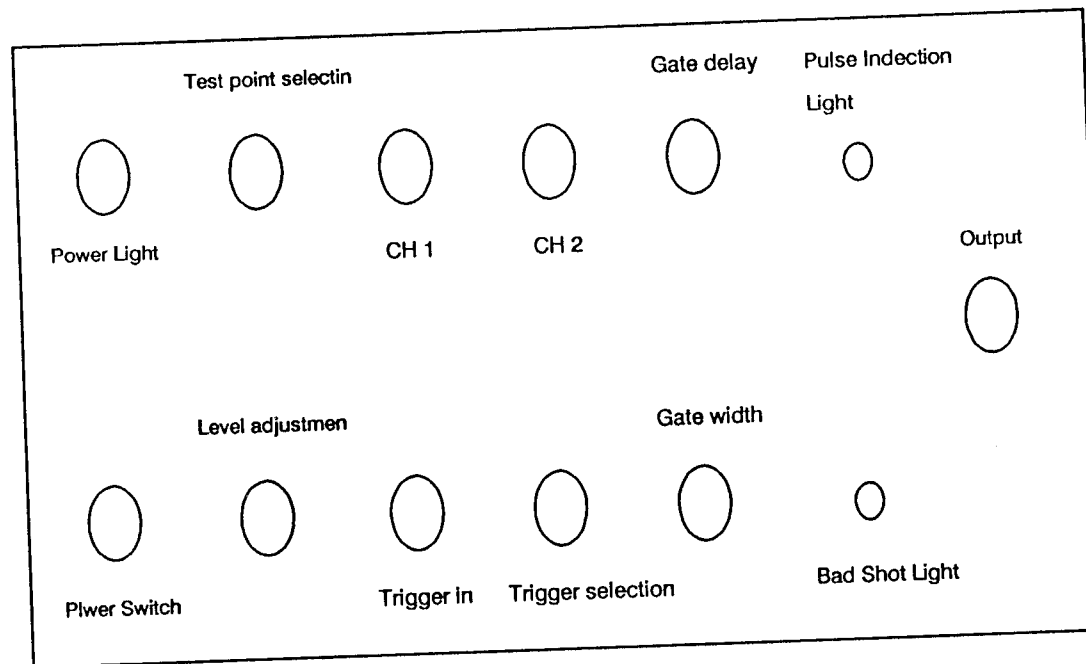


Figure C.1: Bad shot rejector front panel diagram.

Appendix D: Laser Noise Rejector

Figure 6.2 shows a schematic diagram of laser scanner and noise filter for seeded Nd:YAG laser. There are three different parts in this diagram: (a) noise filter, (b) laser scanner, and (c) power supply. The laser scan part has discussed in chapter 3, therefore in this appendix only the noise filter part will be discussed

As we discussed in chapter 3 the Q-switch buildup time reduction operation is used to stabilize the laser in a single frequency by minimizing the time different of Q-switch pulse and signal pulse from seeder. The resultant of the operation send to adjust the piezoelectric frequency tuning element to get minimum Q-switch build up time. The quality of the Q-switch pulse is very important to this operation. However, there are some noise in the Q-switch trigger line and the Q-switch buildup time reduction unit can not make good judgment which pulses come from the Q-switch trigger line is the real Q-switch pulse. The top part of diagram is the circuit which use the lamp pulse as the trigger and three operational amplifiers used to produce a positive 5 volts TTL pulses which send to trigger a 74211 chip then the output pulse was sent to U1A109 chip (pin 5) which is located inside of seeder By adjusting the pulse delay time and width to match the Q-switch pulses, the U1A109 now control by the input pulse which only let the Q-switch pulse goes through and all noise pulses are blocked.

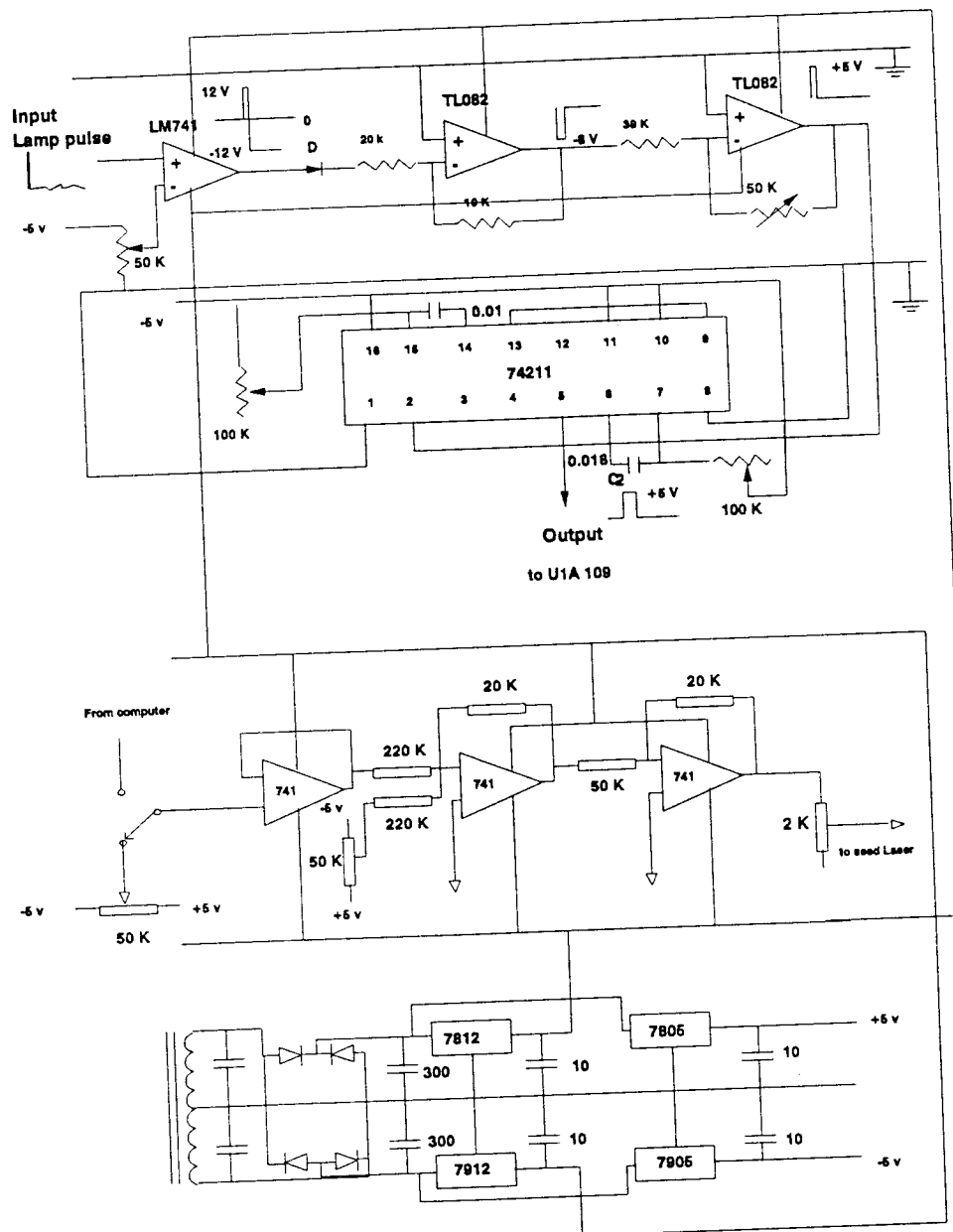


Figure D.1: Temperature scan and noise rejector circuit.

Appendix E: Data used in this thesis

Data used in chapter 5 (Fig. 5.7, 5.11 and 5.12) are listed below.

Filename	X/D	$\nu[\text{cm}^{-1}][\text{L}]$	$\nu[\text{cm}^{-1}][\text{S}]$	T[K]
N2Je1. J14	0.25	2326.407		58
N2Je2. J14	0.75	2326.404		57.8
N2Je3. J14	1.25	2326.392		55.5
N2Jet5. J17	2.50	2326.377		49.3
N2Jet6. J17	5.00	2326.363		44.8
N2Jet7. J17	7.50	2326.362		42
N2Jet8. J17	10.0	2326.350		40
N2Jet9. J17	12.5	2326.341		38.5
N2Jet15. J17	13.75	2326.336	2326.573	40.2
N2Jet16. J17	14.38	2326.334	2326.564	41.0
N2Jet14. J17	15.0		2326.551	42.1
N2Jet13. J17	17.5		2326.522	44.7
N2Jet12. J17	20.0		2326.546	42.5
N2Jet1. J25	27.5		2326.555	41.7
N2Jet2. J25	30.0		2326.564	40.6
N2Jet3. J25	32.5		2326.579	39.6
N2Jet4. J25	35.0		2326.583	39.3
N2Jet5. J25	37.5		2326.592	38.4
N2Jet6. J25	40.0		2326.594	38.3
N2Jet7. J25	42.5		2326.577	39.8
N2Jet8. J25	45.0		2326.598	38.0
N2Jet9. J25	47.5		2326.607	37.1